CONVECTIVE AND RAINFALL PROPERTIES OF TROPICAL CYCLONE INNER CORES AND RAINBANDS IN RELATION TO TROPICAL CYCLONE INTENSITY CHANGES USING ELEVEN YEARS OF TROPICAL RAINFALL MEASURING MISSION DATA

by

Ellen Michelle Ramirez

A thesis submitted to the faculty of
The University of Utah
in partial fulfillment of the requirements for the degree of

Master of Science

Department of Atmospheric Sciences

The University of Utah

May 2011

The University of Utah Graduate School

STATEMENT OF THESIS APPROVAL

The thesis of **Ellen Michelle Ramirez**

has been approved by the following supervisory committee members:

Haiyan Jiang	, Chair	**3/17/11** Date Approved
Edward J. Zipser	, Member	**3/18/11** Date Approved
Steven Krueger	, Member	**3/24/11** Date Approved

and by **W. James Steenburgh** , Chair of the Department of **Atmospheric Sciences**

and by Charles A. Wight, Dean of The Graduate School.

ABSTRACT

Covering December 1997 through December 2008, over 13,000 tropical cyclone (TC) overpasses of 945 TCs by the Tropical Rainfall Measuring Mission (TRMM) satellite are used to document the observed passive microwave ice scattering magnitudes, radar reflectivity, IR cloud top height, total lightning, and derived rainfall parameters including rain rate, raining area, and volumetric rain. A semimanual method is used to divide TC raining area into inner core (IC), inner rainband (IB), and outer rainband (OB) regions. Precipitation features (PFs) within these regions are compared for their convective vigor and rainfall characteristics based on passive microwave, IR, radar, and lightning properties. These properties in the IC region are further examined in terms of different TC intensity and intensity change categories. TC intensity categories include tropical depressions (TDs), tropical storms (TSs), category 1-2 hurricanes (CAT12s), and category 3-5 hurricanes (CAT35s). The 24-h TC intensity change categories include weakening (W), neutral (N), slowly intensifying (SI), and rapidly intensifying (RI).

The stronger tails of the convective intensity distributions are found to be similar for features in both the IC and OB regions, while the features in the IB region yield the weakest convective signatures. However, at the middle to weaker end of the convective spectrum, ice scattering signatures and reflectivity profiles are the strongest for features in the IC region, followed by those in the IB, then those in the OB. The same order is found for the whole distribution spectrum of feature conditional mean rain rates in these

regions. The convective intensity of features in the IC region are found to increase as storm intensity increases, except at the strongest end of the spectrum, where ice scattering signatures and reflectivity profiles are stronger in features associated with TS and TD strength storms rather than those associated with hurricane strength storms. The IC conditional mean rain rate and volumetric rain increase as storm intensity increases. It is found that necessary conditions for RI are that the minimum 85 GHz PCT in the IC region must be less than 256 K and the minimum 37 GHz PCT must be less than 275 K. Over 98% of RI minimum 11μm brightness temperatures in the IC region are less than 212 K. RI storms always have larger raining area and volumetric rain in the IC region than storms in other intensity change categories.

TABLE OF CONTENTS

LIST OF TABLES

ACKNOWLEDGEMENTS

For guidance and learning experiences during this research opportunity, I sincerely thank Dr. Haiyan Jiang. This project could not have been completed without her. I also thank Dr. Daniel J. Cecil of UAH for helpful feedback and conversations, and Dr. Steven Krueger for serving on my thesis committee. For advice and assistance, I thank the faculty and students of the tropical meteorology group including Dr. Edward J. Zipser, Dr. Chuntao Liu, Weixin Xu, Jon Zawislak, Christy Wall, Adam Varble, Michael Peterson, and Sarah Bang. For love, encouragement, and unwavering support during graduate school, I thank my mother and father, Richard and Jane, and my brother and sister, Matt and Maggie. You have all made this academic endeavor possible, and for that I am greatly indebted.

CHAPTER 1

INTRODUCTION

Observations of tropical cyclones (TCs) are limited because they spend most of their lifetime over open oceans. The Tropical Rainfall Measuring Mission (TRMM) satellite marks the first time that TCs in all ocean basins can be viewed by a high resolution downward-looking precipitation radar. After 12 y of successful operation, TRMM measurements, including those from the TRMM Microwave Imager (TMI), Precipitation (PR), Visible and Infrared Scanner (VIRS), and Lightning Imaging Sensor (LIS), have provided invaluable sources of TC data for the study of TC structure, intensity, and intensity change.

It has been long known that convective systems over tropical oceans, including TCs, generally produce weaker vertical motions and have weaker convective intensity than their continental counterparts (LeMone and Zipser 1980, Jorgensen and LeMone 1989, Lucas et al. 1994). This has been indicated by observations of sharp decreases in radar reflectivity above the melting layer (Szoke et al. 1986, Black et al. 1996, Cecil et al. 2002), modest passive microwave ice scattering signatures (Cecil and Zipser 1999, 2002), and low lightning flash rates (Black et al. 1986, Samsury and Orville 1994, Molinari et al. 1999, Cecil et al. 2002). However, the characteristics of convective intensity and precipitation are different in distinct regions of TCs. Szoke et al. (1986) found that the mean radar reflectivity profiles are similar above the freezing level for convective cells in

hurricane rainbands and in general tropical oceanic rainfall systems, but the mean eyewall reflectivity profile above the freezing level is stronger. Jorgensen et al. (1985) and Black et al. (1996) found that inner rainbands exhibit weaker updraft magnitudes than do eyewalls. Cecil et al. (2002) and Cecil and Zipser (2002) showed that the convective cores within the eyewall region have the highest reflectivity compared with that in inner and outer rainbands. In terms of ice scattering signatures derived from microwave observations, Cecil et al. (2002) demonstrated that the eyewall region has a higher percentage of samples with depressed 37 and 85 GHz polarization corrected brightness temperatures (PCTs, Spencer et al. 1989) than both inner rainband and outer rainband regions. The lack of lightning in the inner rainband region compared to the rest of the hurricane has been found by Molinari et al. (1999) and confirmed by Cecil et al. (2002). The controversial part is that Molinari et al. (1999) found that eyewall flash rate densities show a relatively weak maximum and that outer rainband flash densities show a relatively strong maximum, while Cecil et al. (2002) found that lightning flash densities in the eyewall region and outer rainband region, normalized by the total precipitation area, are similar and four times greater than in the inner rainband region. Cecil et al. (2002) attributed this difference to deficiencies in the sample size and representative of either study.

Satellite-based microwave observations can not only provide advanced understanding of convective intensity in distinct regions of TCs, but they also help improve our knowledge on TC intensity and intensity change. The low central pressure corresponding to the subsidence warming in the eye is sometimes referred to as the TC's intensity. In this study, the maximum sustained wind speed is used to define the intensity.

Although visible and infrared (IR) imagery from geostationary satellites provide the most continuous data for TCs, data at microwave frequencies from polar-orbiting satellites are more directly related to convection and precipitation than are those from visible and IR channels. Previous studies (Steranka et al. 1986, Rao and MacArthur 1994, Rodgers et al. 1994, Rodgers and Pierce 1995, Cecil and Zipser 1999, Kelley et al. 2004, 2005, Kerns and Zipser 2009) have related information from microwave data to TC intensity, future intensity, and intensity change.

Rain rates derived from all four channels (19.35 GHz, 22.2 GHz, 37.0 GHz, and 85.5 GHz) of Special Sensor Microwave Imager (SSM/I) observations were used to examine western North Pacific typhoons (primarily from 1987) and the associated precipitation fields by Rao and MacArthur (1994). They found that rain rates were highly correlated with 24-h future typhoon intensity with a correlation coefficient as high as 0.68 for rain rates averaged in the 2.0° radius box.

On the other hand, low correlations were found by Rodgers and Pierce (1995), who examined precipitation characteristics derived from SSM/I for a dramatically larger sample size. A total of 123 SSM/I observations of tropical depressions, 61 observations of tropical storms, and 73 observations of typhoons occurring from 1987 through 1992 comprised the sample. They compared the 12-h increase in inner core (1.0° radius) rain rate with the 12-h and 24-h change in maximum wind speed of the TC. Results for both the 12-h and 24-h change in maximum wind were similar, with tropical depressions yielding a correlation of 0.25, tropical storms yielding a correlation of 0.51, and typhoons yielding a negligible correlation of 0.04. Rodgers et al. (1994) performed a similar study using Western North Atlantic TCs, but with a much smaller sample size. Tropical

depressions and tropical storms produced a correlation of 0.06 and 0.27, respectively. The hurricane sample produced the highest correlation, 0.78.

Cecil and Zipser (1999) examined TCs in the Atlantic, Eastern North Pacific, and Western North Pacific that were observed by SSM/I during 1995 and 1996. A total of 277 SSM/I observations of TCs at hurricane/typhoon strength were used to relate 85 GHz ice scattering signatures to hurricane/typhoon intensity. High correlations (~-0.7) are found between inner core areal mean 85 GHz PCT (and the percentage area having PCT at or below 250 K) and future hurricane/typhoon intensity. As pointed out by Mohr and Zipser (1996a,b) and Mohr et al. (1996), the 250 K PCT is considered an indicator of moderate rain. Therefore, Cecil and Zipser's (1999) results indicate that the strongest correlations involve the spatial coverage of at least moderate inner core rainfall. Similarly, Kerns and Zipser (2009) found that enhanced TC genesis probability is associated with greater cold cloud area and raining area, especially in the Eastern North Pacific.

The above-mentioned parameters that produce the highest correlations with intensity respond primarily to the mesoscale coverage of the precipitation in the inner cores of TCs, as opposed to the convective scale. However, early studies suggested that hot towers (Simpson et al. 1998), convective bursts (Steranka et al. 1986), and enhanced lightning activity (Lyons and Keen 1994) near the eye can be related to TC intensity change. Molinari et al. (1999) found that the moderate-to-strong hurricanes in their study had inner core flash density maxima below 30 flashes $(100\ km)^{-2}\ d^{-1}$, but the marginally intense hurricanes had maxima in excess of 100 flashes $(100\ km)^{-2}\ d^{-1}$, suggesting that core convection in weaker TCs (that may have not yet reached their Maximum Potential Intensity; MPI, Emanuel 1986) is more electrified. Recent modeling studies (Hendricks et

al. 2004, Montgomery et al. 2006) have proposed that intense "vortical hot towers" may be a missing link in the chain of events that transforms a mid-level vortex into a near-surface vortex, initiating TC genesis and rapid intensification. This model-based result needs to be evaluated by observational studies not only on a case study basis, but more importantly in a statistical manner. Recent observational studies also found that the chance of TC intensification increases when one or more hot towers exist in the eyewall, using a limited subset of TRMM precipitation radar (Kelley et al. 2004) and WSR-88D radar data (Kelley et al. 2005). A hot tower (first proposed by Riehl and Malkus 1958) is a tropical cumulonimbus cloud extending from the lower troposphere up to the tropopause and sometimes into the stratosphere. They are termed "hot" because they rise due to the large amount of latent heat release. Still, uncertainties of the importance of hot towers in relation to TC intensification remain and additional quantification with a larger database is highly desirable.

In this study, we use the 11-y (December 1997-December 2008) TRMM Tropical Cyclone Precipitation Feature (TCPF) database (Jiang et al. 2010) to study convective and precipitation properties in distinct TC regions, and different TC intensity and intensity change stages. For the lightning analysis exclusively, data from 2009 are included. TC inner core (IC), inner rainband (IB), and outer rainband (OB) regions are divided subjectively by using a semimanual method adapted from Cecil et al. (2002). The purpose of this study is:

1) To quantitatively compare the convective and rainfall characteristics of IC, IB, and OB precipitation features (PFs) using the 11-y TRMM TCPF database. Properties to be investigated include the 85 and 37 GHz PCTs, IR 11μm

brightness temperature, rain rate, volumetric rain (rain rate multiplied by the raining area), reflectivity profiles, and lightning.

2) Using the same database and properties in 1), to quantitatively examine the convective and rainfall characteristics of IC PFs for different TC intensity categories, i.e., tropical depression, tropical storm, category 1-2 hurricane, and category 3-5 hurricane.
3) Using the same database and properties in 1), to quantitatively investigate the relationship between the convective and rainfall characteristics of IC PFs and TC intensity change stages, i.e., weakening, neutral, slowly intensifying, and rapidly intensifying.

CHAPTER 2

DATA AND METHODS

2.1 Tropical Cyclone Inner Core and Rain Band Separation

The categorizations used in this study follow the three distinct regions identified by Cecil et al. (2002) subjectively using TRMM TMI and PR observations. These categories are 1) the eyewall region, 2) the inner rainband region, and 3) the outer rainband region. The eyewall is a circular band of clouds and precipitation sloping radially outward with height that encircles the eye. In the cases of low-intensity TCs without a clear eye (and therefore no eyewall), near-center convection is included in this category. Therefore, we define this category as the *inner core (IC)* instead of the eyewall region. The IC region includes complete eyewalls, incomplete or partial eyewalls, concentric eyewalls, and near-center convection for storms without an eye. The *inner rainband (IB)* region includes banded or blob-like precipitation immediately outside of the IC boundary. The *outer rainband (OB)* region includes outward spiraling rainbands, no matter their spatial extent.

More than 13,000 TRMM TC overpasses from December 1997 to December 2008 are subdivided into IC, IB, and OB regions (collectively referred to as TC regions) by subjectively analyzing gradients and transitions zones in TMI and PR orbital data. Storms must have reached minimum tropical storm intensity at least once in their lifecycle. Radial limits for each TC region are assigned with the aid of concentric circles plotted at

30 km intervals outward from the TC center. Storm center locations are linearly interpolated from best track data, an archived 6-h post analysis product from the National Hurricane Center (NHC) and Joint Typhoon Warning Center (JTWC). This procedure is partially an extension of Cecil et al. (2002) who hand-traced TC regions for 261 TRMM observed TC overpasses (PR swath only) from December 1997 through December 1998. The present work instead uses circles to define TC regional boundaries in order to process over 40 times more data including 11 y of TRMM TC observations in both TMI and PR swaths. Extension of IC convection into the designated IB region is inevitable for some asymmetric storms. In such instances, the IC boundary is allowed to reach into the moat region, a circular rain free or lightly raining area outside of the IC. However, if the lightly raining area appeared as a *band* of precipitation, then it likely belonged in and was assigned to the IB. In this latter circumstance, the IB is subject to IC contamination.

In general, the high resolution and 3-D PR reflectivity is a better TC region discriminator than the 2-D observations from TMI. But, since IC convection slopes outward with height, an estimated radius from PR near surface parameters may be smaller than an estimated radius near the tropopause from TMI parameters. For this reason, both PR (when available) and TMI data were consulted simultaneously, but preference was given more towards TMI pixels in the interest of capturing all IC convection. The IC was completely captured by the TMI swath for all the TC observations used in this study, but entirely missed by the PR swath for 33% of the total sample. In the absence of PR data, the most useful discriminator is the 85 GHz PCT (showing ice scattering signature) because of its sensitivity to precipitation-sized ice particles that are characteristically present in strong IC updrafts. Example images used in

the TC region separation process are shown in Figs. 2.1-2.4. Figure 2.1 is a typical 6-panel view of a single overpass, Typhoon Namtheun in this case.

Two panels (Fig. 2.1b,d) are extracted and enlarged in Fig. 2.2 for closer inspection. The left panel shows the PR maximum reflectivity projection, while the right panel represents TMI 85 GHz PCT. This overpass is ideal because the TRMM instruments pass directly over the TC center and the precipitation is roughly concentric. The PR swath extends to 120 km radius and the TMI to 450 km radius from the TC center, which correspond to the maximum radial limits for all perfectly centered observations. The IC region exhibits 40+ dBZ maximum radar echoes with sub 200 K 85 GHz PCT out to 45 km radius. This convection is encircled by an echo-free annulus. The IB consists of secondary lines of precipitation, reflectivities, and depressed PCTs inwards of 110 km. The OB region lies between 110 km and 570 km, where deep convective cells are embedded in outward spiraling rainbands.

Figure 2.3 highlights the process of defining an IC without PR data. The abrupt increase in 85 GHz and 37 GHz PCTs at 65 km radius marks the outer boundary of the IC, coincidentally where PR coverage begins. An area of relatively low radar reflectivity near 150 km separates the IB from the innermost outer spiral rainband. At times it is difficult to distinguish OB convection from non-TC convection. If precipitating extremities can be visually traced inwards of 500 km, then their outermost contiguous reach is included within the OB boundary. Here, the OB boundary is marked at 450 km radius. Note the proximity of this TC to the Philipine Islands. Although the storm IC is over ocean, approximately one third of the 2A12 raining area is over land. An

explanantion of how storms near coastlines are handled is given in the latter part of this chapter.

Asymmetric TCs (e.g., Fig. 2.4) increase difficulty in parsing TC regions. Gradients in the TRMM data are not as steep and so the separation process requires looking for subtle changes or inconsistencies in TRMM parameter magnitudes. For example, relatively weak near surface reflectivity and low rain rate near the 60 km radius signify the IC edge, as higher values are observed inward of this threshold. The IB extends to the edge of the innermost spiral rainband at 115 km radius, visible in Fig. 2.4b. Lastly, the OB is defined out to 480 km radius, inside of where other likely unassociated convection exists.

The mean and standard deviations of the radial extent of IC, IB, and OB regions are given in Table 2.1. The mean extents of the IC, IB, and OB are 82, 162, and 502 km, respectively. Cecil et al. (2002) reported that the mean radii of their eyewall, IB, and OB regions were 50, 135, and 350 km, respectively, which are all smaller than what we determined here. The discrepancy is due to the fact that their sample included only mature TCs with well defined eyewalls whereas this study includes all near center convection, even for disorganized systems. Additionally, Cecil et al. (2002) used both PR and TMI data inside the PR swath, but this study includes all TMI data in a wider swath where radar observations may or may not be available.

2.2 Tropical Cyclone Precipitation Feature Definitions

The University of Utah (UU) tropical convection group developed a TRMM precipitation feature (PF) database (Nesbitt et al. 2000, Liu et al. 2008) for event based precipitation analysis. Adjacent pixels that satisfy specified criteria are grouped as a

single entity, i.e., a PF. A *tropical cyclone precipitation feature* (TCPF) database (Jiang et al. 2010) is derived from the UU TRMM PF database. The criterion to define a TCPF is the PF center has to be within 500 km of a linearly interpolated TC best track center. The storm information along with measurements from the TRMM instruments is saved as level-2 FIU/UU TCPF data (Fig. 2.5), a subset of the UU PF level-2 data. Storm parameters used in this study include a land / ocean flag, the current wind speed, and the future 24-h wind speed.

Two types of TCPFs are used in this study (Table 2.2). The TTPFs are defined in TMI swath with 2A12 (Kummerow et al. 1996) rain rate greater than zero. The RPFs are defined in PR swath with 2A25 (Iguchi et al. 2000) rain rate greater than zero. All TTPFs and RPFs hereafter are understood as TCPFs. The size criterion of TCPFs used in this study is at minimum four pixels for PR swath features (RPFs) and one pixel for TMI swath features (TTPFs).

2.3 Population Overview

Using the recorded IC, IB, and OB radii for each cyclone overpass, TCPFs are assigned to the TC region in which they occur. If a feature crosses a regional boundary then it is split into two features. This procedure generates over 95,000 TTPFs and over 250,000 RPFs. Features are considered *good* if both the parent TC center and the feature center are over ocean. To ensure a quality sample, if the instrument (either PR or TMI) captured a TC region (IC, IB, or OB) less than a percentage threshold, the sample is removed. The TMI swath must have observed the IC (IB, OB) region at 100% (100%, 60%) for IC (IB,OB) TTPFs to be used. The PR swath must have observed the IC (IB, OB) region at 80% (70%, 30%) for IC (IB, OB) RPFs to be used. The approximate

capture percentages are estimated subjectively by visual inspection. To exclude the overwhelmingly large number of small PFs, TTPFs and RPFs that meet or exceed 1000 km^2 in area are considered in most of the study, unless indicated otherwise. To illustrate the need for a size restriction, 2-D histograms of TTPF frequency as a function of minimum 85 GHz and 37 GHz PCT are plotted in Figs 2.6-2.7. Notice the barrage of small, (i.e. less than 1000 km^2) warm TTPFs, particularly in the OB region.

2.3.1 Microwave Imager TTPFs: Population and Geographical Distribution

Approximately 85 % of TMI snapshots captured the TC IC entirely, and only these overpasses are used for analysis (Table 2.3). The 7545 parent TC centers and 23411 TTPFs are plotted in Figs. 2.8-2.9. In Fig. 2.8 the basin labels are marked for the North Indian Ocean (NIO), South Indian Ocean (SIO), North West Pacific (NWP), South Pacific (SPA), East Pacific (EPA), and Atlantic (ATL) basins.

2.3.2 Precipitation Radar RPFs: Population and Geographical Distribution

Similar results as in Figs. 2.6-2.7 were obtained for RPF 2-D histograms (not shown). The total RPF sample decreases by 55% when PR capture restrictions are imposed. The RPF dataset is more limited than the TTPF dataset because of the narrower instrument swath, only 247 km for PR versus 878 km for TMI. Subsequently, the RPF ICs and IBs cannot be constrained by 100% capture, as was done for TTPF ICs and IBs. Sample sizes are presented in Table 2.4. The 7585 parent TC centers and 10348 RPFs are plotted in Figs. 2.10-2.11.

2.4 Selection of TRMM parameters

In this study, analysis of TTPF and RPF characteristics is done through examining TRMM observed convective and rainfall proxies. Parameters selected in this study for both TTPFs and RPFs include total flash counts and lightning flash rate. Parameters for TTPFs only include PF size, minimum 85/37 GHz PCT, minimum 11 micron [μm] Tb, percentage of pixels with 85 GHz PCT less than 250, 225, 200, and 150 K, percentages of pixels with 11 μm Tb less than 235 and 210 K, 2A12 raining area, 2A12 rain rate, and 2A12 volumetric rain. Parameters solely for RPFs in this study include 2A25 rain rate, 2A25 volumetric rain, 2A25 raining area, vertical profile of maximum radar reflectivity, maximum near surface radar reflectivity, maximum height of radar echo at specific reflectivity value, and area of radar echo higher than certain values.

The TMI brightness temperatures at 85 and 37 GHz respond to the scattering of upwelled radiation by precipitation-sized frozen hydrometeors, which reduce the observed brightness temperature. The PCTs at 85 and 37 GHz are defined to remove the ambiguity between low brightness temperatures due to ice scattering and due to low sea surface emissivity (Spencer et al. 1989, Cecil et al. 2002). Magnitudes of temperature depressions depend on ice particle number densities and size distributions (with respect to wavelength). Compared to 85 GHz PCT, 37 GHz PCT is more sensitive to large ice particles than small ice particles. Therefore, low values of minimum 85 GHz PCT tend to indicate a large ice water path, while low values of minimum 37 GHz PCT tend to indicate that the feature contains larger ice particles. Both the minimum 85/37 GHz PCT and percentage of pixels with 85 GHz PCT less than certain values are considered as convective proxies in this study. The traditional way to define deep convection from IR

measurements is finding pixels with brightness temperatures colder than a given threshold. Therefore, minimum 11 μm Tb observed by TRMM VIRS and percentage of pixels with 11 μm Tb less than a certain threshold are considered convective proxies too. Radar reflectivity depends on hydrometeor phase and the sixth power of hydrometeor diameter for Rayleigh scattering. Reflectivity, therefore, responds preferentially to the largest particles in a sample volume. High reflectivities below the freezing level indicate large liquid water content, while high values above the freezing level indicate supercooled liquid raindrops or large ice particles, which can only reach those altitudes by substantial updrafts. Without strong updrafts, reflectivity decreases rapidly with height above the freezing level. Lightning occurs as a result of a charge separation generated by collisions of large and small ice particles in the presence of supercooled liquid water (Takahashi 1978). The likelihood of a discharge, therefore, is contingent upon both the ability of an updraft core to loft liquid droplets into the mixed phase region and the supply of liquid hydrometeors. Supercooled liquid water in a hurricane is rare because it is quickly scavenged by of the abundance of ice being horizontally redistributed about the cyclone vortex (Black and Hallett 1986). The preferred location for electrification may then be the outer rainbands of a hurricane where convective dynamics are “normal” compared to the IC. Electrical activity can also be evaluated by flash rates, either from multiple convective bursts or isolated events. The proxies to represent rainfall characteristics are derived from TMI 2A12 and PR 2A25 rain. Both rain rate and volumetric rain are examined.

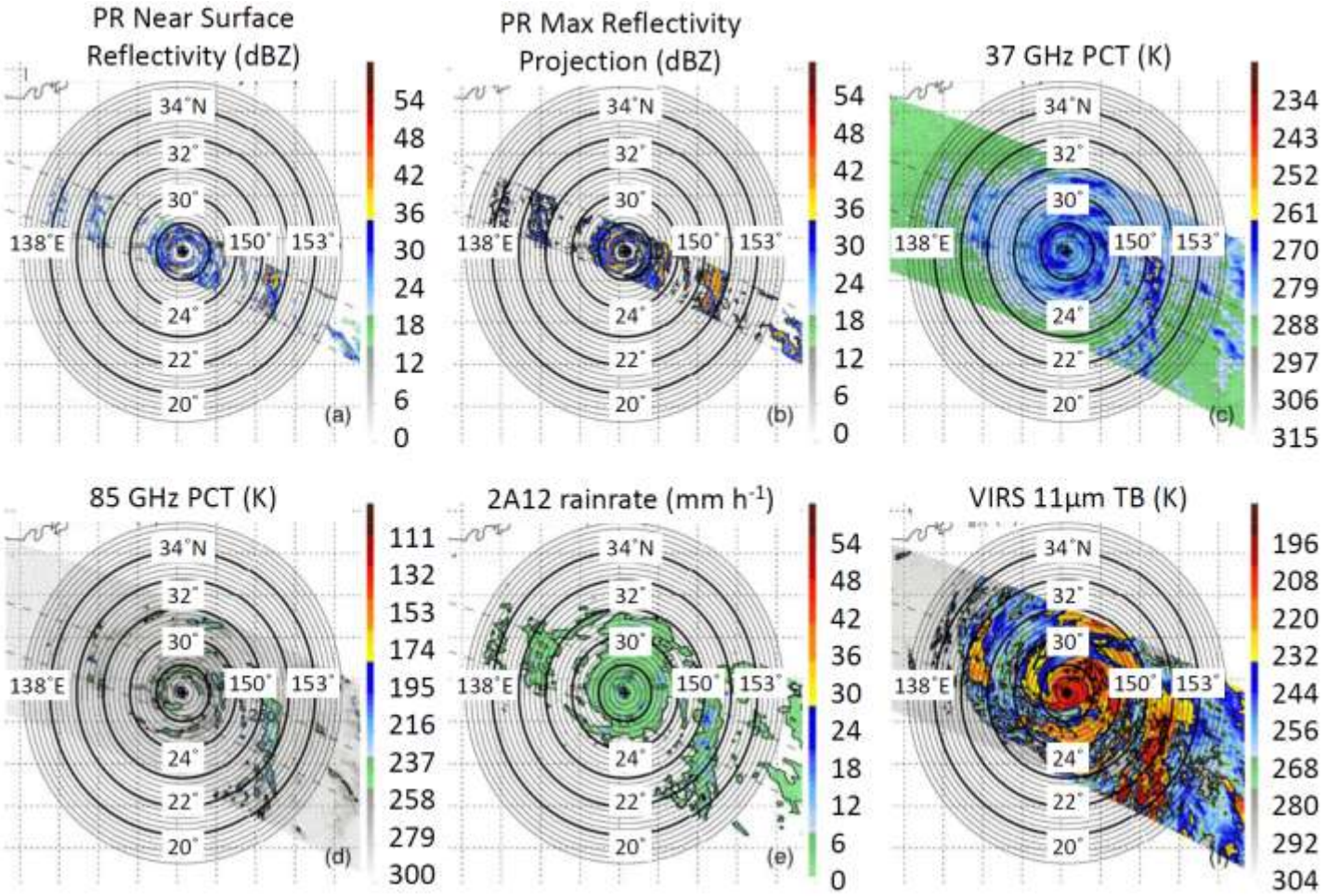

Figure 2.1. TRMM overpass of Typhoon Namtheun (current maximum wind speed 115 kts) of the North West Pacific basin at 2100 UTC 26 July 2004 showing (a) PR near surface reflectivity [dBZ] (b) PR maximum reflectivity projection [dBZ] (c) 37 GHz PCT [K] (d) 85 GHz PCT [K] (e) 2A12 rain rate [mm h^{-1}], and (f) VIRS 11µm brightness temperature [K]. The TC center is indicated by a black cross in each panel. Thin grey circles represent 30 km increments radially outward from the TC center and thick black circles represent 150 km increments radially outward from the TC center. The dashed lines in (a)-(f) are the edges of the TRMM PR swath.

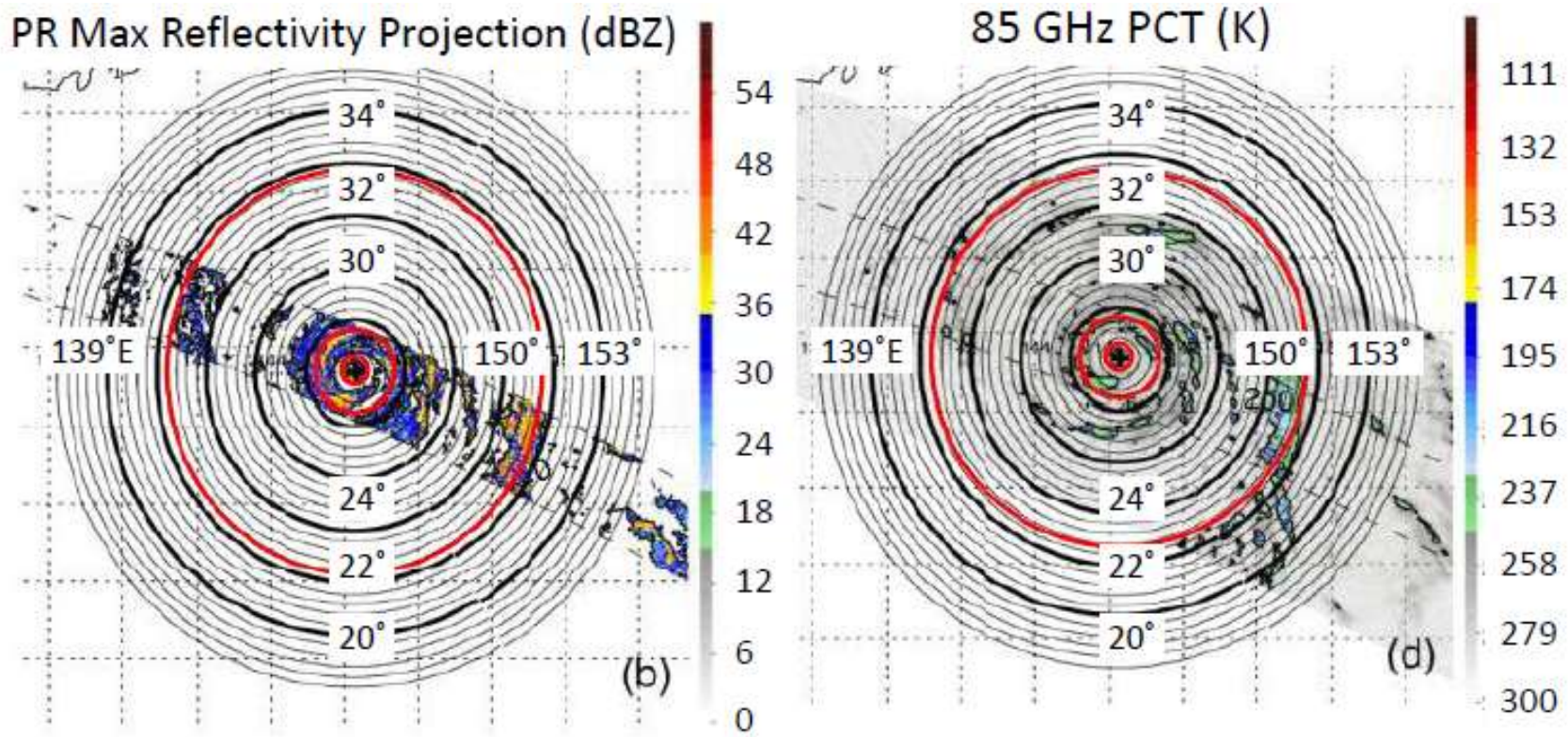

Figure 2.2. A zoomed-in excerpt of panels b and d from Fig. 2.1. Red circles indicate the outer edge of the IC, IB, and OB boundaries.

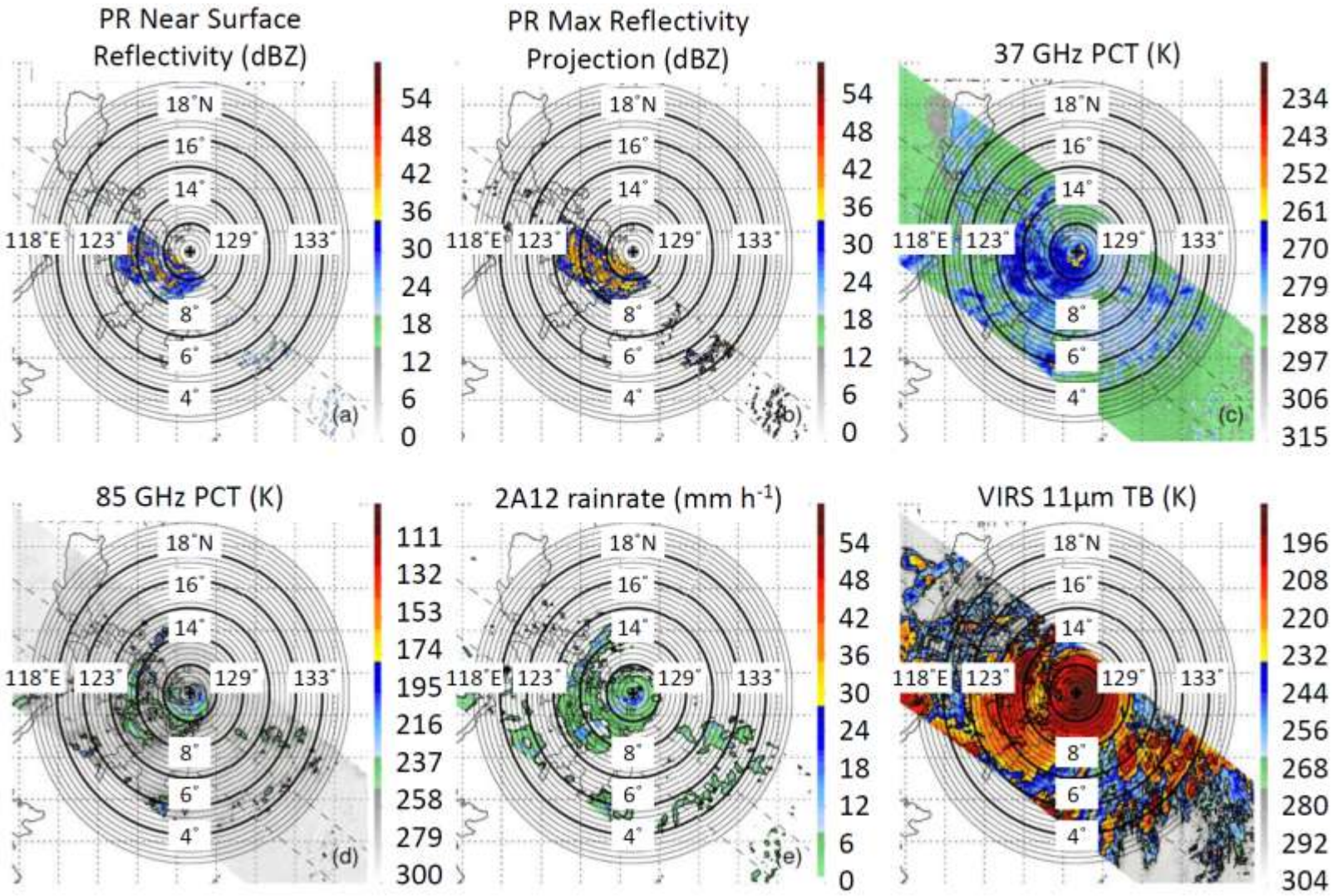

Figure 2.3. Same as Fig. 2.1 except for Typhoon Fengshen (current maximum wind speed 69 kts) of the North West Pacific basin at 2300 UTC 19 June 2008.

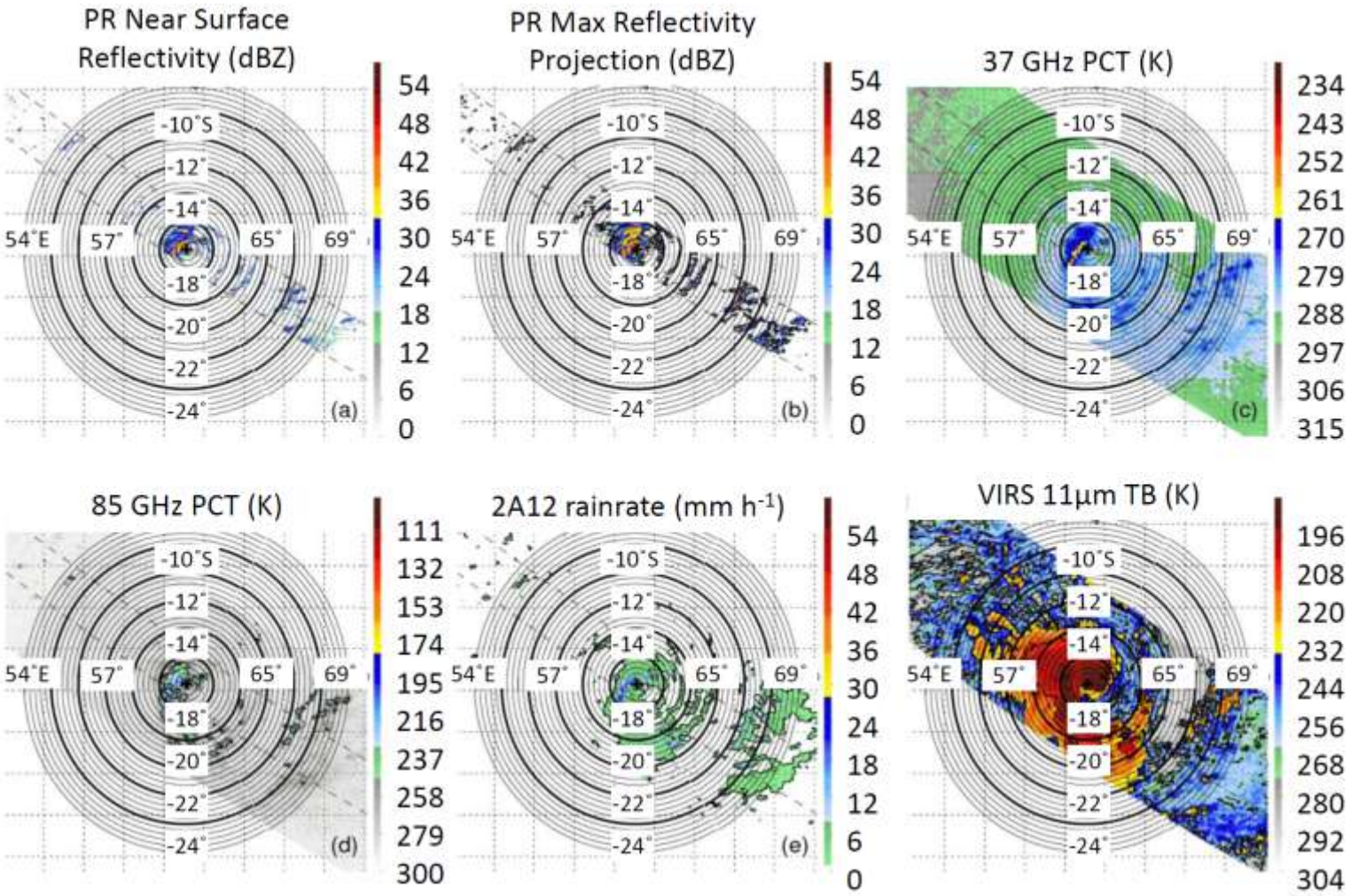

Figure 2.4. Same as Fig. 2.1 except for Tropical Cyclone Crystal (current maximum wind speed 74 kts) of the Southern Indian Ocean basin at 1300 UTC 25 December 2002.

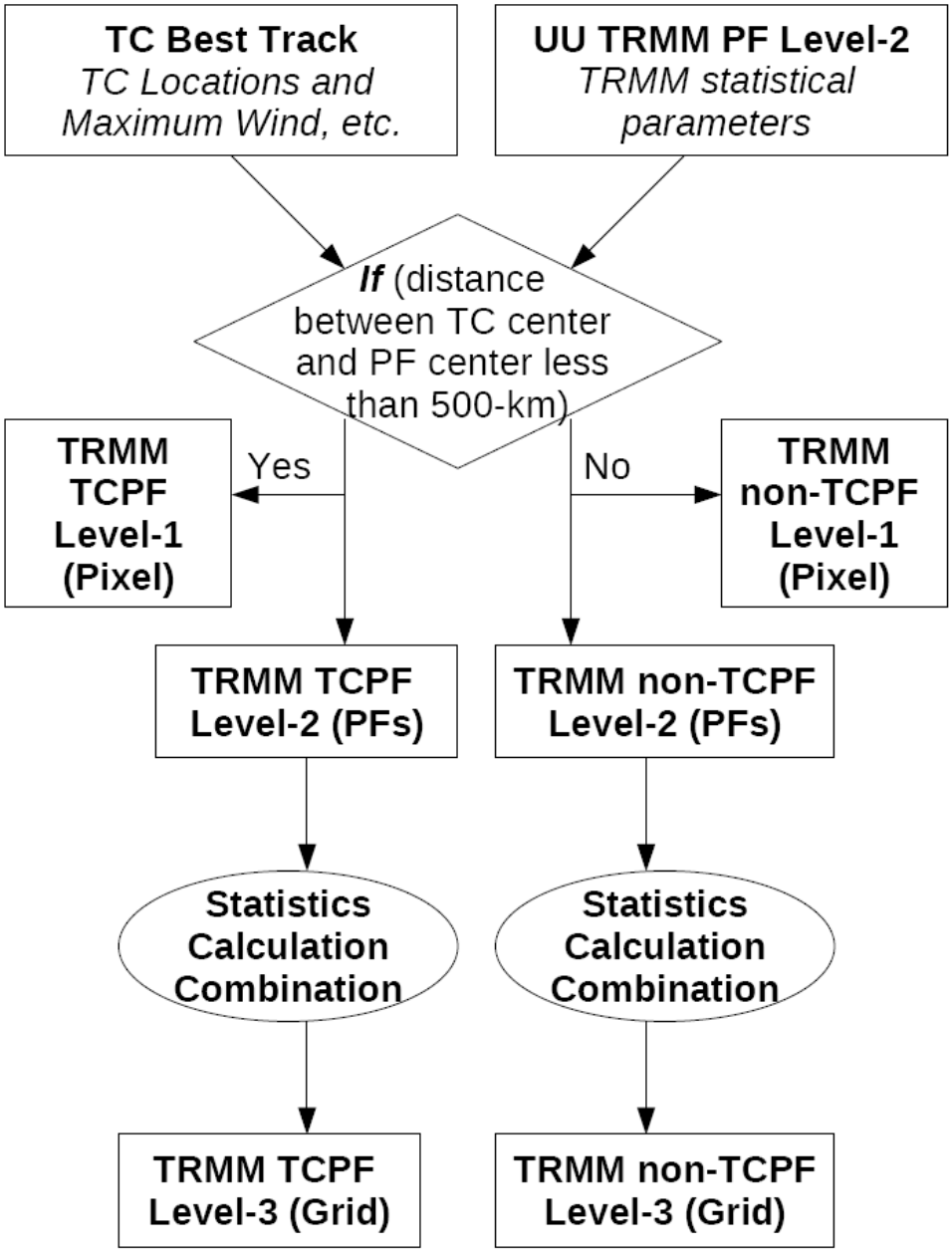

Figure 2.5. FIU/UU TRMM TCPF database construction flow chart (Jiang et al. 2010).

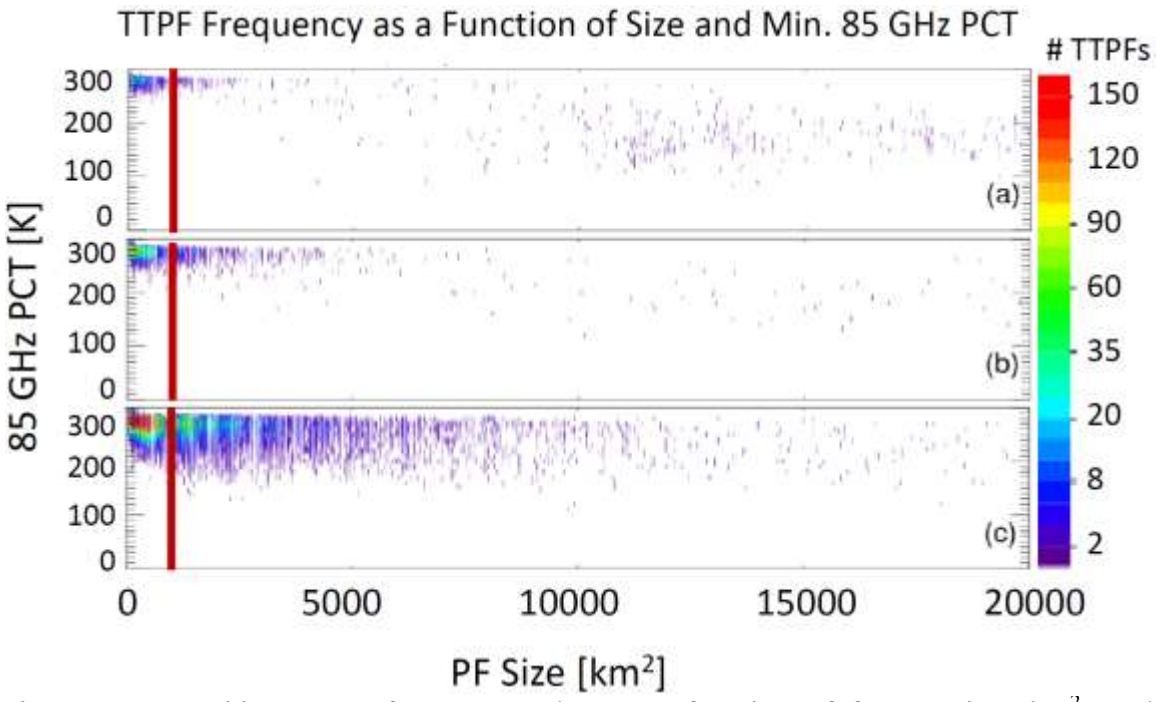

Figure 2.6. 2-D histogram of TTPF number as a function of feature size [km^2] and minimum 85 GHz PCT [K] for (a) IC (b) IB and (c) OB TTPFs. The red line is marked at PF size equal to 1000 km^2.

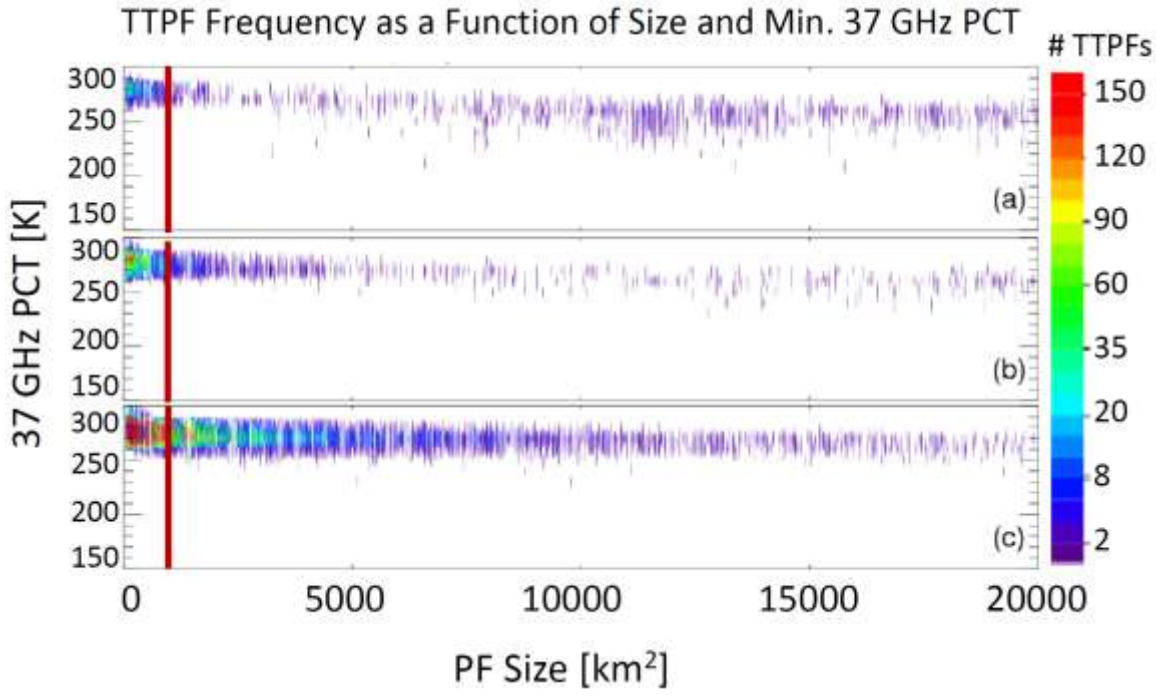

Figure 2.7. Same as Fig 2.6 except for minimum 37 GHz PCT.

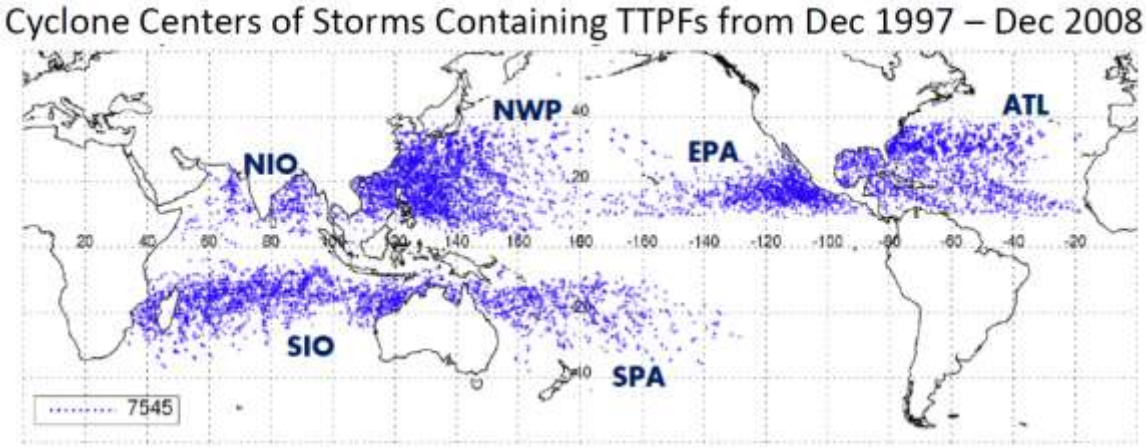

Figure 2.8. Storm centers of TRMM TMI TC overpasses from 1997-2008. The Northwest Indian Ocean (NIO), Northwest Pacific (NWP), East Pacific (EPA), Atlantic (ATL), Southern Indian Ocean (SIO), and South Pacific (SPA) basins are labeled.

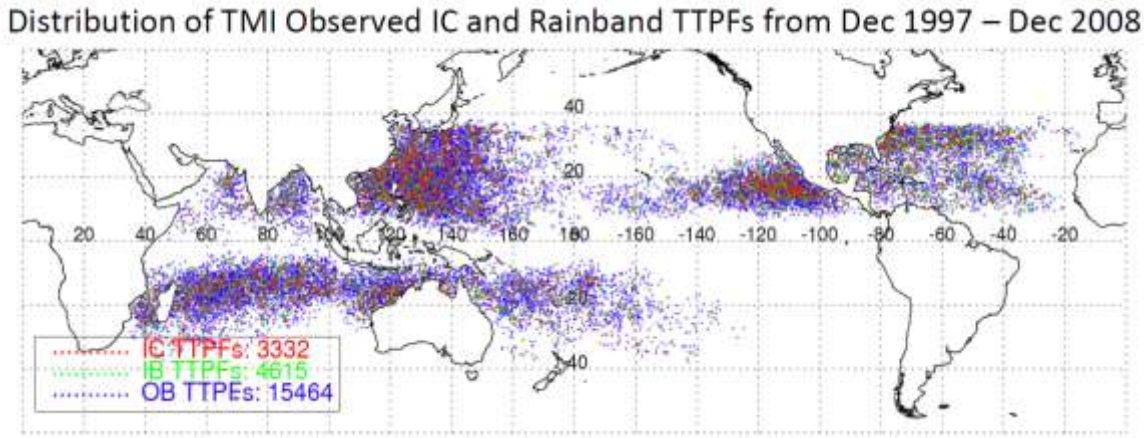

Figure 2.9. Geographic distribution of TTPFs in the IC, IB, and OB TC regions.

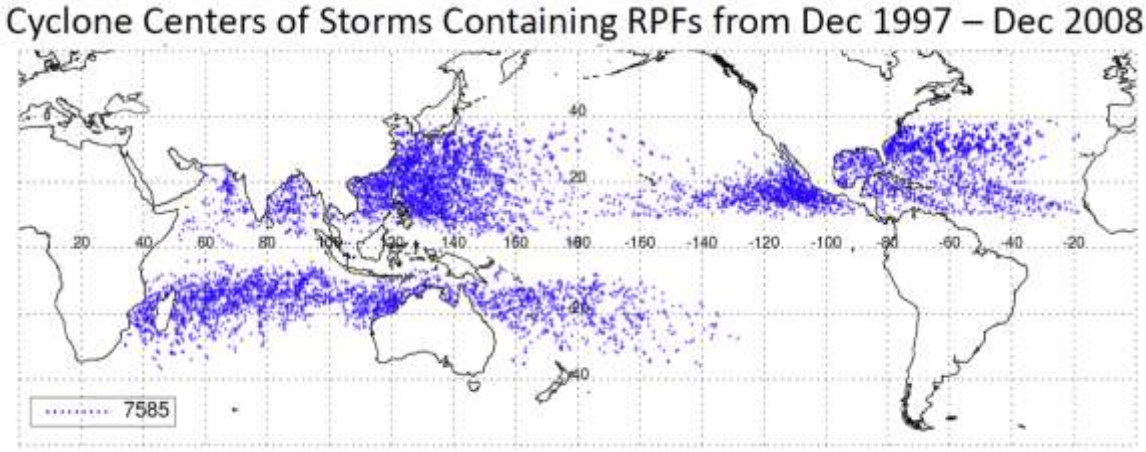

Figure 2.10. Storm centers of TRMM PR TC overpasses from 1997-2008.

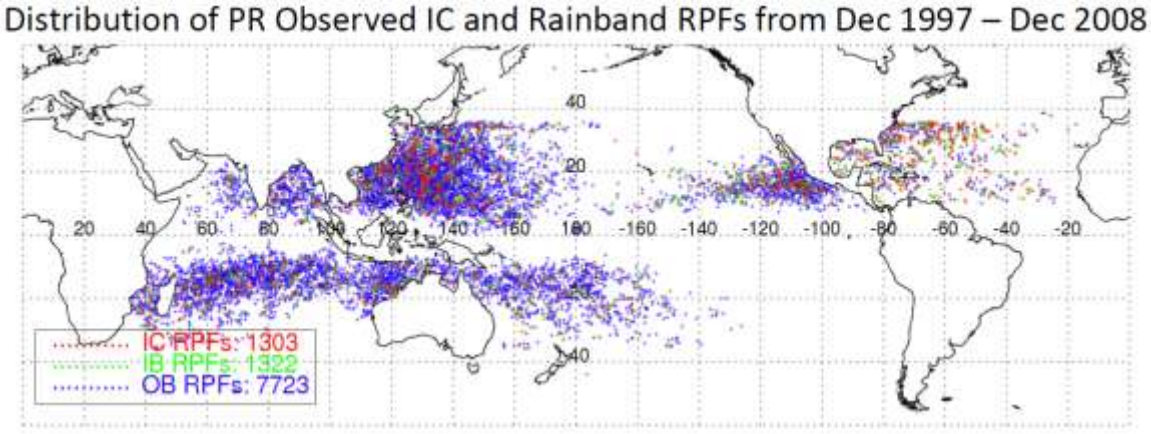

Figure 2.11. Geographic distribution of RPFs in the IC, IB, and OB TC regions.

Table 2.1. The mean and standard deviation radial extent of each TC region.

Radii	Mean (km)	Standard Deviation (km)
IC	82	18
IB	162	27
OB	502	129

Table 2.2. Excerpt of precipitation feature database description from Jiang et al. (2010)

	Acronyms	Definitions	Criteria	12-y Total Population	12-y TCPF Population
Precipitation Features	RPF	PR feature in PR swath	2A25 rainfall rate > 0	26,523,461	239,375
	TTPF	TMI feature in TMI swath	2A12 rainfall rate > 0	13,649,884	95,956

Table 2.3. Orbit and TTPF populations seen by the TMI swath from 1997-2008. The TMI swath dataset used in this study is constrained to include TCPFs whose parent cyclone IC, IB, and OB were captured at 100%, 100% and 60%, respectively.

	Orbits	TTPFs
IC Sample	7545	3338
100 % IC Capture by TMI	**5891**	**3332**
% of respective sample	84.6	99.8
IB Sample	7545	5235
100 % IB Capture by TMI	**4549**	**4615**
% of respective sample	65.3	88.2
OB Sample	7545	19557
60 % OB Capture by TMI	**5670**	**15464**
% of respective sample	81.4	79.1
Total Sample	7545	28130
Total restricted sample	7545	23411

Table 2.4. Orbit and RPF populations seen by the PR swath from 1997-2008. The PR swath dataset used in this study is constrained to include TCPFs whose parent cyclone IC, IB, and OB were captured at 80%, 70% and 30%, respectively.

	Orbits	RPFs
IC sample	7585	2637
80 % IC capture by PR	**1387**	**1303**
% of respective sample	18.2	49.4
IB sample	7585	4357
70 % IB Capture by PR	**1133**	**1322**
% of respective sample	14.9	28.5
OB sample	7585	15921
30 % OB capture by PR	**3174**	**7723**
% of respective sample	41.6	48.5
Total sample	7585	22915
Total restricted sample	7585	10348

CHAPTER 3

CONVECTIVE AND RAINFALL PROPERTIES OF INNER CORE AND RAINBAND REGIONS

3.1 TMI: Polarization Corrected Brightness Temperatures and 2A12 Rainfall

The cumulative distribution functions (CDFs) of minimum 37 GHz and 85 GHz PCTs and 11μm Tb are presented in Fig. 3.1. The IC features generally have colder 85 GHz PCTs than IB and OB features (Fig. 3.1a). Median values of minimum 85 GHz PCT in IC, IB, and OB features are 183 K, 203 K, and 244 K, respectively. Spencer et al. (1989) found the 85 GHz PCT range of 250 – 260 K to be a proxy for precipitation, with 250 K corresponding to roughly 3 mm h^{-1}. Cecil et al. (2002) found approximately 80% of eyewall features and 15% of inner and outer rainband features to have minimum 85 GHz PCT less than 250 K, while this study observes 86%, 80%, and 54% in IC, IB, and OB regions, respectively. While the sample size here is dramatically larger (with 3332 IC features) than that in Cecil et al. (2002, with only 104 eyewall features), differences are mainly attributed to the current 1000 km^2 size restriction which was not used in Cecil et al. (2002). Mohr and Zipser (1996a,b) used an SSM/I 85 GHz PCT pixel of 225 K to indicate convection. Approximately 41% of OB features have minimum 85 GHz PCT falling below this threshold, as do 70% of IB features and 77% of IC features. Consistent with the findings by Cecil et al. (2002), the IC features appear to produce strong ice scattering signatures more often than IB and OB features. Cecil et al. (2002) also suggest

that the distributions for IB and OB features become more like those of the eyewall region after removing small features. However, Fig. 3.1 indicates that feature distributions in the IC region are still very different than those for IB and OB regions, even with the current 1000 km^2 size restriction.

The IB feature distribution shown in Fig. 3.1 may be skewed towards lower PCTs from IC contamination. Contrarily, the OB feature distribution is assuredly skewed towards higher temperatures from the high population of small and warm features that have been acknowledged as characteristic of this region (Cecil et al. 2002, Cecil and Zipser 2002). Upon closer inspection of the stronger end of the convective spectrum, particularly with minimum 85 GHz PCT < 150 K, it is found that the IC region features still have the highest percentage (25%) of minimum 85 GHz PCTs below 150 K, while the percentages in IB and OB features are comparable to each other (10 and 13%) and a factor of 2 fewer than that in IC. The OB region features produce strong ice scattering more often than the IB features with minimum 85 GHz PCTs between 100-150 K. The OB feature distribution is a few Kelvin colder than the IB feature distribution in that range, but the IC feature distribution is still the coldest. A more strict restriction is applied as follows to compare the strongest portions of the convective spectrum in features in the IC, IB, and OB regions: MCS (mesoscale convective system) TTPFs are defined in features containing a 2000 km^2 area of 85 GHz PCT less than 250 K and a 200 km^2 area less than 225 K. CDFs of minimum 85 GHz PCT in MCS TTPFs in the IC, IB, and OB regions (not shown) indicate that with minimum 85 GHz PCT ≥ 110 K, the OB region produces strong ice scattering slightly more often than the IC region, but much more often than the IB region. Median values are approximately 148, 152, and 175 K in

OB, IC, and IB regions, respectively. However, in those parts of the plots with minimum 85 GHz PCT ≤ 110 K, features in the IC region produce strong ice scattering slightly more often than those in the OB region.

Median minimum 37 GHz PCT values among TC regions have a much narrower spread with median values of 260 K in IC, 263 K in IB, and 274 K in OB features (Fig 3.1b). However, the IC region has 23% of TTPFs with minimum 37 GHz PCT below 250 K, while the IB and OB have only 10%. This implies that updrafts in the IC region are often strong enough to produce large ice hydrometeors. At the colder end of the plots, minimum 37 GHz PCT CDFs show similar characteristics as those in the distributions of minimum 85 GHz PCT for the differences among IC, IB, and OB regions. The IR 11μm Tb is a good indicator of cloud top height. Fig. 3.1c shows that the cloud top heights of IC TTPFs are higher than those in IB TTPFs, which is higher than those in OB TTPFs, with median values of minimum 11μm Tb of 197 K in IC, 201 K in IB, and 220 K in OB. Note that IB minimum 11μm should be especially contaminated by IC clouds that are sloped outward.

Minimum brightness temperatures are extreme values which represent just one pixel in a PF. The percentage of area satisfying a given PCT threshold is perhaps a more appropriate convective proxy. Size distributions (Fig 3.2a) spotlight the enormous difference between OB versus IC and IB TTPFs. Fig 3.2b-c indicate that IC TTPFs contain a larger percentage of area with 85 GHz PCT less than 250 K and 225 K, followed by IB, then OB TTPFs. This is similar to Cecil et al. (2002) which found that 45% (37%, 28%) of IC (IB, OB) pixels have 85 GHz PCT less than 250 K. At median, one quarter of IC feature area is comprised of 85 GHz pixels below 250 K, one tenth of

IB feature area, and no area for OB. This concludes that at least half of large OB features have no pixels < 250 K, indicating that high PCT values associated with minimal ice comprise a large portion of the OB region. Approximately 27% (41%, 65%) of the IC (IB, OB) features have either no area, or less than 1% of their area < 225 K (Fig. 3.2c). Overall, features from the IB region have a higher percentage of area that meets the convective threshold of 225 K than features from the OB region. Conversely, when implementing a 200 K threshold (not shown) the IB produces strong ice scattering least often.

The IC region features produce the highest mean conditional rain rates, followed by the IB and OB region features, with median rain rates of 4.5 mm h^{-1}, 3.1 mm h^{-1}, and 1.6 mm h^{-1}, respectively.

3.2 PR: Vertical Profiles of Radar Reflectivity and 2A25 Rainfall

To compare the vertical profiles of radar reflectivity in IC, IB, and OB regions, contoured frequency by altitude diagrams (CFADs, Yuter and Houze 1995) of *maximum* radar reflectivity for RPFs is derived from the 11-y TRMM TCPF database and plotted in Fig. 3.4. From Fig. 3.4a-c, the median heights of the 20 dBZ echoes are 12.5 km, 11.5 km, and 9.5 km in IC, IB, and OB RPFs, respectively, while the median maximum near surface reflectivities are 48 dBZ, 44 dBZ, and 42 dBZ in IC, IB, and OB RPFs, respectively. The top 10% of the 20 dBZ echo height in IC RPFs is 16.5 km, which is distinctly higher than that in IB and OB RPFs, which is roughly 15 km. The IC maintains higher altitudes at all dBZ thresholds. The IB exhibits the most clear brightband at about 5 km, which is seen by an increase in reflectivity followed by sharp decreases in reflectivity with height, and is indicative of stratiform rain. For clarification, since all

CFADs represent the maximum reflectivity, the stratiform characteristics should be under-represented. Cecil et al. (2002) separated stratiform and convective pixels in each TC region to show that stratiform precipitation is most readily found in the rainband regions and that convective precipitation most commonly occurs in the cyclone core.

A more convenient comparison of vertical reflectivity profiles is accomplished by overlaying the median and 90th percentile profiles of each TC region in Fig. 3.5. Hence and Houze (2010) studied mature hurricanes eyewalls from 1998-2007 and found them to have the highest reflectivites, echo tops, and a relatively uniform vertical profile of reflectivity compared with rainband regions. Consistent with their study, Fig. 3.5 shows that both the median and 90th percentile profiles are the strongest in the IC region. However, although the median profile is stronger in the IB than the OB region, the 90th percentile profiles of the IB and OB region are comparable. This is consistent with the result from passive microwave ice scattering signatures shown in Fig. 3.1. From Fig. 3.5, the brightband, characterized by enhanced radar echoes at the melting level, again, is most noticeable in the IB region.

The magnitudes of PR 2A25 rain rate (Fig. 3.6) are almost a factor of two greater than TMI 2A12 rain rate distributions (Fig 3.3). It is likely that the differences in rain rate are inherent within the PR and TMI algorithms. Cecil and Wingo (2009) examined TC rain retrievals from four algorithms, including version 6 of PR 2A25 and TMI 2A12, and found that 2A25 produces the highest estimates when averaged over the 0-100 km radius, because it assigns much higher rain rates, up to 100 mm h^{-1} in grid boxes with the heaviest rain. Estimates from the 2A12 algorithm were the lowest, most often assigning grid boxes to 5 mm h^{-1} rain rate. Discrepancies were reduced when averaged further

outward and in weaker tropical cyclones. The differences can also be attributed to pixel size, as the higher resolution of PR data better represents, though not fully, the most heavily raining portions of convective cells. The highest rain rates are observed in the IC region features. Median rain rates are 7.0 mm h^{-1}, 4.2 mm h^{-1}, and 3.4 mm h^{-1} in IC, IB, and OB RPFs, respectively.

3.3 Lightning

Cecil et al. (2005) found that in a 3-y record of TRMM observed PFs that only 2.4% contained a flash. If their distribution was extrapolated to flash rates below the minimum detectable signal of 0.7 fl min^{-1}, it suggests that up to 10% of PFs may contain lightning. Data from 1998-2009 of TMI observed PFs show that 4.1% recorded a flash, that is 10.3% in only features over land and 1.7% in only features over ocean. Constrained by only the oceanic TTPFs (e.g., associated with a TC), lightning is observed in 4.6% of this work's sample (Table 4.1). For comparison, 8.5% of TTPFs over land recorded a flash. Note that in this section, not all electrically active features are represented, just the ones that managed to produce a flash within the relatively short 80 second TRMM LIS view time. The minimum 1000 km^2 size restriction in TTPFs or RPFs does not apply for this section. If the LIS records a lightning flash, then the other TRMM instruments likely captured the conditions associated with the lightning, regardless of feature size.

There are 2,895 lightning flashes within the 12-y TRMM TC TTPF sample and the majority of them (74%) occur in the OB region. The IC region, however, has the highest percentage of TTPFs with a flash at 9.5%, followed by the IB at 4.7% and OB at 4.2%, though TCs have been proven to contain relatively little lightning compared to

tropical continental features (Toracinta et al. 2002, Cecil et al. 2002). The likelihood of a PF having lightning is 40 times greater over land than over ocean (Cecil et al. 2005). To further describe the rarity of electrical discharges in hurricanes, Molinari et al. (1999) continuously monitored 4 moderate to strong Atlantic hurricanes with the National Lightning Detection Network (NLDN) and found that 93% of hourly flash counts amounted to 0. That study was limited to storms with TC centers within 400 km of the coast because the detection efficiency of the NLDN decreases sharply with distance. Therefore some TCs may have land interference. The advantage here is that the majority of TCs are in the open ocean. For the TTPFs that have lightning, the 2-D distributions of lightning flash counts as a function of minimum 85 and 37 GHz PCTs are examined (Fig. 3.7). Since the production of lightning requires ice particle collisions in the presence of supercooled liquid water in the mixed phase region, the occurrence of an electrical discharge is plotted with regard to minimum PCT, an indicator of ice scattering..

Two points from Fig. 3.7 are evident: (1) Lightning occurs in a wide spectrum of PCT values, but is most prevalent in colder PCTs, especially below the 85 GHz PCT of 100 K and (2) Features in the OB region are likely to have more flashes, on average, for a given PCT bin. Molinari et al. (1999) investigated lightning in 9 Atlantic basin hurricanes, binning roughly every 30 km outward from the TC center, and discovered that the area outward of 140 km in mature hurricanes contained the highest strike density. A secondary maximum was found from 0-60 km, and a clear minimum 80-100 km outside the TC center with approximately 2-6 times fewer strikes. Case studies of coastal tropical storm and hurricane events from Lyons and Keen (1994) also conclude that lightning is most common in the outer rainbands. Figure 3.7 corroborates those findings,

but also demonstrates that they may apply in general to the global population of TCs. An explicit flash density maximum lies within the OB, followed by the IC and IB. However, the IB is not quite as electrically dormant as previous works have stated. Black and Hallett (1999) argue that IC lightning should be infrequent due to high volumes of ice in a mature hurricane that act to freeze the supply a supercooled liquid water. TCs are great producers of mid tropospheric ice (Houze 2010). Ice particles from higher levels come in contact with super cooled liquid droplets that freeze by contact nucleation and further grow by riming (Houze 2010). Black and Hallett (1986) call this an "ice multiplication" process. These observations and hypotheses show cause for a relative minimum in observed lightning, except where the most vigorous updrafts exist. The lack of lightning in the IB (Fig. 3.7) therefore makes sense and is consistent with the results of Molinari et al. (1999), Cecil et al. 2002, and Cecil and Zipser 2002. So the question remains, what makes the OB more electrically active than the IC? Are not the updrafts just as strong in the core? Lyons and Keen found that lightning in a hurricane eyewall is scarce because the nature of cloud dynamics within the interior of a mature TC is different from that of isolated convective storms. Houze (2010) suggests that although not studied, the lightning on the outer fringes of TCs is likely similar to that of ordinary thunderstorms, but IC dynamics are unique. Particles circumnavigate the storm about 1.5 times as they advect up and radially out, and are then ejected by aggregation and sedimentation processes. Figure 3.7 merely illustrates the flash densities for given PCT combinations in features that observed lightning. It is equally important to quantify the fraction of features with lightning at those same PCTs.

Squires and Businger (2008) found that TRMM 85 GHz PCTs displayed a correspondence with eyewall lightning, though PCTs are not a sufficient discriminator. When lightning *was* detected there were always low PCTs collocated, making them perhaps a necessary condition. Probabilities of lightning at given minimum 85 GHz and 37 GHz PCTs are examined to find out how often an observed PCT will produce an electrical discharge (Fig. 3.8). Despite having seen earlier that the IC contains the highest fraction of cold PCT pixels, it does not attain the highest flash counts. Cecil and Zipser (2002) found that in the OB region, the 85 GHz PCT must fall below 200 K and the 37 GHz PCT below 265 K before the likelihood begins to increase. Similar values of 210 K and 270 K are found in Fig. 3.8. In both the IC and IB regions, these respective thresholds are 180 K for 85 GHz and 255 K for 37 GHz. At minimum 85 GHz PCT of 150 K, 37% of OB, 23% of IB, and only 14% of IC features have lightning. At 37 GHz PCT of 235 K, 70% of OB and 42% of IC and IB features have lightning.

Figure 3.8 shows that for a given minimum PCT that an OB feature is more likely to contain a flash than an IC or IB feature with the same minimum values. Molinari et al. (1999) suggest the outer maximum is attributed to the relatively unstable air around the storm compared to the core. Khain et al. (2008) suggest that lightning is common in the OBs but exists in the IC only during replacement cycles. They also concluded through modeling studies that instability is a necessary but probably not sufficient condition for lightning. Aside from the influence of ice near the IC, high near-center winds loaded with large sea salt particles might inhibit the strength of the updraft and subsequently favor a more efficient warm rain process. Or, perhaps salt composition in some way alters the

electrification process by modifying the droplet number concentration or size distribution.

Another approach to doing lightning statistics is to normalize the number of flashes by various convective criteria. Cecil et al. (1999), using observations from the optical transient detector (OTD), found that the lightning production in the eyewall is comparable to that in the OB region, similar to Cecil and Zipser (2002). However, Squires and Businger (2008) showed the strike density for eyewall versus OB to be 6:1 for Rita and 1:1 for Katrina. Note that case studies (especially category 5 storms), however, do not often compare well with robust statistics. The 0-25 km bin of Rita contained over 5600 strikes in a 3-d period, about 7 times larger than any OB bin (25 km bins out to 300 km) over the same observation period. Is this surprising? Not really, because any specific storm cannot be expected to mirror the statistical summary of a large numbers of storms. When Cecil et al. (2002) documented various aspects of sample size to flash count they found that the OB had the most flashes per precipitating area, convective certain area, 85 GHz PCT area less than 215 K, and 37 GHz PCT area less than 263 K. However their study was completed with about 2% of the sample size used in this work. As shown in Table 3.2, the IC 2A12 raining area per lightning flash is roughly half of that in the OB and about a quarter of that in the IB. This is different from Cecil et al. (2002) in which the IC and OB 2A25 raining areas per lightning flash were comparable and about a quarter of that seen in the IB. In Table 3.2, the IC and OB 2A12 volumetric rains per lightning flash are comparable and about one third of that in the IB region, while Cecil et al. (2002) found that 2A25 volumetric rain per flash in the OB region was about two fifths of that in the IC. Also examined are 85 GHz PCT area less

than 250 K and 225 K and 11μm Tb area less than 235 K and 210 K. For the weaker convective constraints, e.g., area 85 GHz PCT < 250 K and area 11μm Tb < 235 K, the IC and OB are comparable and have about 3 times *more* lightning than the IB. Interestingly, for the stronger convective constraints, e.g., 85 GHz PCT < 225 K and 11μm Tb < 210 K, the OB has *more* lightning than the IC by a factor of 1.5 and 2, respectively. This is consistent with findings from the earlier lightning probabilities as a function of minimum PCTs, that for a convective restriction the OB features are more likely to have a flash. The likelihood of a flash significantly increases for OB minimum 85 GHz PCTs below 210 K while it takes PCTs down to 180 K before the IC and IB probabilities begin to rise.

Lightning occurrence in PR detected features among varying TC regions is summarized in Table 3.3. The IC has the highest percentage of PFs with a flash at 3.5%, followed by both the IB and OB at 1.1%. The vertical profiles of maximum radar reflectivity in each TC region for RPFs with lightning are presented in Fig. 3.9. The 50^{th} percentile of maximum radar reflectivity in the IC region is even stronger than the 80^{th} percentile and only slightly weaker than the 90^{th} percentile in IB and OB regions. It shows that in order to produce lightning, the IC region features must have much stronger radar echoes than those in IB and OB regions.

Black and Hallett (1986) observed the type and distribution of particles above the zero degree isotherm in 3 Atlantic hurricanes. They concluded that supercooled liquid drops were found only in convective updrafts stronger than 5 m s^{-1}, but not all updrafts stronger than 5 m s^{-1} contained appreciable liquid. The three case studies also revealed that except in the strongest updrafts, hurricane convection is largely glaciated at

temperatures as warm as -5 C, and most hurricanes contain graupel as warm as -2 C. This leads to speculation that most liquid water that reaches the 0 degree isotherm is frozen well below the -10 C isotherm, which is contrary to tropical continental convection where ice particles are rare in updrafts below the -10 C isotherm. Jorgensen et al. (1985) identified an updraft range of 4-6 m s^{-1} for mature TCs. Zipser and Lutz (1994) propose as a necessary condition for rapid electrification, based on field experiment data, that a convective cell must have updrafts of 6-7 m s^{-1} for mean speeds and 10-12 m s^{-1} for peak speed. Therefore it should be very difficult to produce lightning as those vertical speeds are identified as uncommon in hurricanes. If high reflectivities exist above the freezing level then it is hypothesized that updraft strength is sufficient for supercooled liquid water to be lofted into the mixed phase region. The probabilty of lightning in features with respect to their maximum radar echoes at 6 km height, 8 km height, 10 km height, and 12 km height is shown in Fig. 3.10. Results show that the OB has between a 10-25% higher likelihood of lightning than features in the IB and OB for a given maximum dBZ at all altitiude levels.

Flash rates are examined for correlations with feature minimum PCTs, maximum reflectivites, and area of echoes for all TTPFs with lightning (Fig. 3.11). Flash rate is slightly more correlated to the 37 GHz PCT than the 85 GHz PCT. While the correlations are not substantial, they are definitively nonzero. Correlations of similar magnitude to that between flash rate and minimum 85 GHz PCT are found between flash rate and maximum reflectivity at 9 km. Xu et al. (2010) found that radar echoes at 8-9 km altitude are a good indicator of ice hydrometeors and supercooled liquid water, and therefore of lightning production. The highest correlation with lightning flash rate was 0.61, and was

achieved with the area of the 35 dBZ echo at 9 km. Using the onboard aircraft radar, Long-Range Lightning Detection Network (LLDN) data, and TRMM data, Squires and Businger (2008) found that lightning strikes were observed to coincide with maxima in radar reflectivity. Results in Fig. 4.11c and d indicate that the maximum reflectivity is not as important as the area of a strong echo.

Squires and Businger (2008) also show that aircraft radar reflectivity exhibits the highest spatial correlation with lightning strikes, in particular 30 dBZ reflectivities at altitudes 7 km or greater. Figure 3.12 shows the correlation coefficients of lightning flash rate with area of radar reflectivity at certain values at a given altitude. Collectively, the IC and IB have correlations less than 0.10 at altitudes less than 5 km. Differently, the OB region has correlations up to 0.35 at altitudes less than 5 km. The OB is the only region to experience what would be called traditional convection. The highest correlations for the IC occur in a broad region between 6 – 9 km and reach up to 0.60 and over a broad range of reflectivities centered near 32 dBZ. The IB reaches its highest correlations between 8 – 11 km centered near 35 dBZ with correlations up to 0.70. The OB attains the highest correlation, 0.80, between 6 – 8 km, just above the freezing level for reflectivities 35 – 40 dBZ.

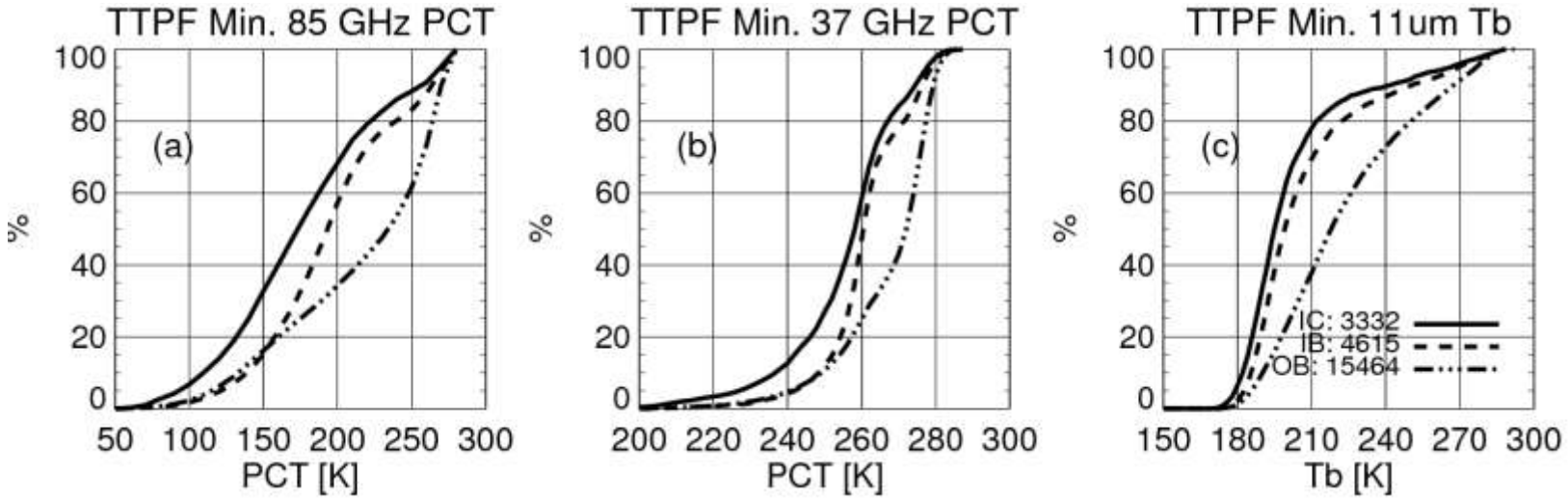

Figure 3.1. Cumulative distribution functions (CDFs) for (a) minimum 85 GHz PCT [K] (b) minimum 37 GHz PCT [K] and (c) minimum 11μm brightness temperature [K] for TTPFs in the IC, IB, and OB TC regions.

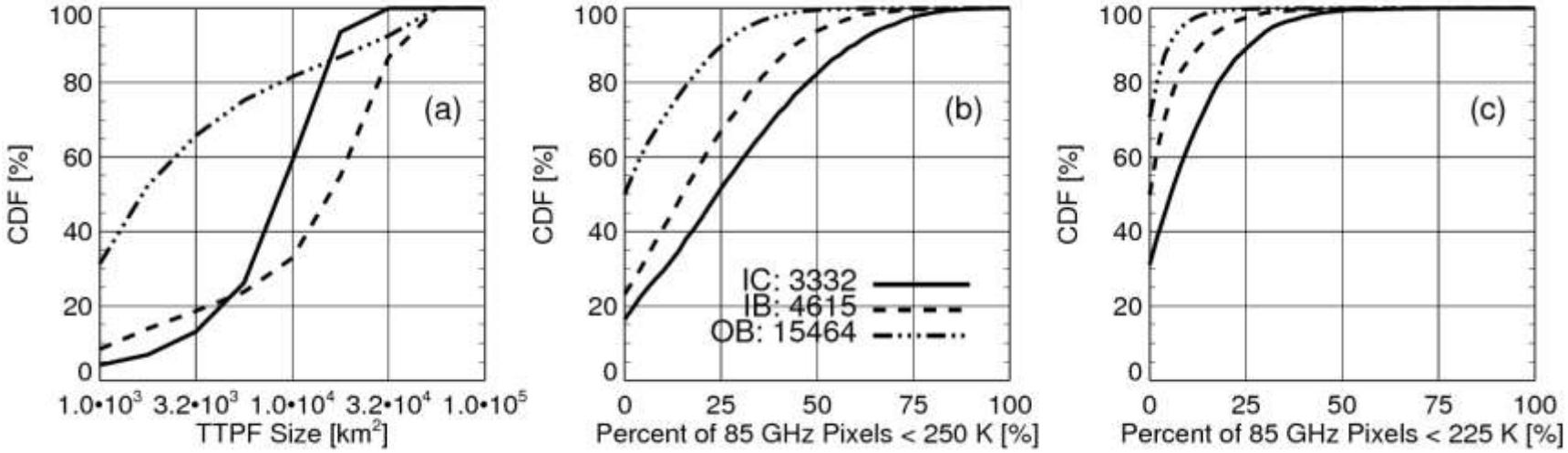

Figure 3.2. CDFs of (a) TTPF size [km^2] (b) percent of 85 GHz PCT pixels less than 250 K [%] and (c) percent of 85 GHz PCT pixels less than 225 K [%] for TTPFs in the IC, IB, and OB TC regions.

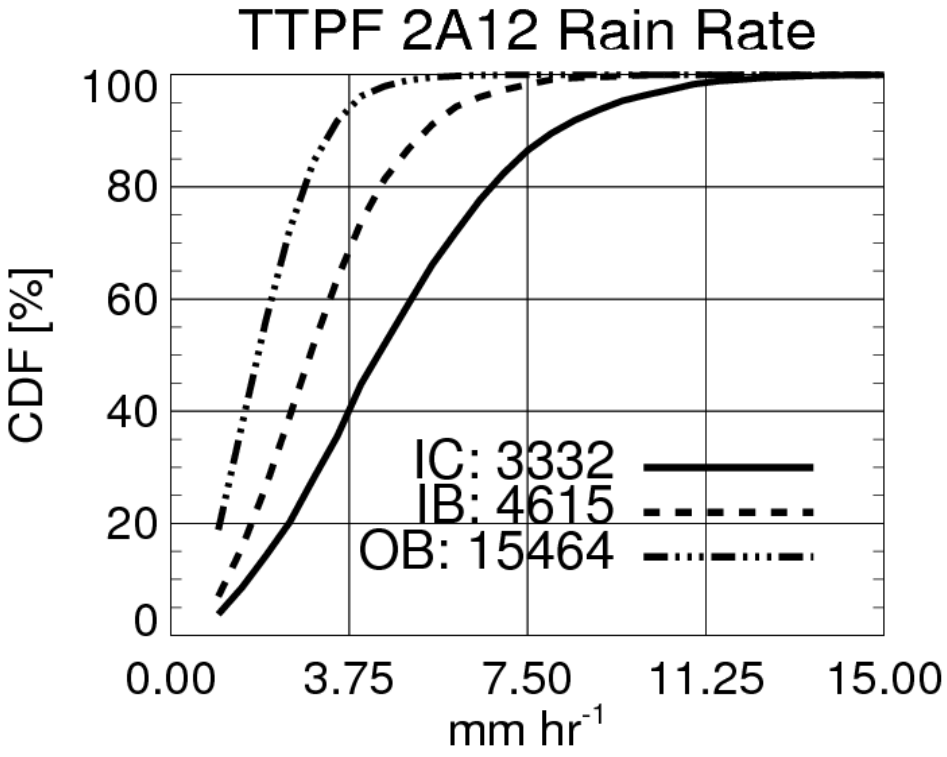

Figure 3.3. CDFs of TMI 2A12 rain rate for TTPFs in the IC, IB, and OB TC regions.

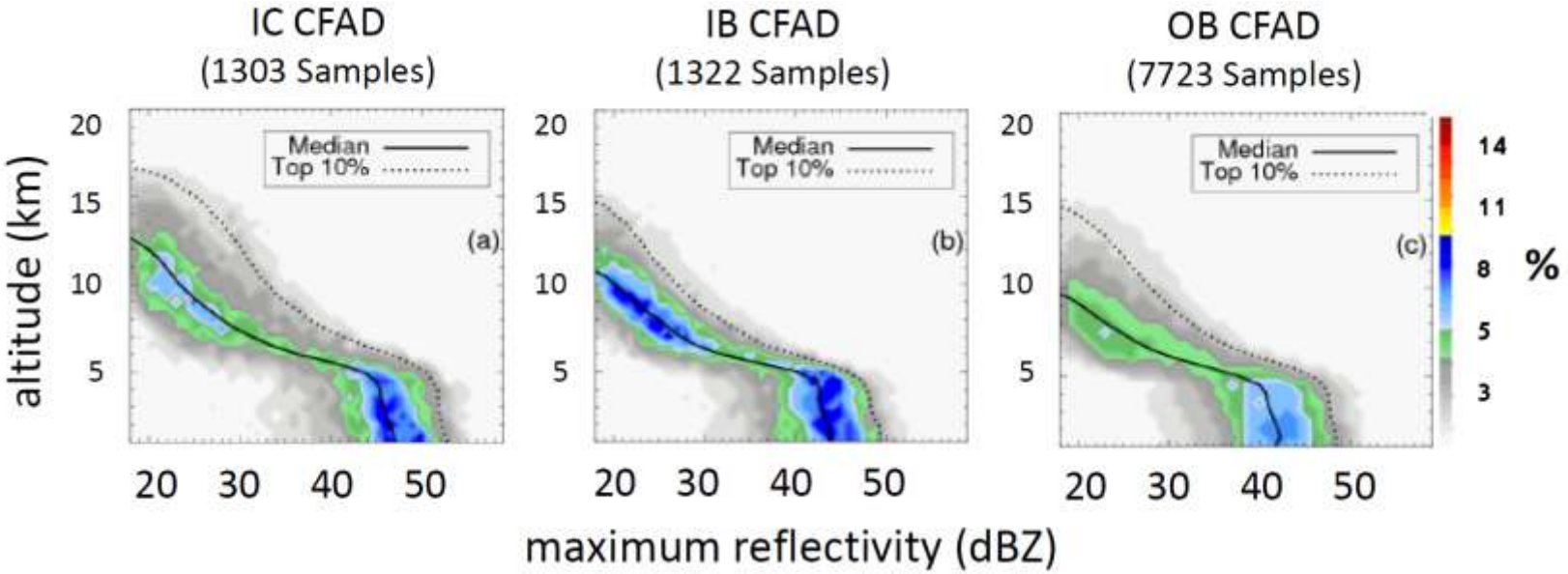

Figure 3.4. Contoured frequency by altitude diagrams (CFADs) of maximum radar reflectivity for (a) IC RPFs (b) IB RPFs and (c) OB RPFs. The median maximum reflectivity profile is indicated by the solid black line and the top 10 % of maximum reflectivity profile is indicated by the dashed line.

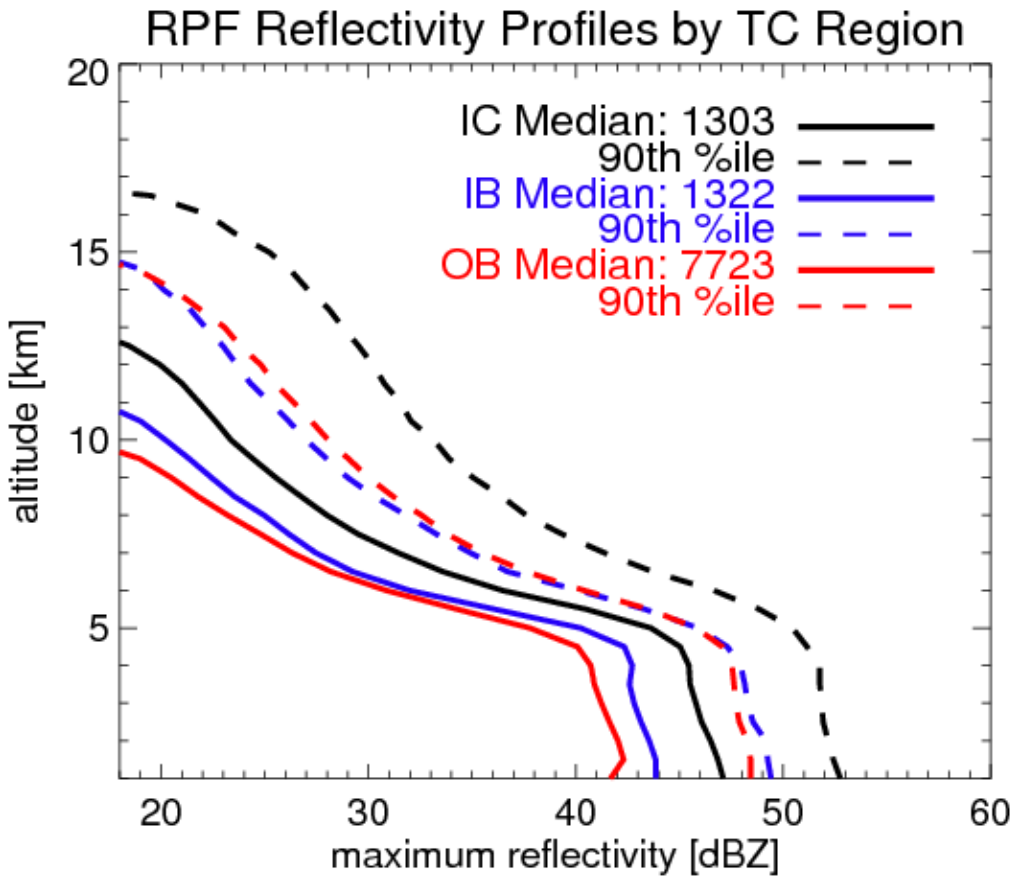

Figure 3.5. Median (solid lines) and 90th percentile (dashed-dotted) of vertical profile of maximum radar reflectivity in IC, IB, and OB TC regions.

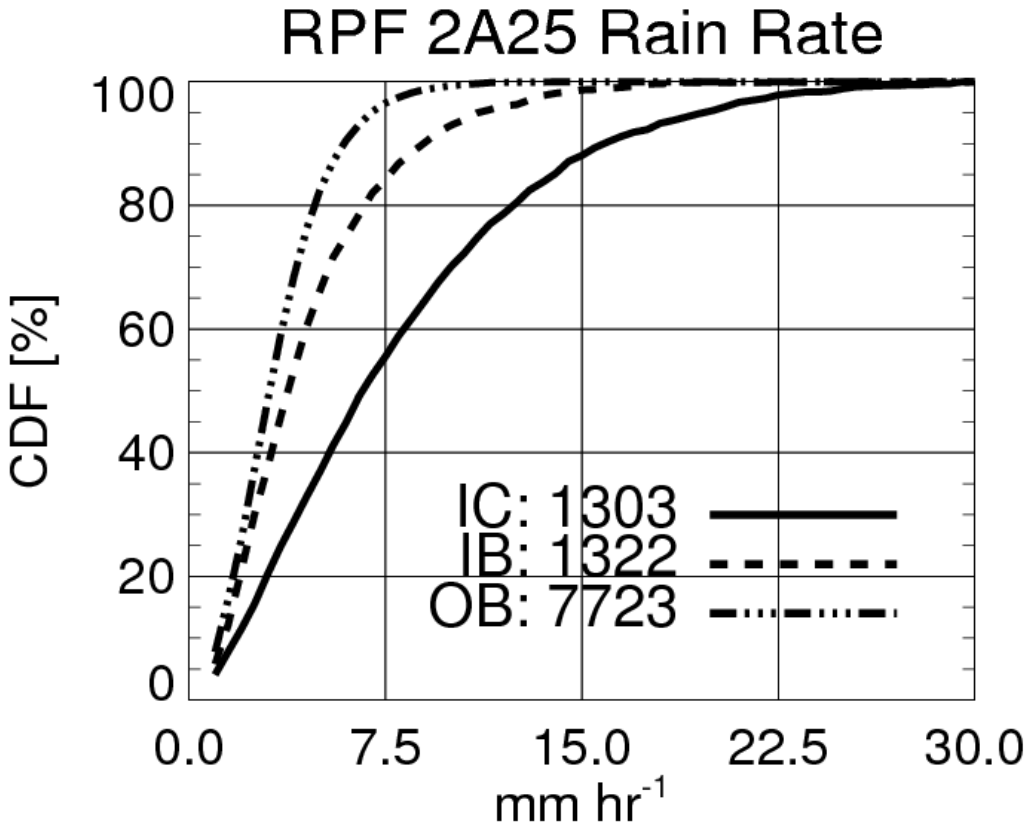

Figure 3.6. CDFs of PR 2A25 rain rate for RPFs in the IC, IB, and OB TC regions.

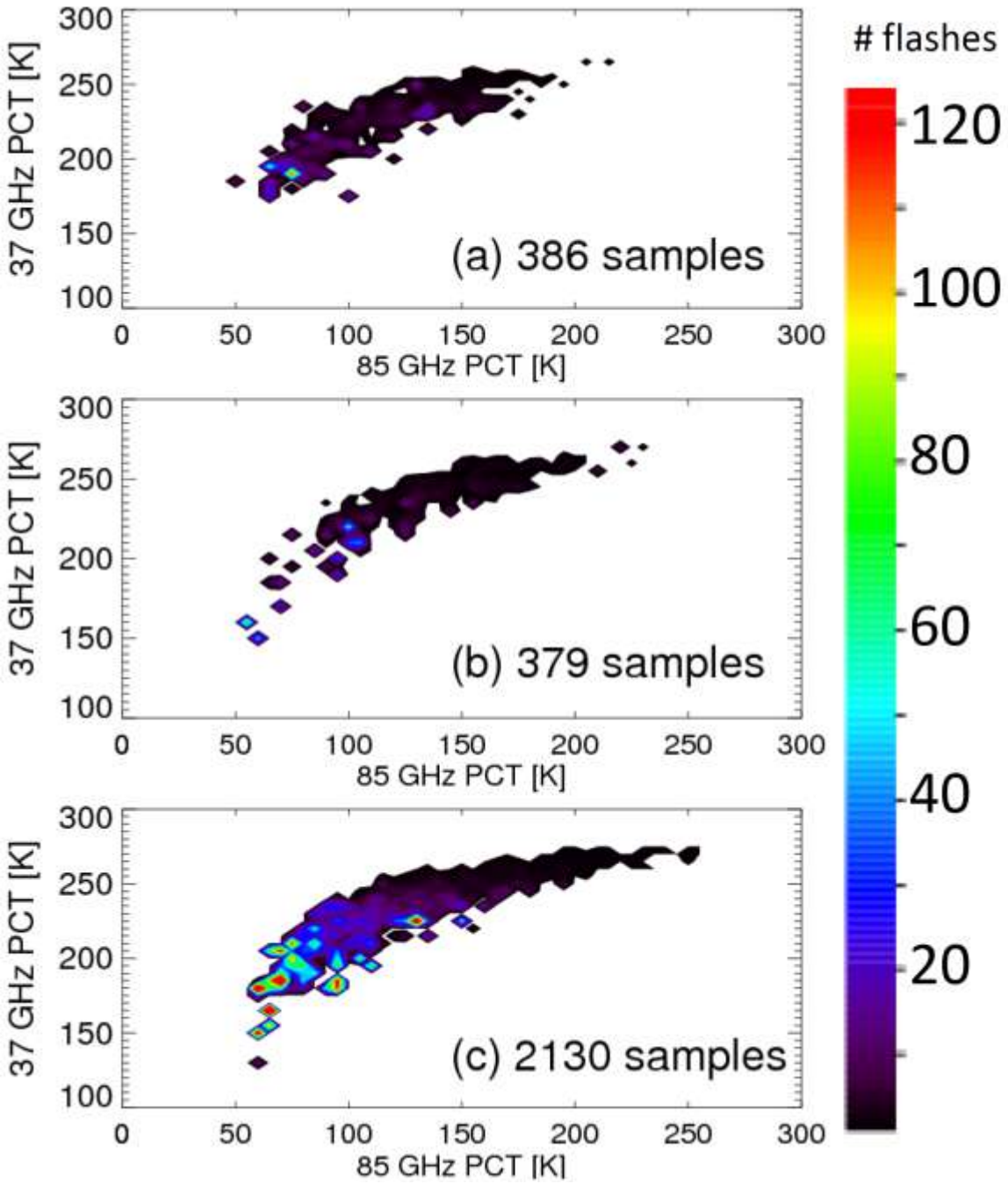

Figure 3.7. Lightning flash counts as a function of minimum 85 GHz PCT [K] and minimum 37 GHz PCT [K] (in 5 K bins) in (a) IC (b) IB and (c) OB TTPFs. The number of flashes in each PCT bin are totaled and then normalized by the number of features with lightning in that bin.

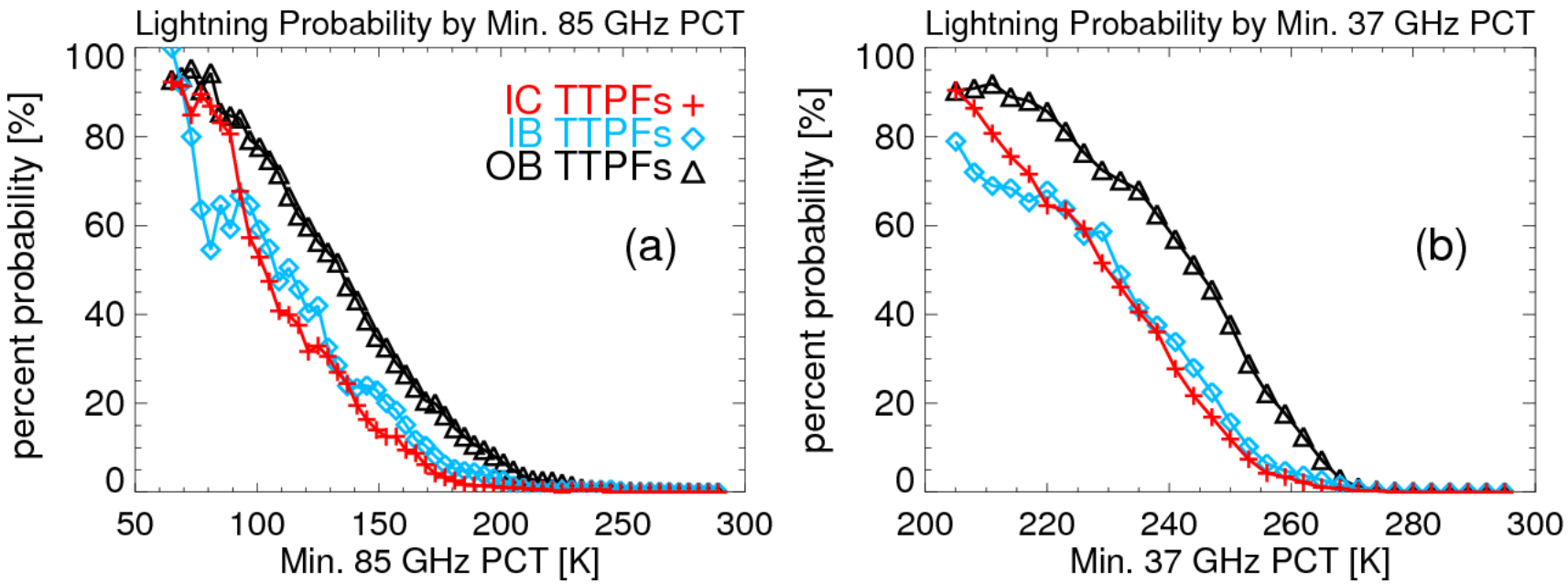

Figure 3.8. Probability of lightning occurrence within IC, IB, and OB TTPFs as a function of (a) minimum 85 GHz PCT [K] and (b) minimum 37 GHz PCT [K].

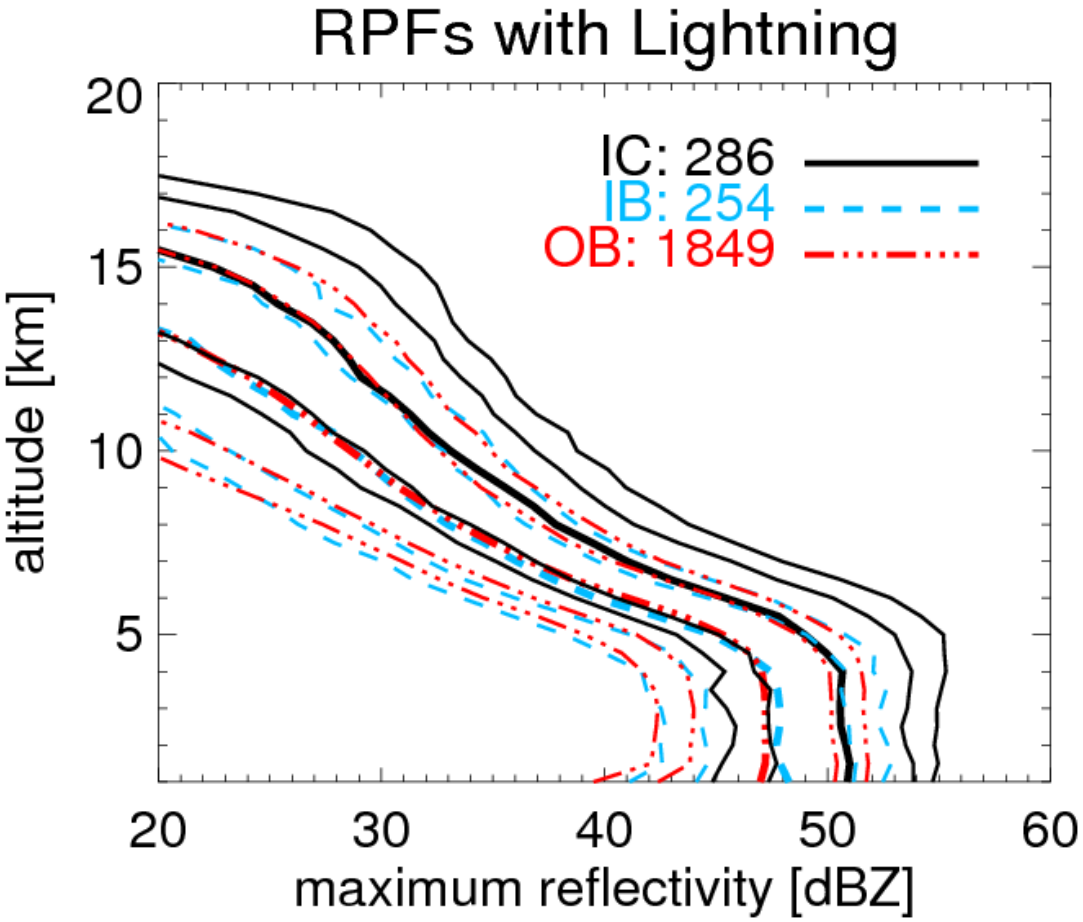

Figure 3.9. Tenth, 30th, 50th, 80th, and 90th percentiles of vertical profile of maximum radar reflectivity for IC, IB, and OB RPFs with lightning.

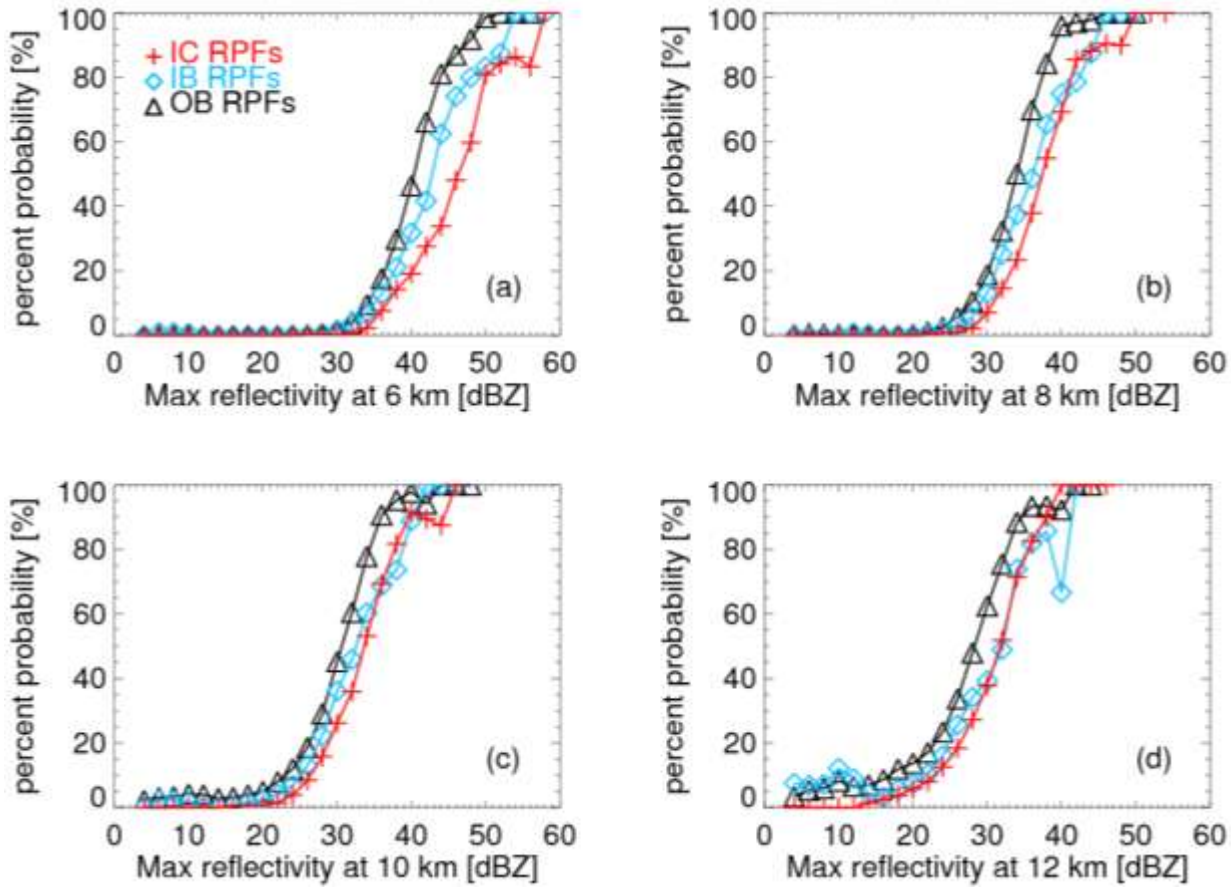

Figure 3.10. Probability of lightning occurrence within IC, IB, and OB TTPFs as a function of maximum radar reflectivity [dBZ] at (a) 6km (b) 8km (c) 10km and (d) 12km.

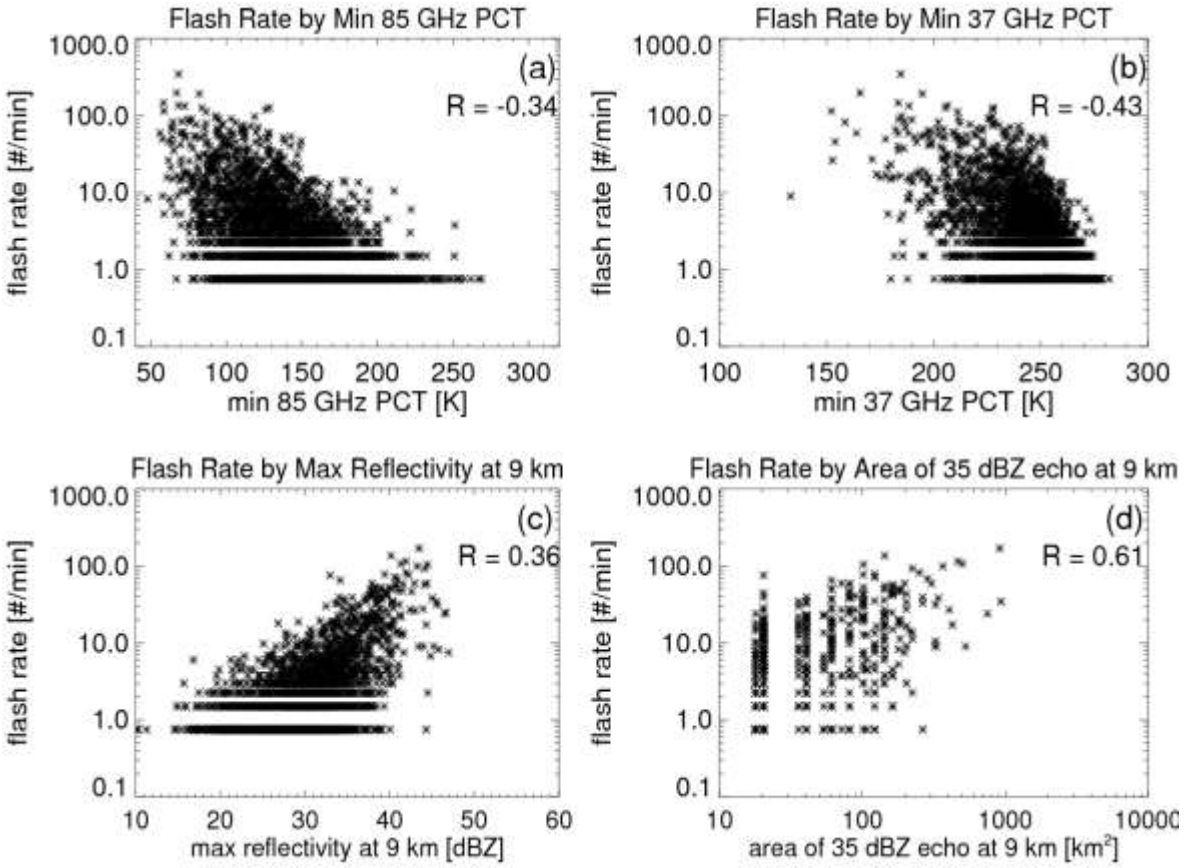

Figure 3.11. Scatterplot of flash rate versus (a) minimum 85 GHz PCT [K] (b) minimum 37 GHz PCT [K] (c) maximum radar reflectivity at 9 km [dBZ] and (d) area of 35 dBZ echo at 9 km [km^2].

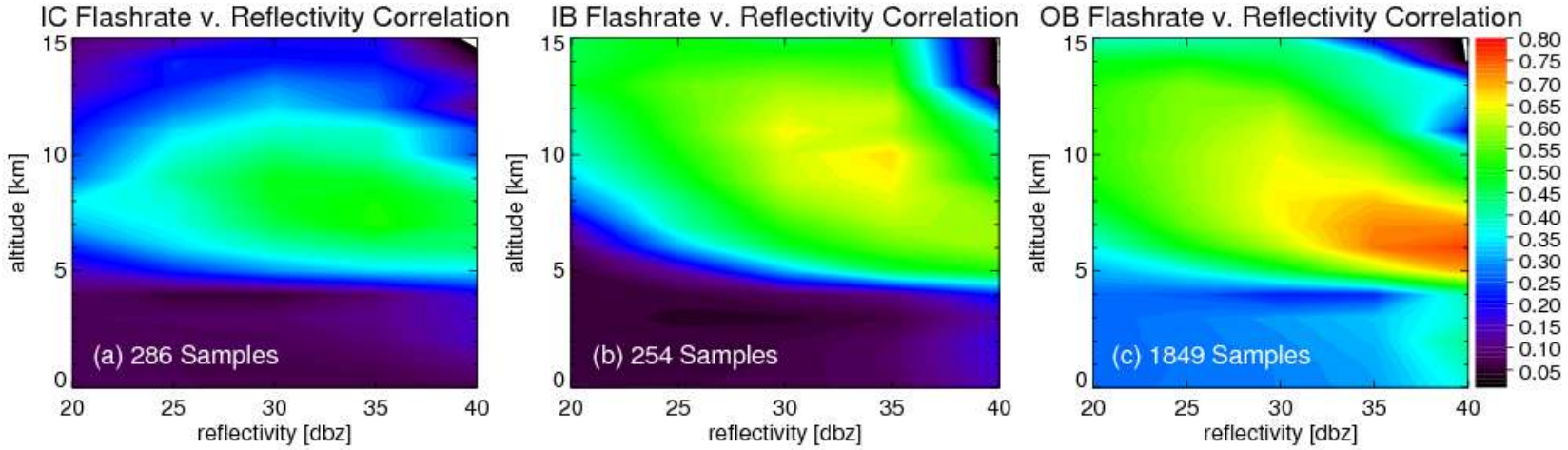

Figure 3.12. Linear correlation coefficients between lightning flash rate [fl min^{-1}] and area of radar reflectivity at certain values showed on the x-axis [km^2] in all (a) IC TTPFs (B) IB TTPFs and (c) OB TTPFs with lightning at different altitudes.

Table 3.1. Number and percentage of TTPFs that contain a lightning flash in the IC, IB, and OB TC regions.

TC Region	ALL TTPFs	TTPFs W/ Lightning	%
IC	4077	386	9.5
IB	8094	379	4.7
OB	50281	2130	4.2

Table 3.2. Lightning flash counts and ratios of various aspects of sample size to flash count in IC, IB, and OB TTPFs.

TTPFs	Number of TCPFs	Number of Flashes	2A12 Rain Area per flash	2A12 Vol. Rain per flash	85 GHz PCT Area < 225 K per flash	85 GHz PCT Area < 250 K per flash	11μm Tb Area < 210 K per flash	11μm Tb Area < 235 K per flash
	[#]	[#]	[km^2]	[$mmh^{-1}km^2$]	[km^2]	[km^2]	[km^2]	[km^2]
IC	4077	2317	23800	124200	2800	7600	21900	33500
IB	8094	1786	96200	360600	5700	24600	47300	90300
OB	50281	21619	46800	136900	2000	9400	9700	28300

Table 3.3. Same as Table 3.1, but for RPFs.

TC Region	ALL RPFs	RPFs W/ Lightning	%
IC	8250	286	3.5
IB	23742	254	1.1
OB	162881	1849	1.1

CHAPTER 4

CONVECTIVE AND RAINFALL PROPERTIES FOR INTENSITY CATEGORIES

Intensity categories are based on the Saffir-Simpson scale (Table 4.1) and include tropical depressions (TD), tropical storms (TS), category 1-2 hurricanes (CAT12), and category 3-5 hurricanes (CAT35, also called *major hurricanes*). Other countries use terms such as typhoon or tropical cyclone, but for consistency all storms will be referenced by National Hurricane Center standards. TC intensity is a measure of the 1-min average wind speed, with the radius of maximum wind located near the inner edge of the eyewall for well developed systems. All TCPFs for intensity analysis are of the IC region.

In Croxford and Barnes (2002), the IC strength is defined as the mean tangential wind from 65 – 140 km from the circulation center, and was found to be linearly related to TC intensity for 18 Atlantic TCs. In this study, the IC strength is taken as the best track documented maximum sustained wind speed, which is then compared with the strength of TRMM derived convective, rainfall, and lightning characteristics.

4.1 TMI: Polarization Corrected Brightness Temperatures and 2A12 Rainfall

CDFs of minimum 37 and 85 GHz PCTs and 11μm Tb in IC features in different intensity stages are presented in Fig. 4.1. Median values of minimum 85 GHz PCT in the IC region for TD, TS, CAT12, and CAT35 are 200, 183, 178, and 166 K, respectively (Fig. 4.1a). Approximately 65% of TD IC features have minimum 85 GHz PCT less than 225 K, as do 75% of TS IC features, 90% of CAT12 IC features, and 98% of CAT35 IC features. This suggests that convective signatures are more often seen in the IC region of stronger storms.

However, at the stronger end of the convective spectrum with minimum 85 GHz PCTs below 150 K, the gap between intensity categories narrows and eventually the order switches. There are 7.0% of IC features with minimum 85 GHz PCTs < 100 K in the TS category, 3.7% in TD, 2.0% in CAT12, and only 0.8% in CAT35 categories. This implies that extremely strong convection is more often seen in TSs and TDs than in hurricanes. The subhurricane strength storms that have the coldest PCTs in the IC region may be intensifying. Median values of minimum 37 GHz PCT are 264, 261, 258, and 254 K in IC features in TD, TS, CAT12, and CAT35, respectively (Fig. 4.1b). This suggests that generally, the minimum 37 GHz PCT decreases as storm intensity increases. However, a similar flip-flop scenario, as in minimum 85 GHz PCTs (Fig. 4.1a), is also observed in minimum 37 GHz PCTs as the intensity category distributions gradually converge around 250 K and then switch below 240 K. This indicates that at the stronger end of the convective intensity spectrum, some TS and TD IC features may contain larger ice particles than hurricane IC features. An interesting attribute of feature minimum

11μm Tb distributions is the spectrum of observed values. The TD , TS, and CAT12 categories all span about 118 K, from 172-290 K and the CAT35 category spans just 57 K, from 176-233 K. Minimum 11μm Tbs are nonexistent below 170 K for any category. One hundred percent of CAT35 minimum 11μm Tbs lie between 175-233 K, as do 97% of CAT12, 87% of TS, and 79% of TD features.

CDFs of TTPF size and percentage of pixels with 85 GHz PCT less than 250, 225, and 150 K are presented in Fig. 4.2. The IC TTPF size distribution (Fig 4.2a) shows that the hurricane IC features are much larger than those in TS and TD. Median feature sizes are 11 100 km^2 in TD, 14 500 km^2 in TS, and 19 700 km^2 in both CAT12 and CAT35 categories. Percentage of 85 GHz PCT area less than 225 K and 250 K is highest for CAT35 features (Fig. 4.2b-c), followed by CAT12, TS, and TD features. This indicates that as TC intensity increases, the areal percentage of both raining pixels (85 GHz PCT < 250 K) and convective pixels (85 GHz PCT < 225 K) increases. However, the exception to that statement is that the TS IC region has the highest percentage of features with minimum 85 GHz PCT below 130 K (Fig 4.1), so it is useful to examine the percentages of IC pixels with 85 GHz PCT under 150 K (a somewhat arbitrary, but very cold threshold) in each orbit, among each intensity category (Fig. 4.2d). Similar to the minimum PCT analysis at the stronger end of the convective spectrum, the TS IC features clearly exhibit the highest percentage of pixels below 150 K, with TD features in second. Although the IC region in hurricanes has more moderate convective strength features, TSs and TDs exhibit higher percents of *extremely* cold minimum 85 GHz PCTs (e.g., < 150 K) in the IC region. These TS and TD IC features which experience near center

convective bursts, or hot towers, have been hypothesized to undergo TC intensification (Steranka et al. 1986), but not necessarily RI.

The 2A12 mean conditional rain rates (Fig. 4.3a) in IC features increases for increasing storm intensities. Stronger hurricanes have higher rain rates. Median values in TD, TS, CAT12, and CAT35 are 3.1 mm h^{-1}, 4.2 mm h^{-1}, 5.8 mm h^{-1}, and 8.1 mm h^{-1}. The 2A12 volumetric rain (Fig 4.3b) also yields increasing values for features associated with increasing storm intensities. Note that the x-axis is logarithmic in scale. There are significantly higher volumetric rain amounts in features in the IC region for major hurricanes. The median volumetric rains in TD, TS, CAT12, and CAT35 features are 33 500 $mmhr^{-1}$ km^2, 64 000 $mmhr^{-1}$ km^2, 109 000 $mmhr^{-1}$ km^2, and 152 500 $mmhr^{-1}$ km^2, respectively. The volumetric rain in TD features is a factor of 5 less than that in major hurricane features. This indicates that there is much more latent heat release in the IC features of a stronger system, due to having a much larger raining area and heavier rain rates.

4.2 PR: Vertical Profiles of Radar Reflectivity and 2A25 Rainfall

The 3-D vertical profiles of radar reflectivity provide more important information about storm structure than TMI brightness temperatures. In this section, both radar reflectivity and 2A25 rainfall from PR in each intensity category will be examined. PR sample sizes are given in Table 4.2.

The CFADs of maximum radar reflectivity in RPFs in different intensity categories are presented in Fig. 4.4. It is seen that CAT35 storms generally have the highest radar reflectivity at all vertical levels. The median maximum surface echoes for TD, TS, CAT12, and CAT35 IC features are 45, 47, 48, and 50 dBZ, respectively, while

the highest 10% of surface reflectivities are 51 dBZ, 52 dBZ, 53 dBZ and 54 dBZ, respectively. Although these measures of maximum radar reflectivity in RPFs at the surface increase with increasing TC intensity, the top 10% of reflectivities at 14 km height are 26 dBZ in TD, 29 dBZ in TS, 28 dBZ in CAT12, and 24 dBZ in CAT35. Similar to what is seen in Fig. 4.2d, the extremely strong echoes in the TS features may be from bursts of intense convection near the storm center that *could* be related to some degree of intensification.

The overlays of the median profiles in Fig. 4.5 reveal that the median maximum radar reflectivity profile in IC features gets stronger as storm intensity increases. However, in the top 10% profile this is only true below 11 km altitude. Above 11 km, TS IC features contain the strongest radar reflectivities, while the CAT35 IC features contain the weakest radar reflectivities. This is consistent with the TMI-based analysis in section 4.1.

As shown in TTPF rain data, the 2A25 RPF rain rate (Fig. 4.6a) increases as the storms' intensity increases. The CAT35 storms have the greatest amount of IC rain volume, as shown in Fig 4.6b (again note that the x-axis is in log scale), followed by CAT12, TS, and TD.

4.3 Lightning

Cecil and Zipser (1999) used the OTD data to study lightning flash counts and rates in storms of varying intensity. They found that lightning near the IC most often occurs in weak tropical storms with maximum wind speed of 34 – 45 kts (flash in 44% of observations) and strong hurricanes with maximum wind speed greater than 95 kts (flash in 37% of observations). Similar trends are seen with the present dataset (Table 4.3). In

terms of TTPF analysis, only 15% of TD TTPFs and 17% of TTPFs in weak hurricanes recorded lightning flashes. The IC TTPFs in CAT35 hurricanes produce lightning most often, twice as often as TS features, which have the second highest percentage. The CAT12 and TD categories are comparable with 7-8%.

Figure 4.7 shows the percentages of TTPFs with lightning as a function of minimum 85 and 37 GHz PCTs in different intensity categories. Lightning probabilities tell which intensity category is most likely to have a lightning flash with a given feature minimum parameter. For minimum 85 GHz PCTs above 200 K and 37 GHz PCTs above 270 K, lightning activity is little to none. The likelihood of a discharge begins to increase significantly in CAT35 IC TTPFs with minimum 85 GHz PCT below 180 K and minimum 37 GHz PCT below 260 K. All other intensity categories produce greater likelihoods, but less steep, when minimum 85 GHz PCTs fall below 165 K and minimum 37 GHz PCTs fall below 255 K. CAT35 IC features have a greater chance of generating lightning than other categories, and CAT12 IC features generally have the lowest probabilities, as a function of minimum 85 GHz PCTs, but the small sample size of features that record a flash severely discredits any details in the trends. The lightning probabilities in terms of minimum 37 GHz PCT are similar in that in general, it is easier for an intense storm to produce a lightning flash.

Abarca et al. (2010) examined 24 Atlantic TCs that came within 400 km of the coastline and showed that average flash densities near the center of circulation were smaller for hurricanes than for TDs. A ratio of convective and rainfall parameters to flash count are calculated in IC TTPFs in different intensity stages (Table 4.4). For the unit of 2A12 raining area per flash, TD, TS, and CAT35 are comparable while CAT12 is about a

factor of 3 fewer. This is similar to what is found by Cecil and Zipser (1999). For the ratio of 2A12 volumetric rain per flash, the TD features produce twice as many strikes as a CAT35 feature. The TD features produce a lightning flash with a smaller unit area of rain and a smaller unit area with brightness temperature < 250 K and < 225 K thresholds than the other intensity categories. The exception is the area of 85 GHz PCT < 150 K per flash, where on average the CAT35 features need only half the area that TDs require to record a flash. There are two ways the ratio for CAT35 features could have decreased, either by reducing the area (numerator) or increasing the flash count (denominator). By revisiting Fig. 4.2d, it is clear that CAT35 features produce the lowest feature percentage of pixels with 85 GHz PCT less than 150 K, suggesting that the numerator has been reduced.

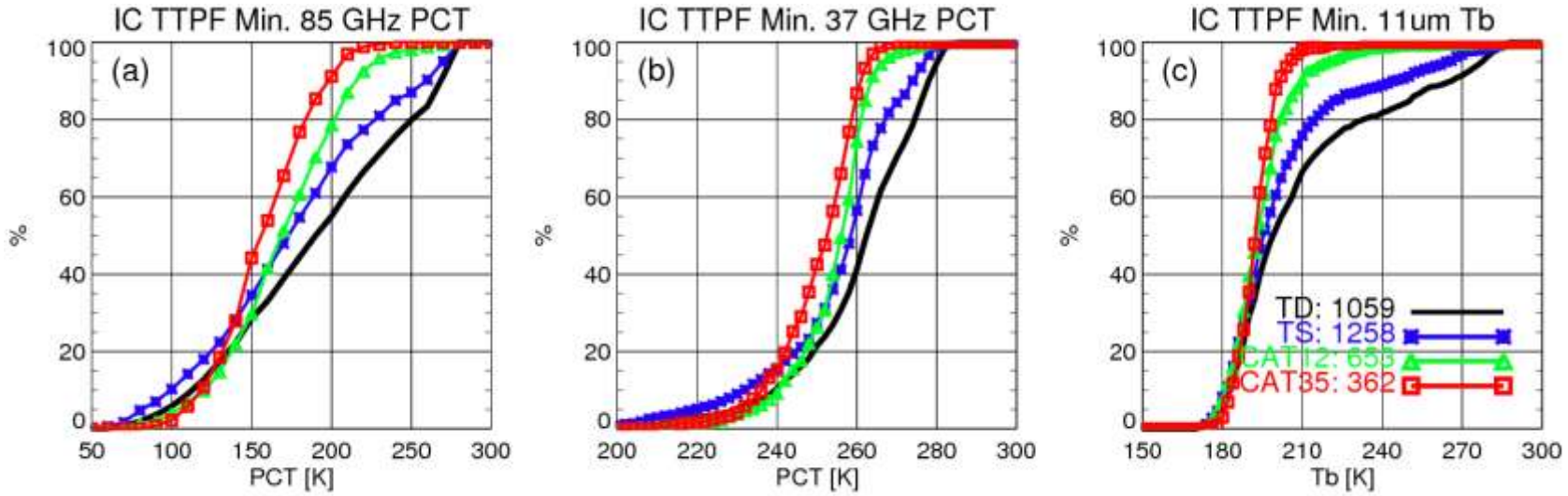

Figure 4.1 CDFs for (a) minimum 85 GHz PCT [K] (b) minimum 37 GHz PCT [K] and (c) minimum 11μm brightness temperature [K] for IC TTPFs in the TD, TS, CAT12, and CAT35 intensity categories.

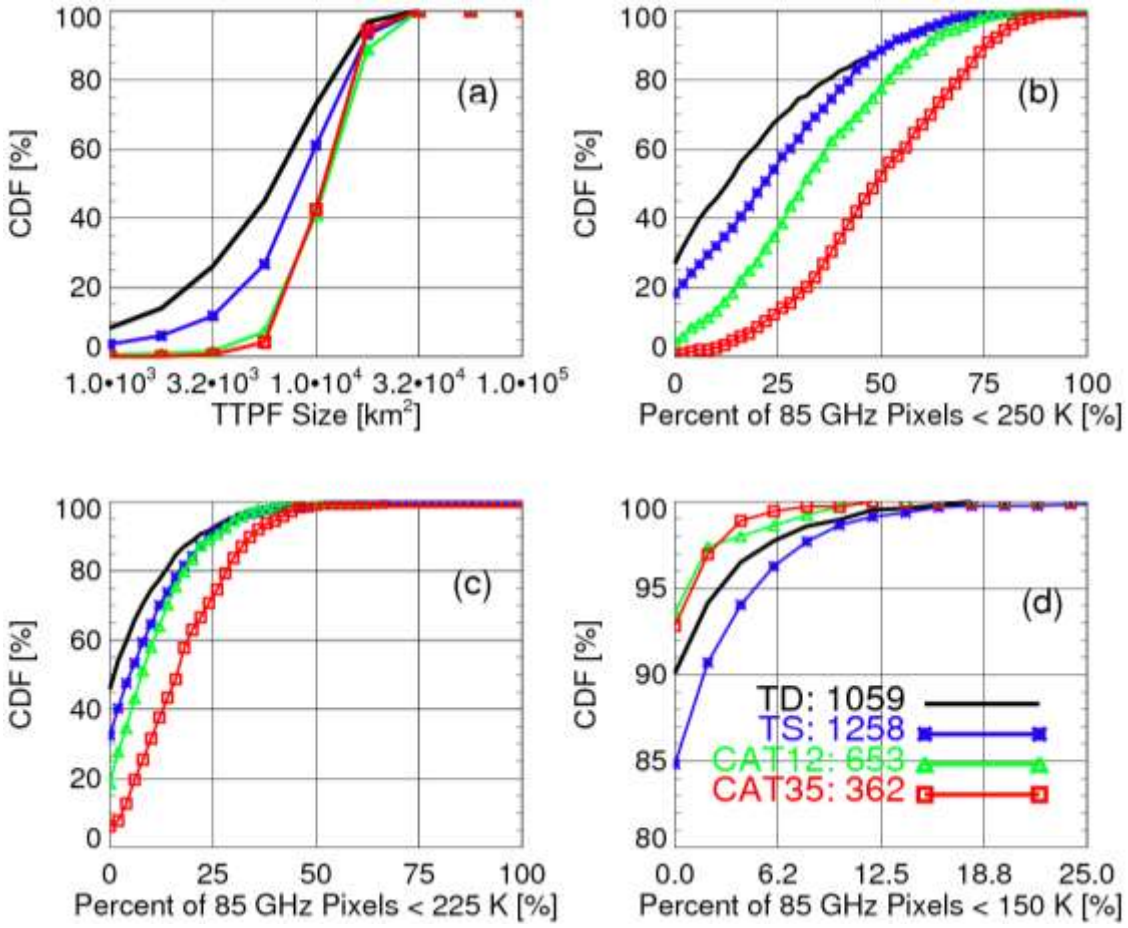

Figure 4.2. CDFs for (a) TTPF size [km^2] (b) percent of 85 GHz PCT pixels less than 250 K [%] (c) percent of 85 GHz PCT pixels less than 225 K [%] and (d) percent of 85 GHz PCT pixels less than 150 K [%] for IC TTPFs in the TD, TS, CAT12, and CAT35 intensity categories.

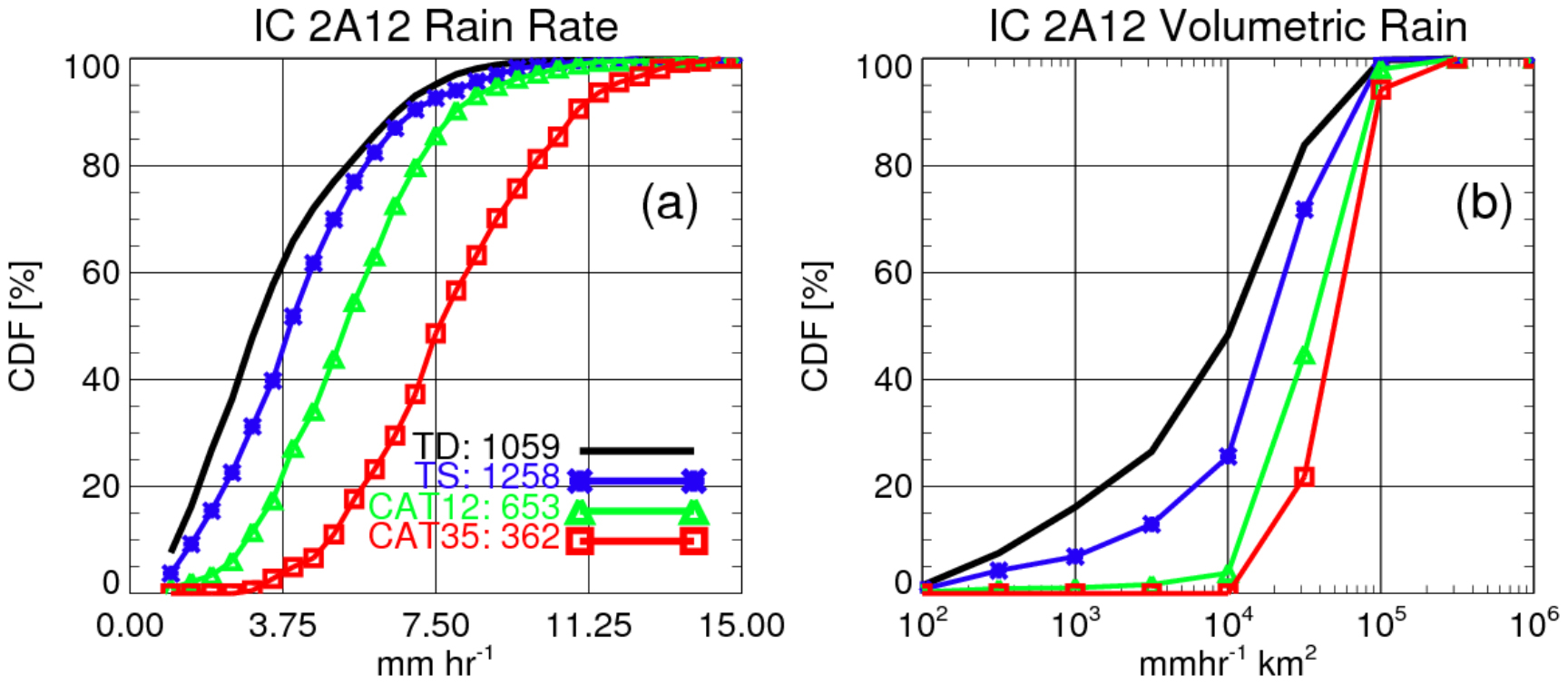

Figure 4.3. CDFs of TMI 2A12 (a) rain rate [mm hr^{-1}] and (b) volumetric rain [$mmhr^{-1}$ km^2] for IC TTPFs in the TD, TS, CAT12, and CAT35 intensity categories.

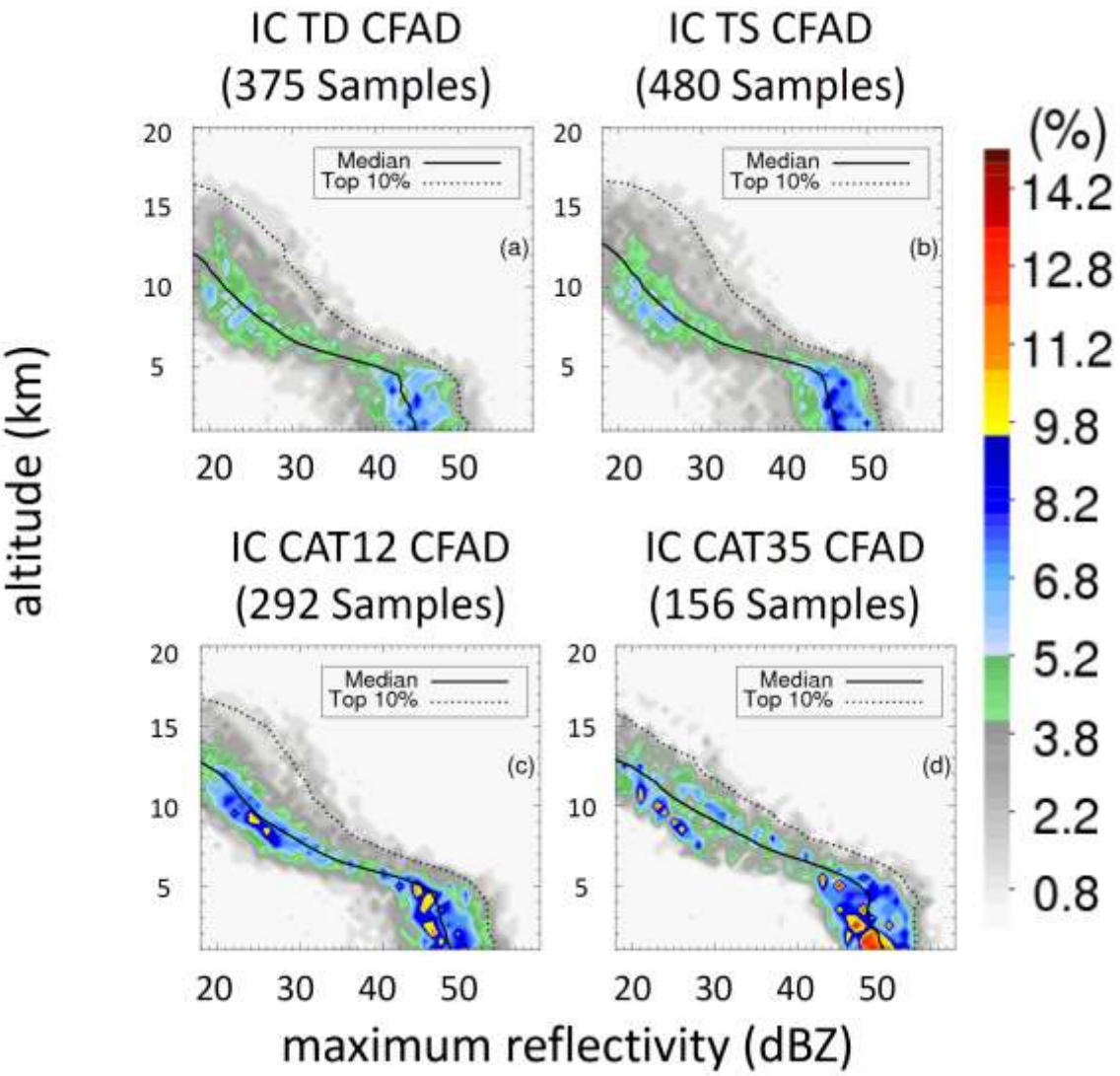

Figure 4.4. CFADs of IC (a) TD RPFs (b) TS RPFs (c) CAT12 RPFs and (d) CAT35 RPFs. The median maximum reflectivity profile is indicated by the solid black line and the top 10 % of maximum reflectivity profile is indicated by the dashed line.

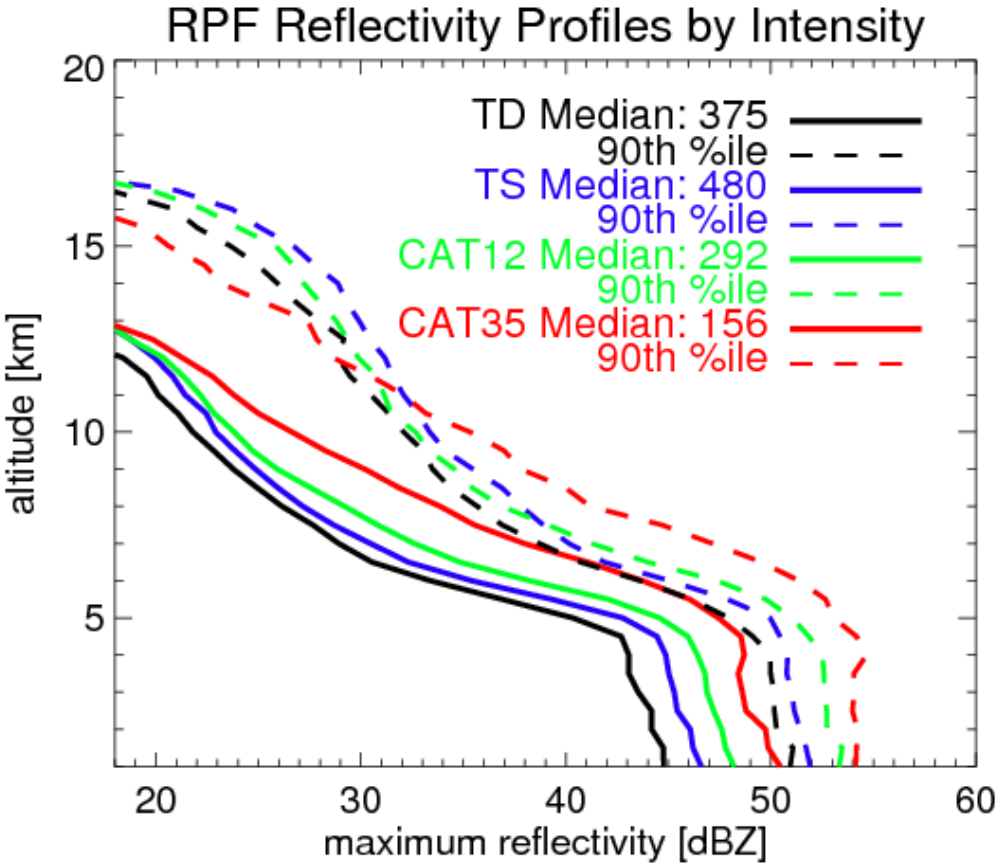

Figure 4.5. Median (solid lines) and 90th percentile (dashed) of vertical profile of maximum radar reflectivity IC RPFs in TD, TS, CAT12, and CAT35 intensity categories.

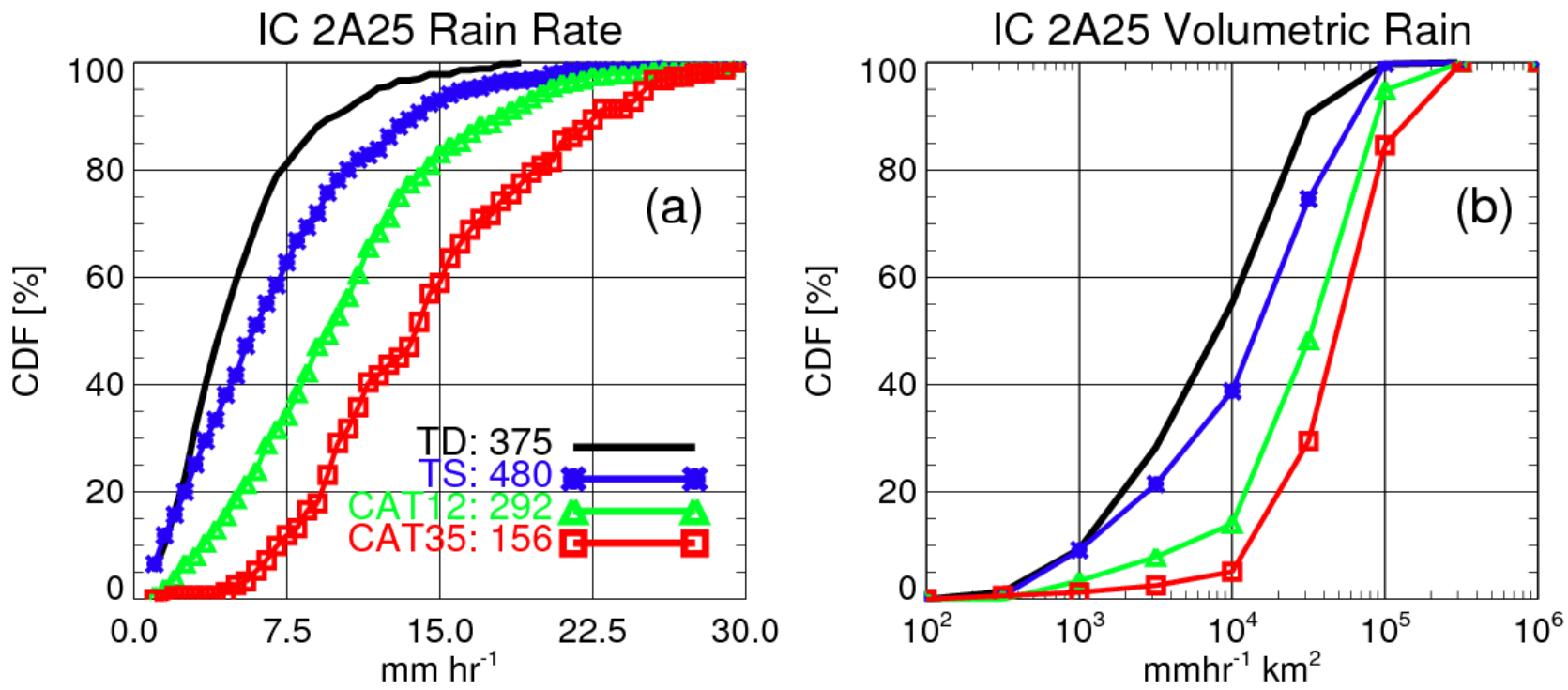

Figure 4.6. CDFs of PR 2A25 (a) rain rate [mm hr^{-1}] and (b) volumetric rain [$mmhr^{-1}$ km^2] in IC TTPFs in the TD, TS, CAT12, and CAT35 intensity categories.

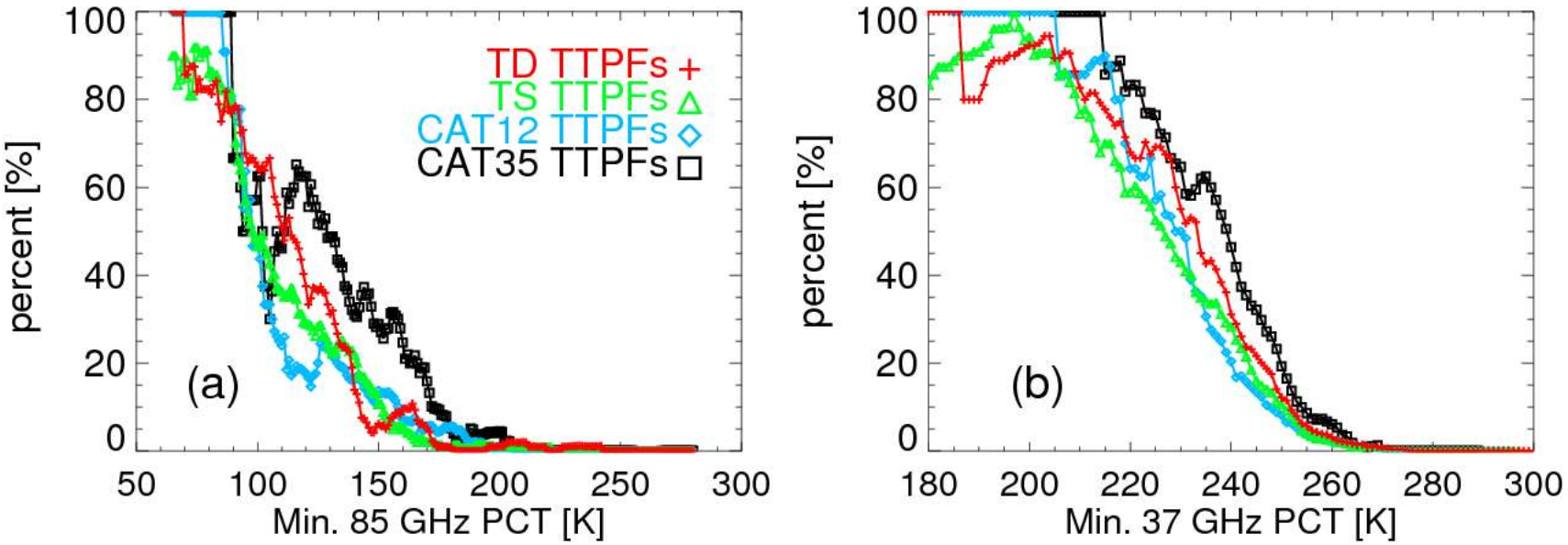

Figure 4.7. Probability of lightning occurrence within TD, TS, CAT12 and CAT35 IC TTPFs as a function of (a) minimum 85 GHz PCT [K] and (b) minimum 37 GHz PCT [K].

Table 4.1. Definition of TD, TS, CAT12, and CAT35 intensity categories and respective IC TTPF population sizes.

TC Intensity	**Maximum Wind Speed Range [kts]**	**IC TTPFs**
TD	$v_{max} < 34$	1059
TS	$64 > v_{max} \geq 34$	1258
CAT12	$64 \leq v_{max} \leq 95$	653
CAT35	$v_{max} > 95$	362
Total	-	3332

Table 4.2. Same as Table 4.1, but for RPFs.

TC Intensity	**Maximum Wind Speed Range [kts]**	**IC RPFs**
TD	$v_{max} < 34$	375
TS	$64 > v_{max} \geq 34$	480
CAT12	$64 \leq v_{max} \leq 95$	292
CAT35	$v_{max} > 95$	156
Total	-	1303

Table 4.3. Number and percentage of IC TTPFs that contain a lightning flash in the TD, TS, CAT12, and CAT35 intensity categories.

Int. Category	ALL IC TTPFs	IC TTPFs W/ Lightning	%
TD	1513	104	6.9
TS	1520	155	10.2
CAT12	680	53	7.8
CAT35	364	74	20.3

Table 4.4. Lightning flash counts and ratios of various aspects of sample size to flash count in TD, TS, CAT12, and CAT35 TTPFs.

TTPFs	Number of TCPFs w flash	Number of Flashes	2A12 Rain Area per flash	2A12 Vol. Rain per flash	85 GHz PCT Area < 250 K per flash	85 GHz PCT Area < 225 K per flash	85 GHz PCT Area < 150 K per flash	11μm Tb Area < 235 K per flash	11μm Tb Area < 210 K per flash
	[#]	[#]	[km^2]	[$mmh^{-1}km^2$]	[km^2]	[km^2]	[km^2]	[km^2]	[km^2]
TD	1513	732	18600	73000	4700	1700	125	23000	13400
TS	1520	914	22500	102900	6200	2400	205	30000	19500
CAT12	680	256	53200	311000	18700	6300	200	84400	55300
CAT35	364	415	17700	146400	9000	3400	65	28500	21500

CHAPTER 5

CONVECTIVE AND RAINFALL PROPERTIES FOR INTENSITY CHANGE STAGES

Changes in cyclone intensity depend not only on large-scale environmental conditions (Kaplan and DeMaria 2003, Hendricks et al. 2010), but also on convective and mesoscale processes. This chapter examines passive microwave, IR, radar, and lightning properties in the TC region in relation to 24-h TC intensity evolution. To exclude land interference and baroclinic processes affecting mid-latitude storms, TCs that are making landfall within 24 h of the overpasses and TCs that are classified as having undergone extratropical transition are removed from the sample. Category 5 strength TCs are also removed because they are certainly either at or near their maximum potential intensity (MPI) and have almost no potential to intensify. For this study, there is no way to remove the TDs, TSs, and category 1-4 storms that have reached their MPI because it cannot be calculated for every overpass due to lack of information. Twenty-four-hour intensity change categories (Table 5.1) include weakening (W), neutral (N), slowly intensifying (SI), and rapidly intensifying (RI: Kaplan and DeMaria 2003). Neutral change has a built-in 9 kt uncertainty to account for errors in wind speed estimation.

5.1 TMI: Polarization Corrected Brightness Temperatures and 2A12 Rainfall

Fig. 5.1 presents the CDFs of minimum 85 and 37 GHz PCT and 11 μm Tb in IC TTPFs in different TC intensity change categories. From Fig. 5.1a, 100% of IC TTPFs in the RI category have minimum 85 GHz PCT less than 256 K, while 5 (10, 15)% of IC TTPFs in the SI (W, N) category have minimum 85 GHz PCT greater than or equal to 256 K. This shows that RI storms do not contain warm features in the IC region (warmer than 256 K in minimum 85 GHz PCT) after using the PF size >1000 km^2 threshold, but all other categories do. The minimum 85 GHz PCT < 256 K in the IC region is a necessary condition for RI. Between 150-250 K of the minimum 85 GHz PCT distributions, RI storms have the coldest IC features at any given percentile (between 50^{th} and 100^{th}), followed by SI, W, and N, although the CDFs of the latter two categories intersect each other in this range. For the coldest portion of the distribution, below 130 K, no distinct differences are seen among different intensity change categories.

Fig. 5.1b shows that the trend in the warmer portions of the 37 GHz PCT distributions (≥ 250 K) is similar to the trend seen in the 85 GHz PCT distributions. From Fig. 5.2b, 100% of IC TTPFs in the RI category have minimum 37 GHz PCT ≤ 277 K, while 4 (5, 12)% of IC TTPFs in the SI (W, N) category have minimum 37 GHz PCT greater than or equal to 277 K. Between 250-275 K of the minimum 37 GHz PCT distributions, RI storms have the coldest IC features at any given percentile (between 30^{th} and 100^{th}), followed by the IC features in the SI, W, and N categories. However, in the coldest portions (< 250 K) of the 37 GHz PCT distributions, the trends are reversed such that RI IC features no longer have the highest percentage of their respective sample that

meets this threshold, but instead are very slightly less than those in other intensity change categories. From Fig. 5.1c, RI features always produce the coldest minimum 11μm brightness temperature in the IC region, followed by the features in the SI, W, and N categories.

General findings from feature minimum PCT and Tb analysis are that RI features in the IC region more frequently produce colder cloud tops and more ice scattering than those in other intensity change categories, although RI features do not necessarily contain the coldest or most intensive convection. Steranka et al. (1986) found high correlations between prolonged surges of deep convective bursts and 24-h TC intensification of 5 m s^{-1} or greater. While their finding can neither be confirmed nor denied since this study uses snapshots of TCs, it is seen here that the presence of very deep convection is not unique to intensifying storms. It is also interesting to note from Fig. 5.1a-c that features associated with W storms generally produce more ice scattering and colder cloud tops than those associated with N storms, probably because the W sample contains a higher number of strong TCs than the N sample.

CDFs of IC TTPF size and percentage of pixels with 85 GHz PCT < 250, 225, and 150 K in different TC intensity change categories are presented in Fig. 5.2a-d. The IC TTPF size distribution (Fig. 5.2a) shows that IC features associated with RI storms are the largest (indicating 2A12 raining area), followed by those associated with W, SI, and N storms. Median TTPF sizes are 20 300, 17 000, 13 200, and 17 700 km^2 in RI, SI, N, and W features, respectively. RI storms tend to have larger raining features in the IC region than those in other intensity change categories.

Percentages of IC pixels with minimum 85 GHz PCT under 250 K (Fig. 5.2b) and under 225 K (Fig. 5.2c) clearly show that RI IC features have the highest percentage of area containing moderate rainfall and convection. Median values of percentages of IC pixels with minimum 85 GHz PCT below 250 K are roughly 39% in RI, 32% in SI, 21% in N, and 26% in W, while for minimum 85 GHz PCT below 225 K, the median values are roughly 14% in RI, 10% in SI, 6% in N, and 7% in W. Percentages of pixels with minimum 85 GHz PCT below 150 K (Fig. 5.2d) show a different order. At the 98th percentile, IC features associated with SI, N and W storms have near 8% of IC pixels with this extremely low value of minimum 85 GHz PCT, but RI features record only 2%. This is consistent with the findings by Cecil and Zipser (1999) and Kerns and Zipser (2009), both of which show that intensifying TCs have larger spatial coverage of at least moderate IC rainfall and relatively strong ice scattering signature, but do not necessarily have the most intense rainfall and convection.

Fig. 5.3 shows CDFs of TMI 2A12 rain rate and volumetric rain in IC features in different intensity change categories. Between the 0 and 65th percentile, RI features have higher rain rates in the IC region than those in other categories (Fig. 5.3a). However, the difference is not very large. For example, at median, the difference between RI and N (which exhibits the lowest rain rates in these percentiles) is only about 1.8 mm h^{-1}. As the percentile increases from 65th, the difference among categories decreases rapidly until eliminated at the 95th percentile. In contrast, CDFs of volumetric rain (Fig. 5.3b) show that RI features always have the largest volumetric rain in the IC region, followed by SI, W, and N features. The difference is quite large. For example, at median, RI features have roughly 109 000 mmhr^{-1} km^2 volumetric rain in the IC region, but SI and W features

have in the vicinity of 85 000 $mmhr^{-1}$ km^2, and N features have only roughly 56 000 $mmhr^{-1}$ km^2. Since volumetric rain is simply the product of rain rate and raining area (feature size in this case), this result suggests that a slightly higher rain rate and much larger raining area in the IC region is characteristic of storms undergoing RI.

5.2 PR: Vertical Profiles of Radar Reflectivity and 2A25 Rainfall

Because the PR swath is much narrower than the TMI swath, the IC RPF population (Table 5.2) is only about one third of the IC TTPF population (Table 5.1). To keep the sample size not extremely small, if a PR orbit captures 80% or more of the IC region of a storm, all IC RPFs with size larger than 1000 km^2 observed in this PR swath are included in the sample. Note that for TTPFs, the sample is included only if the TMI orbit captures 100% of the IC region.

Fig. 5.4 shows the CFADs of maximum radar reflectivity in IC RPFs in different intensity change categories. While the distributions are rather similar among Fig. 5.4a-d, there are some subtle differences: 1) Radar reflectivities in IC RPFs associated with RI storms are centered densely around the median profile at all levels, but reflectivities are spread over a greater range for other categories and 2) IC RPFs associated with RI storms have a higher maximum 20 dBZ echo top than other intensity change categories, as seen in both median and top 10% profiles.

To further compare the radar reflectivity profiles among different intensity change categories, Fig. 5.5 overlays the median and 90^{th} percentile profiles of maximum radar reflectivity. Two things are worth mentioning: 1) Median maximum radar reflectivity profiles show little difference except at upper levels (between 10-15 km), where RI IC RPFs record stronger echoes than IC RPFs in other intensity change categories by an

average of 2-3 dBZ. The storm height for RI IC RPFs is slightly higher than other categories. This says that, overall, IC features in RI storms are deeper than those in other intensity change categories. 2) At lower levels (below 5 km), RI features have the same median maximum radar profile as the W features, while the SI features have a similar profile as the N features. The difference between the median maximum profiles of RI/W and SI/N is about 2 dBZ, with near surface values of 48.5 and 46.5 dBZ, respectively.

Fig. 5.6 shows the CDFs of PR 2A25 rain rate and volumetric rain in IC RPFs in different intensity change categories. Different from 2A12 rain rate CDFs (Fig. 5.3a), the 2A25 rain rate distribution shows that features associated with W storms generally produce the highest rain rates in the IC region. At median, the RI IC RPF rain rate is lower than that of W, but higher than that of SI and N. However, at the 70^{th} percentile and above, e.g., the top 30%, the RI IC RPFs produce the lowest rates. The top 10% of rain rates range between 12.25 – 19 in RI, 15 – 25 in SI, 15 – 28 in N, and 18 – 29 mm h^{-1} in W features. Both the algorithm biases and footprint difference between PR and TMI contribute to the discrepancies between Fig. 5.6a and Fig. 5.3a. It is very likely that the IC features in RI storms have moderate rain rates over a large area, while the IC features in W storms have high rain rates over a small area. With the coarse resolution and beam filling problem of the TMI, it is possible that the isolated features seen in W storms by the high resolution of the PR are merged together, and therefore show lower conditional mean rain rates in the TMI observation. Therefore, 2A12 rain rates in IC TTPFs in the W category appear nearly equal to or slightly lower than those in the RI category. This suggests that RI storms have broad areas of moderate rain embedded with moderate

convection (likely somewhat symmetric) in the IC region, whereas weakening storms contain isolated features that are smaller and have heavier rain rates.

Similar to their TMI 2A12 counterparts (Fig. 5.3b), CDFs of PR 2A25 IC RPF volumetric rain (Fig. 5.6b) show that RI features have the highest volumetric rain in the IC region, followed by W, SI, and N features. Median volumetric rain values in RPFs in RI, W, SI, and N features are 93 000, 86 000, 59 000, and 48 000 $mmhr^{-1}$ km^2, respectively. In the same order, the minimum volumetric rains are 1 900, 940, 480, and 480 $mmhr^{-1}$ km^2. In the same order, the percents of each respective feature population that produce less than 10 000 $mmhr^{-1}$ km^2 are 8.6%, 14.7%, 16.6%, and 19.5%. This further confirms that a larger volumetric rain in PFs in the IC region is more frequently observed in storms undergoing RI.

5.3 Lightning

Electrification as a precursor to TC intensity change has been heavily debated in recent years. Price et al. (2009) analyzed the lifetime of 56 TCs in 6-h intervals and found that minimum pressures and peak winds are measured about 1 d after increases in lightning activity are detected. Leary and Ritchie (2009) separated 98 North Pacific tropical cloud clusters into developers and nondevelopers to determine if there were differences in 6-h flash counts. It was found that average developing clusters had approximately 150 more flashes than average nondeveloping clusters. Squires and Businger (2008) detailed the processes surrounding 3 of their best observed lightning outbreaks in either Katrina (2005) or Rita (2005). The first outbreak occurred at the onset of RI, with 35 m s^{-1} maximum wind speed increase in 24 h. The second outbreak

occurred at the end of an RI period and the third, weaker outbreak occurred in the middle of an eyewall replacement cycle.

In this section, TRMM LIS observed flashes in the IC region are examined in relation to TC 24-h intensity changes. This examination is still conducted in terms of IC PFs, not TC orbits. Table 5.3 shows the number and percentage of IC TTPFs with LIS detected lightning for different intensity change categories. From Table 5.3, IC TTPFs in the W category have the highest fraction with lightning (10.5 %) and IC TTPFs in the RI category have the lowest fraction (6.7 %). Cecil and Zipser (1999) studied 2 y of TCs of at least TS intensity using lightning data from the OTD. They showed that 57% of the observations of storms that intensify moderately (24-h intensity change between 5-15 kts) have lightning in the eyewall region. This percentage is 44% in storms that weaken moderately, 25% in storms that intensify 15 kts or more during 24 h, and 8% in storms that weaken 15 kts or more over 24 h. The sample size in this study is much more robust than in Cecil and Zipser (1999). Though methodologies are different, both studies show a decreased likelihood of RI following IC lightning.

Lightning probability is assessed as a function of minimum 85 GHz and 37 GHz PCTs in TTPFs in different intensity change categories (Fig. 5.7a-b). The greatest differences are found between 100-150 K in minimum 85 GHz PCT and 230–240 K in minimum 37 GHz PCT. In both instances, TTPFs in the W category appear to have a greater likelihood of producing lightning in the IC region for a given PCT value, followed by those in N, SI, and RI categories. The RI probability curve, in general, appears jumpy and there are far too few instances of samples with both lightning and minimum PCTs below 90 K (85 GHz) and 220 K (37 GHz) to be conclusive. Because

there are only 13 RI TTPF samples with lightning, Fig. 5.7c-d combines the features from both the RI and SI categories to create three curves that represent W, N, and *intensifying*. In the ranges of minimum 85 GHz PCT between 100-160 K and minimum 37 GHz PCT between 215-255 K, W features have a higher lightning likelihood in the IC region than those associated with N and intensifying storms. However, with such small populations, absolutely no conclusions can be stated with confidence until more data become available.

Table 5.4 examines the averages of TTPF convective and rainfall area normalized by the respective TTPF flash counts. This is essentially finding the lightning densities for various criteria within the features, and is completed for features in RI, SI, N, and W categories. The greatest lightning densities, in terms of raining area, volumetric rain, and areas of convection (e.g., 85 GHz PCT area < 250 K, 11μm Tb area < 235 or 210 K), are observed in the N category (indicating small intensity changes), followed by W, SI, and RI categories. The N and W IC features produce 1.5-3 times more lightning than RI features, as seen by the ratio 2A12 raining area and volumetric rain per flash, area of 85 GHz PCT below 250 and 225 K per flash, and area of 11 μm Tb below 235 and 210 K per flash. RI features have the lowest flash density overall, and only surpass the SI features for area of 85 GHz PCT below 150 K per flash.

5.4 Storm Analysis

Analyses prior to this section are all feature-based. Since multiple features may exist in a TC IC region, analysis based on storm IC *totals* may provide valuable insight. This is not to say that previous analyses are invalid, because nearly 99% of IC satellite overpasses include only one TTPF satisfying the 1000 km^2 size threshold (Tables 5.1,

5.5). Therefore, previous analyses represent the distributions of the largest feature in the IC region for each TRMM observation. The analysis to be presented in this section represents the distributions of the IC total properties for different intensity change categories with all PFs in the IC region included, not only large PFs with area >1000 km^2.

There are 181 storms that underwent RI in which the TMI swath observed 100% of the IC region, and 64 storms that underwent RI in which the PR swath observed 80% of the IC region. Fig. 5.8 shows the number of storms that underwent RI in different intensity categories (Fig. 5.8a) and in different ocean basins (Fig. 5.8b). Storms in TS stage have the highest number of RI events, while storms in CAT35 stage have the lowest number of RI events. The Northwest Pacific (NWP) basin has the highest raw number of RI events, and the North Indian Ocean (NIO) basin the lowest.

Table 5.5 shows total or average lightning and rainfall and convective proxies in the IC region in different intensity change stages, derived from TMI swath observations. For the lightning parameters, like in the feature-based analysis (Tables 5.3-4), lightning occurs more often in the IC region of W and N storms than SI and RI storms. There are 11.6% (11.5%, 10.8%, 7.2%) of TMI observations in the IC region of W (N, SI, RI) storms that have lightning. The average IC 2A12 raining area, rain rate, and volumetric rain are all highest for RI storms, followed by W, SI, and N storms. The average percentages of IC pixels with 85 GHz PCT under 250 and 225 K in RI storms are about 50% higher than those in other categories, which is related to the fact that the RI storms have the largest raining areas. The average percentage of IC pixels with 85 GHz PCT under 200 K in RI storms is the same as that in SI storms, followed by those in N and W storms.

Fig. 5.9 presents box and whisker plots of minimum 85 and 37 GHz PCT in storm ICs in different intensity change categories. Median minimum 85 GHz PCTs in W, N, SI, and RI storms are 191, 183, 171, and 163 K (Fig 5.9a), showing that RI storms are nearly 30 degrees colder than W storms at median. This is also true at the 75th percentile. However, at the 25th percentile, the minimum 85 GHz PCTs in RI storms are comparable to those in W, N, and SI storms. The whole distribution of RI category is much narrower than other categories. Minimum 37 GHz PCT distributions (Fig. 5.9b) exhibit similar patterns as the minimum 85 GHz PCT distributions.

The 25th percentile, median, and 75th percentile of 2A12 raining area in the IC region in RI storms are the highest, followed by W, SI, and N storms. The median raining areas for W, N, SI, and RI are 17 800, 13 600, 17 200, and 20 400 km^2, respectively.

The distributions of percentages of pixels in the storm IC with 85 GHz PCT below 250, 225, and 200 K (Fig. 5.11) show the same trend. The 25th percentile, median, and 75th percentile of these percentages in RI storms are the highest, followed by SI, W, and N storms. The median percentages below 250 K in W, N, SI, and RI are 27%, 24%, 33%, and 40%, respectively (Fig. 5.11a). An even larger relative difference is seen for the percentage of pixels with 85 GHz PCT below 225K (Fig. 5.11b). Respective medians are 8%, 6%, 11%, and 15%, showing that RI ICs have 0.5-2.5 times higher percentage of convective pixels than other categories. The median percentages of pixels with 85 GHz PCT below 200 K for W, N, SI, and RI are 1%, 2%, 4%, and 5%, respectively (Fig. 5.11c).

The distributions of total IC 2A12 volumetric rain and conditional mean rain rate (Fig. 5.12a-b) are very similar to those from feature-based analysis (Fig. 5.3a-b). The 25th

percentile and median volumetric rains and rain rates in RI storms are the highest, followed by W, SI, and N storms. This is also true for the 75th percentile of volumetric rain. However, the 75th percentile of rain rate is the same for both RI and W storms, followed by SI and N storms.

Table 5.6 shows total or average lightning and rainfall and convective proxies in the IC region in different intensity change stages, derived from PR swath observations. For the lightning parameters, similar to the TMI-based analysis (Table 5.5), lightning occurs less often in the IC region of RI storms than in the IC region of W, N, and SI storms. There are 6.3% (9.4%, 10.5%, 11.4%) of RI (W, N, SI) ICs observed by the PR that have lightning. Unlike TMI-based analysis, SI events produce lightning most often rather than W events. Both the difference in sample size and swath width between PR and TMI contribute to this difference. The average 2A25 IC raining area is the highest for RI storms, followed by SI, W, and N storms. However, the average 2A25 IC rain rate is highest in W storms, with RI storms ranking second, and vice versa for average IC 2A25 volumetric rain. The average maximum heights of 20, 30, and 40 dBZ echoes in the storm IC are highest in RI storms, followed by SI, W, and N storms, in that order.

Fig. 5.13 presents the distributions of total IC PR 2A25 raining area in different intensity change categories. This parameter depends on how broad an area of precipitation exists in the IC, and how far out radially the IC boundaries are defined. The 25th percentile, median, and 75th percentile of the total IC 2A25 raining area are all the highest for RI storms, followed by SI, W, and N storms. Median values for RI, SI, W, and N categories are 12 200, 9 500, 8 100, and 7 000 km^2, respectively, with RI median value greater than the other intensity change categories by 22-43%. The lower whiskers linger

around 1 000 km^2 in all intensity change categories except RI, which records near 5 000 km^2, basically showing that it is unusual for RI storms with total IC raining area under that size. Similar to their TMI 2A12 counterparts (Fig. 5.12a) and PR feature-based analysis (Fig. 5.6b), distributions of total IC PR 2A25 volumetric rain (Fig. 5.14a) show the highest values come from RI storms, followed by W, SI, and N storms. However, the difference between RI and W is not very large. Median 2A25 IC volumetric rain values for RI and W storms are 97 400 versus 86 500 $mmhr^{-1}$ km^2, respectively.

Similar to their feature-based counterparts (Fig. 5.6a), distributions of PR 2A25 IC rain rate (Fig. 5.14b) show that W storms have the highest 75th percentile and median rain rate, followed by RI, SI, and N storms. However, the 25th percentile value is the highest for RI, followed by W, SI, and N storms. As mentioned earlier, both the algorithm biases and footprint difference between PR and TMI contribute to the difference of TMI and PR IC rain rate distributions.

Distributions of maximum near surface reflectivity in the storm ICs (Fig. 5.15) show that median values are comparable in RI and W storms, at 49 dBZ and 49.6 dBZ, respectively, and are 2-3 dB higher than those in SI and N storms. Though there is little spread in the median, the 25th and 75th percentiles give extra information. The 25th percentile is the higest in RI storms, followed by W, SI, and N storms, while the 75th percentile is highest in W storms.

The maximum near surface radar reflectivity is indicative of the rate of rain falling, while the maximum heights of radar echoes that meet certain reflectivity thresholds are indicative of the depth of the storm. Fig. 5.16 shows the distributions of maximum heights of 20, 30, and 40 dBZ radar echoes in the storm IC in different

intensity change categories. The 25th and 75th percentiles and median values of the maximum heights of the 20 dBZ echo are all the highest in RI storms, followed by SI, N, and W storms (Fig. 5.16a). These values in RI storms are a few km higher than those in the other intensity change categories. Minimum values of the maximum 20 dBZ heights in the IC region are 2.25, 1, 2.5, and 8 km in W, N, SI, and RI categories, respectively. The maximum 20 dBZ echo reaches at least 8 km for all storms that underwent RI. The 25th and 75th percentiles and median values of the maximum heights of the 30 and 40 dBZ echoes are also the highest in RI storms, followed by W, SI, and N W storms (Fig. 5.16b-c). Interestingly, the minimum values of the maximum 30 and 40 dBZ heights in the IC region in RI storms are 6 and 4 km, respectively, while those in other categories are 0 km. All this says is that for an RI event to occur there must be some measurable convection present.

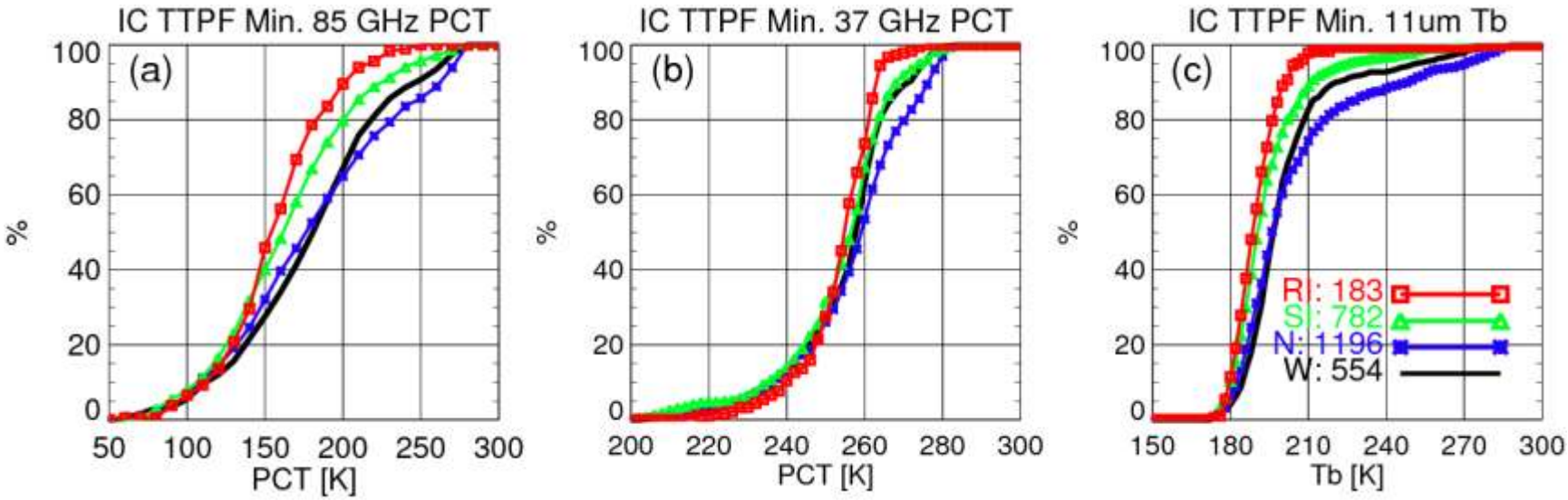

Figure 5.1. CDFs of (a) minimum 85 GHz PCT [K] (b) minimum 37 GHz PCT [K] and (c) minimum 11μm brightness temperature [K] for IC TTPFs in the RI, SI, N, and W intensity change categories.

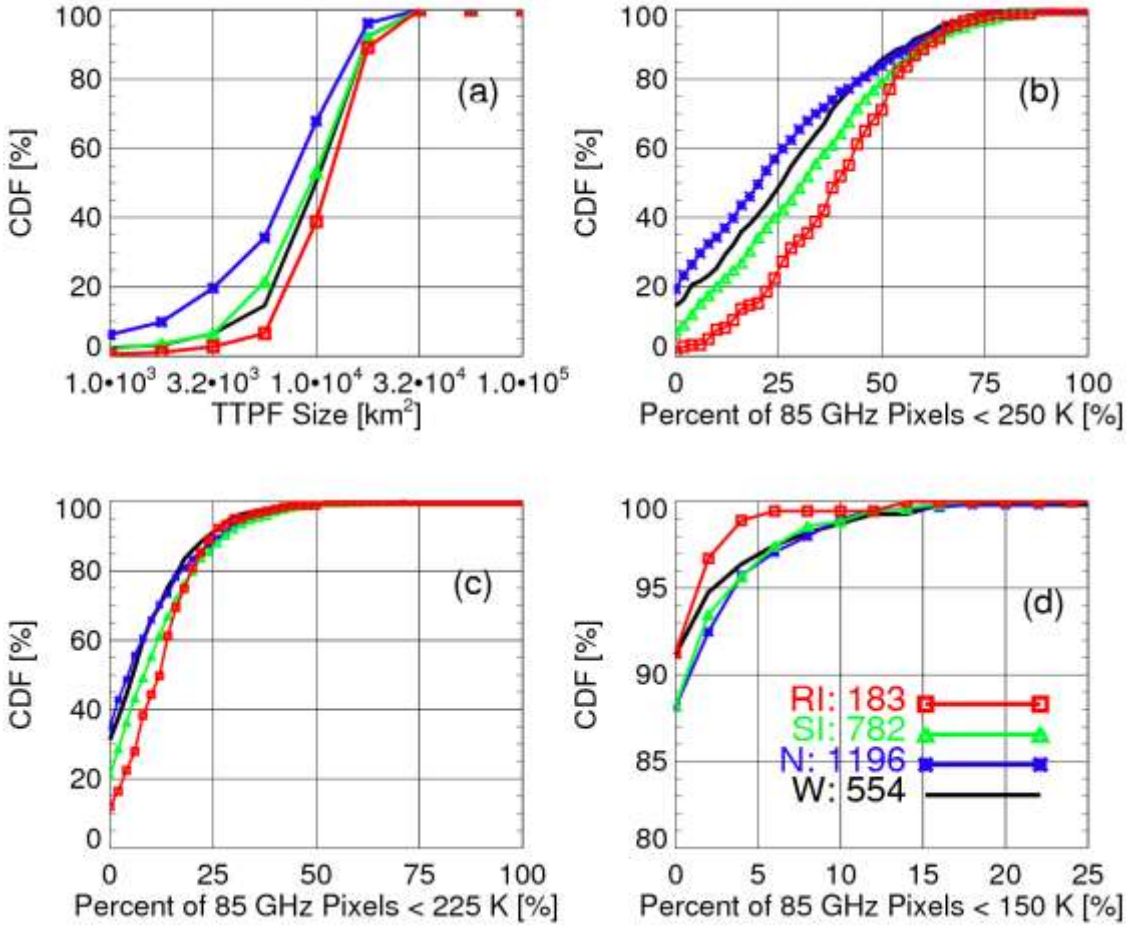

Figure 5.2. CDFs of (a) TTPF size [km^2] (b) percent of 85 GHz PCT pixels less than 250 K [%] (c) percent of 85 GHz PCT pixels less than 225 K [%] and (d) percent of 85 GHz PCT pixels less than 150 K [%] for IC TTPFs in the RI, SI, N, and W intensity change categories.

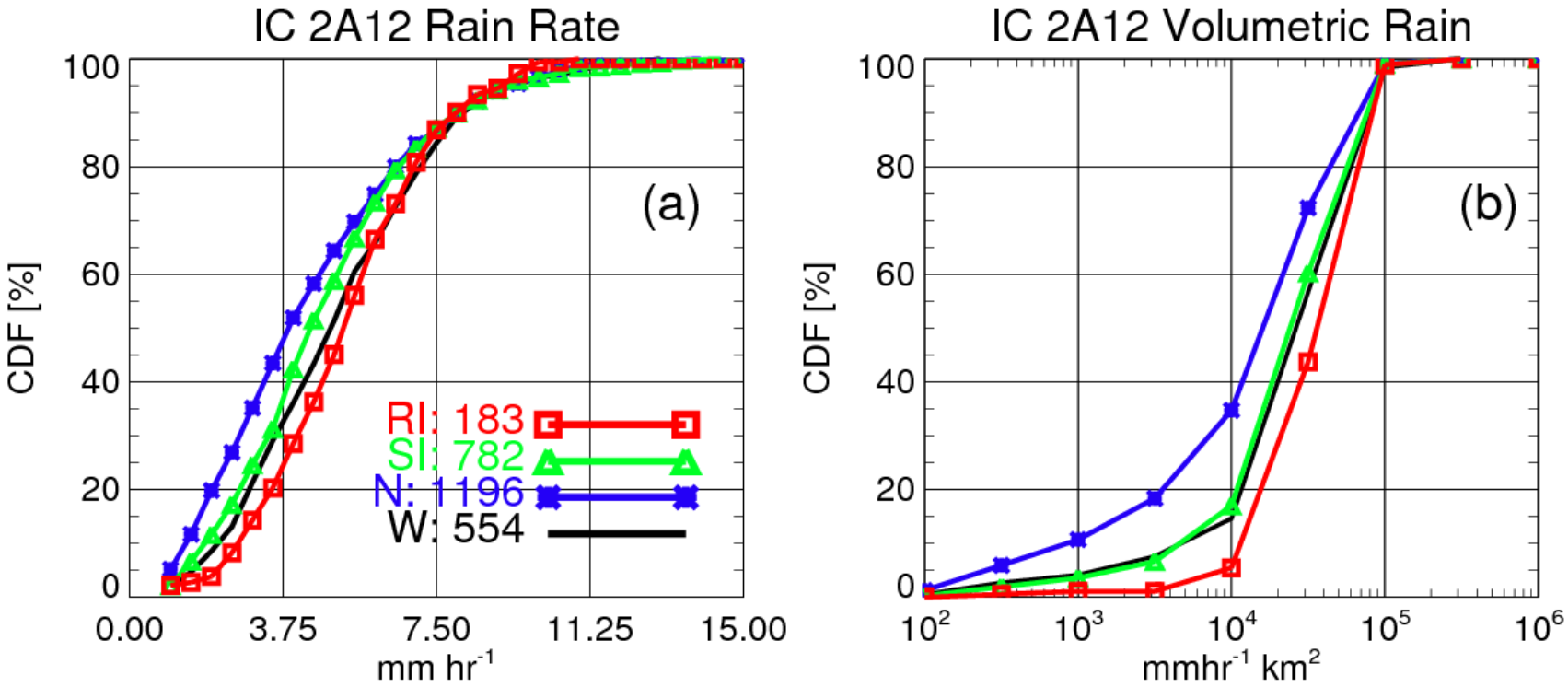

Figure 5.3. CDFs of TMI 2A12 (a) rain rate [$mmhr^{-1}$] and (b) volumetric rain [$mmhr^{-1}$ km^2] for IC TTPFs in the RI, SI, N, and W intensity change categories.

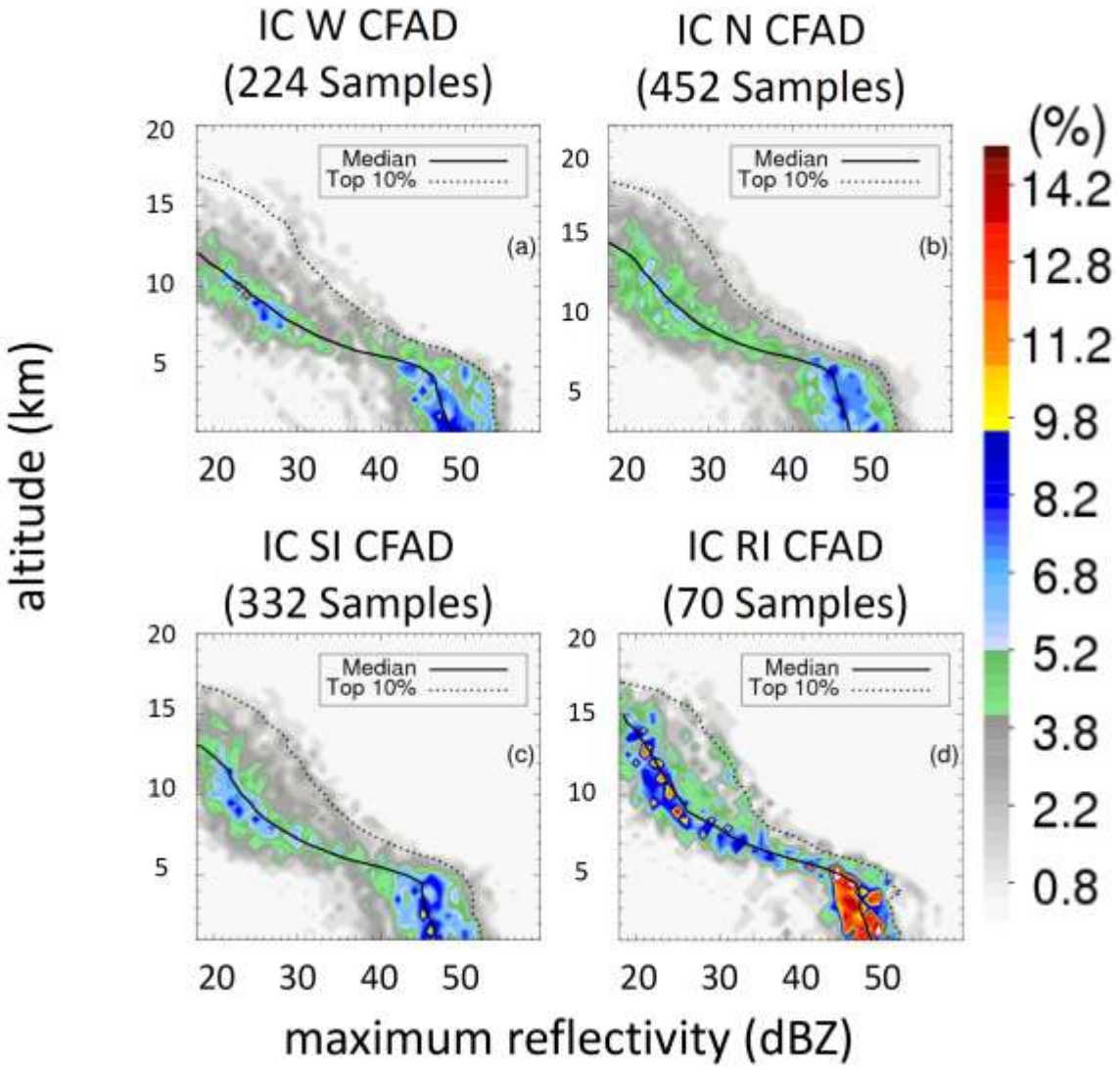

Figure 5.4. CFADs of maximum radar reflectivity of IC RPFs for (a) W (b) N (c) SI and (d) RI intensity change categories. The median maximum reflectivity profile is indicated by the solid black line and the top 10 % of maximum reflectivity profile is indicated by the dotted line.

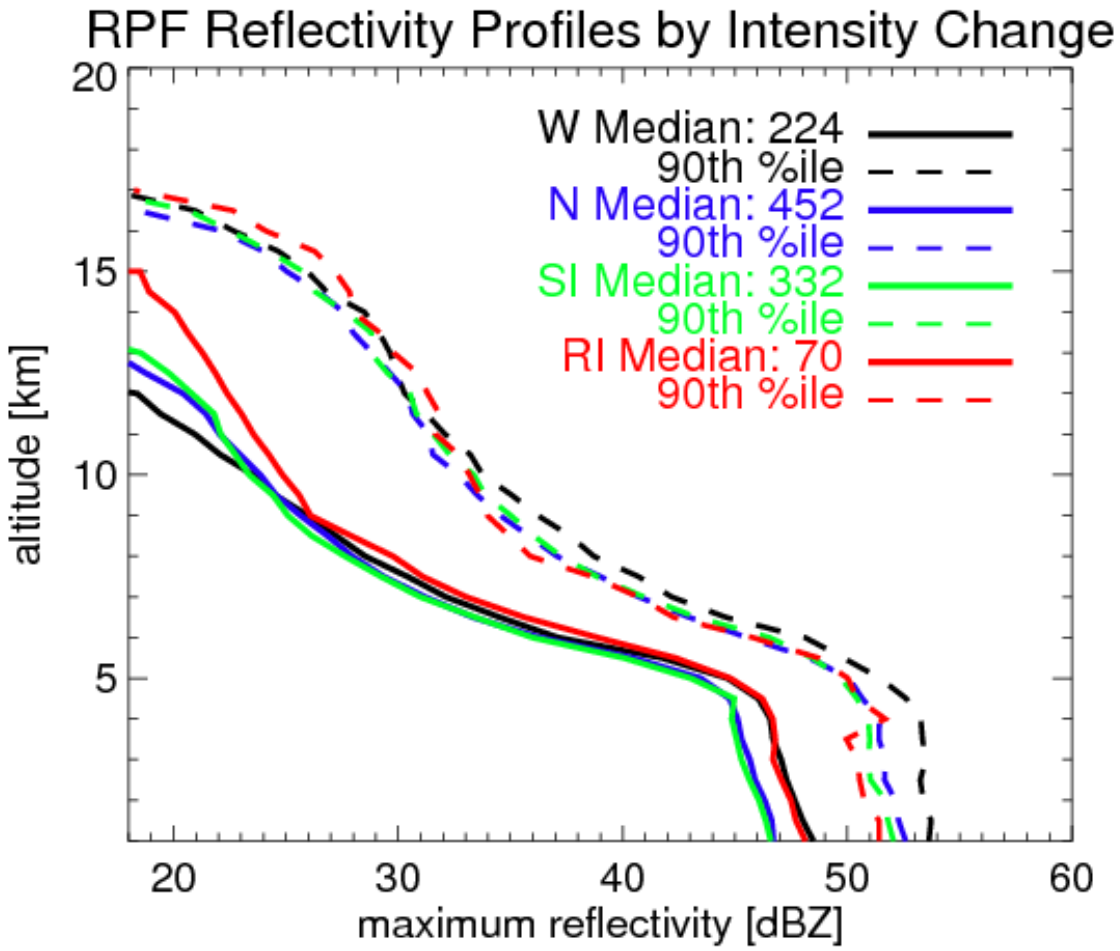

Figure 5.5. Median (solid lines) and 90th percentile (dashed) of vertical profile of maximum radar reflectivity for IC RPFs in W, N, SI, and RI intensity change categories.

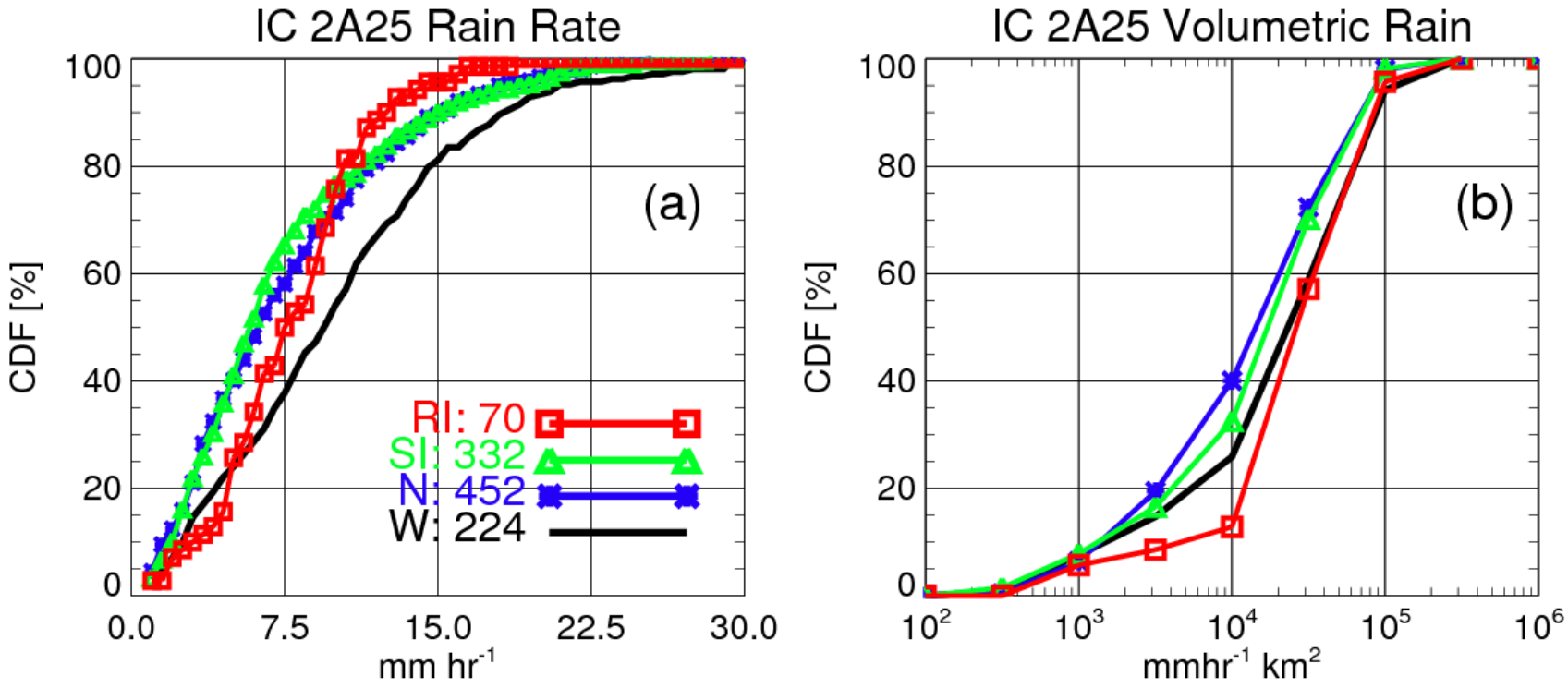

Figure 5.6. CDFs of PR 2A25 (a) rain rate [$mmhr^{-1}$] and (b) volumetric rain [$mmhr^{-1}$ km^2] for IC RPFs in the RI, SI, N, and W intensity change categories.

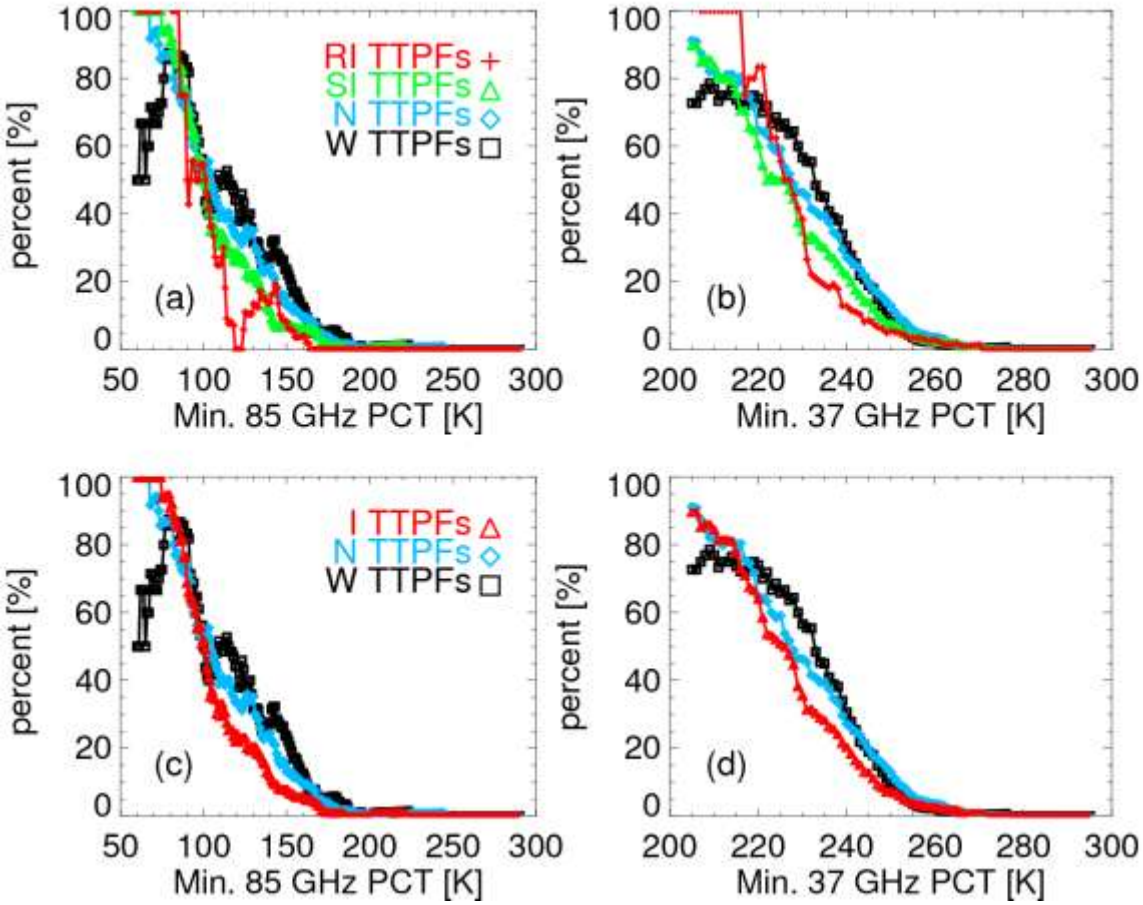

Figure 5.7. Probability of lightning occurrence within- TOP: W, N, SI and RI IC TTPFs BOTTOM: intensifying, neutral, and weakening TCPFs as a function of (a,c) minimum 85 GHz PCT [K] (b,d) minimum 37 GHz PCT [K].

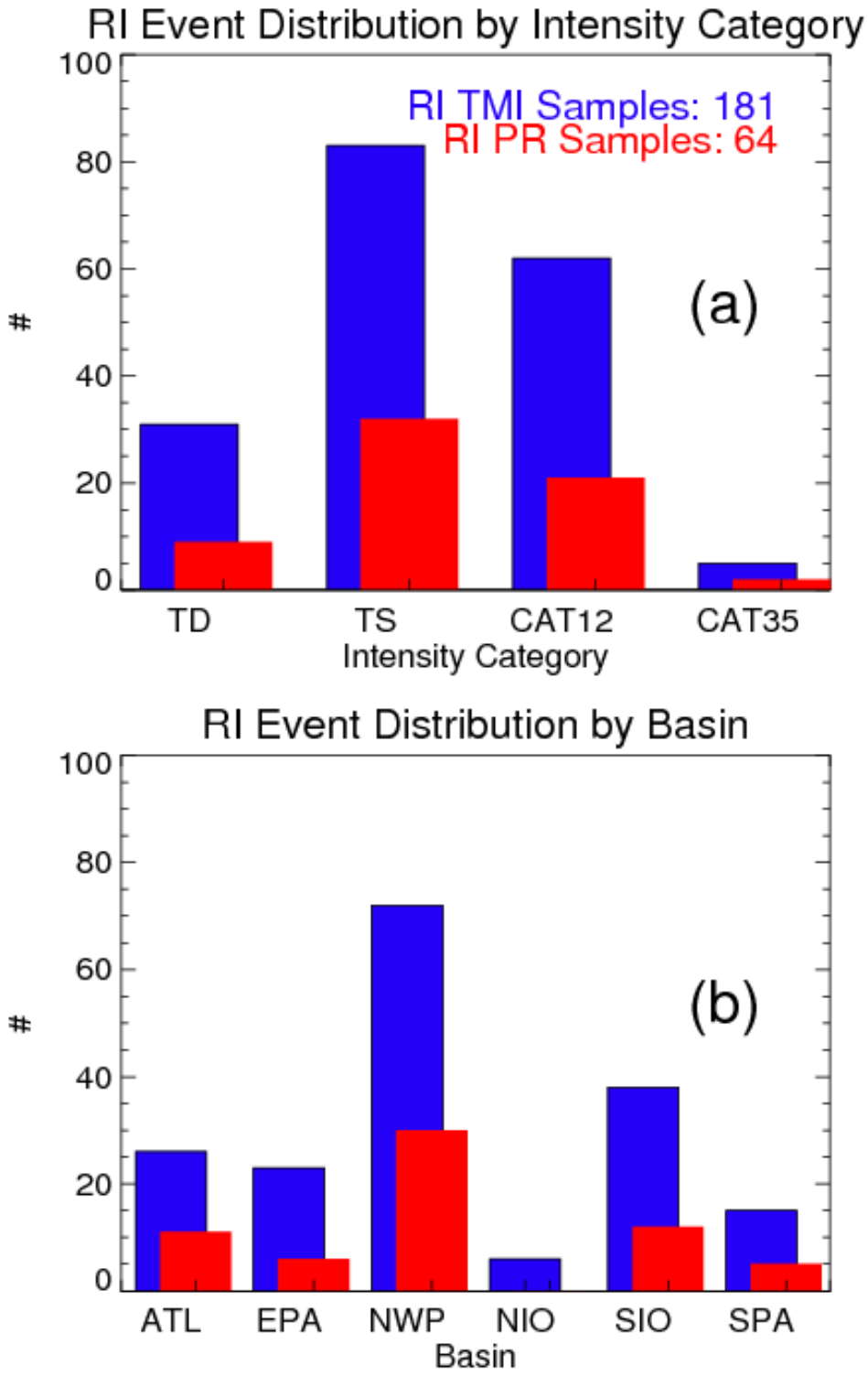

Figure 5.8. Number of storms that underwent RI by (a) intensity category and (b) oceanic basin.

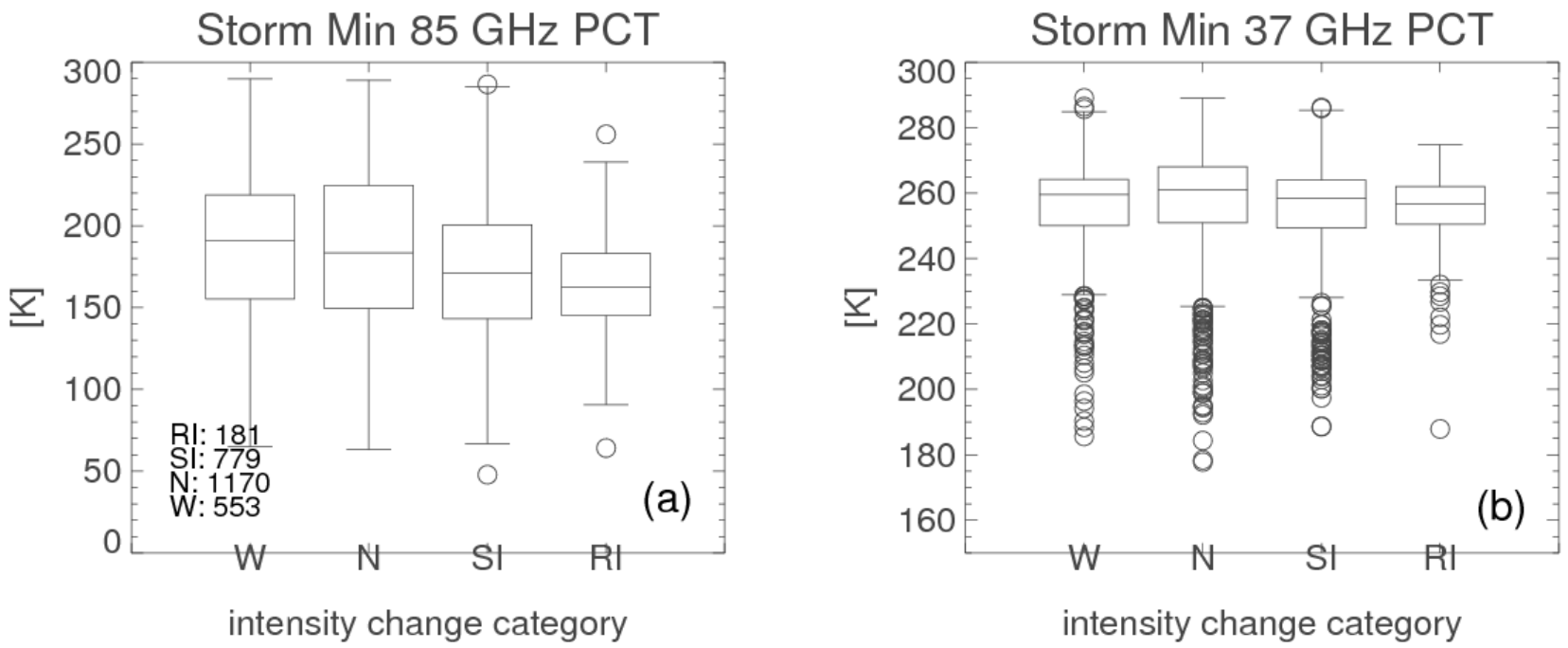

Figure 5.9. Box and whisker plots of (a) minimum 85 GHz PCT and (b) minimum 37 GHz PCT for intensity change categories after combining the individual IC precipitation features in an individual orbit. The top of the box represents the 75%ile, the center line the median, and the bottom of the box the 25%ile. The whiskers extend to 1.5 times the interquartile range and outliers are plotted individually with circles.

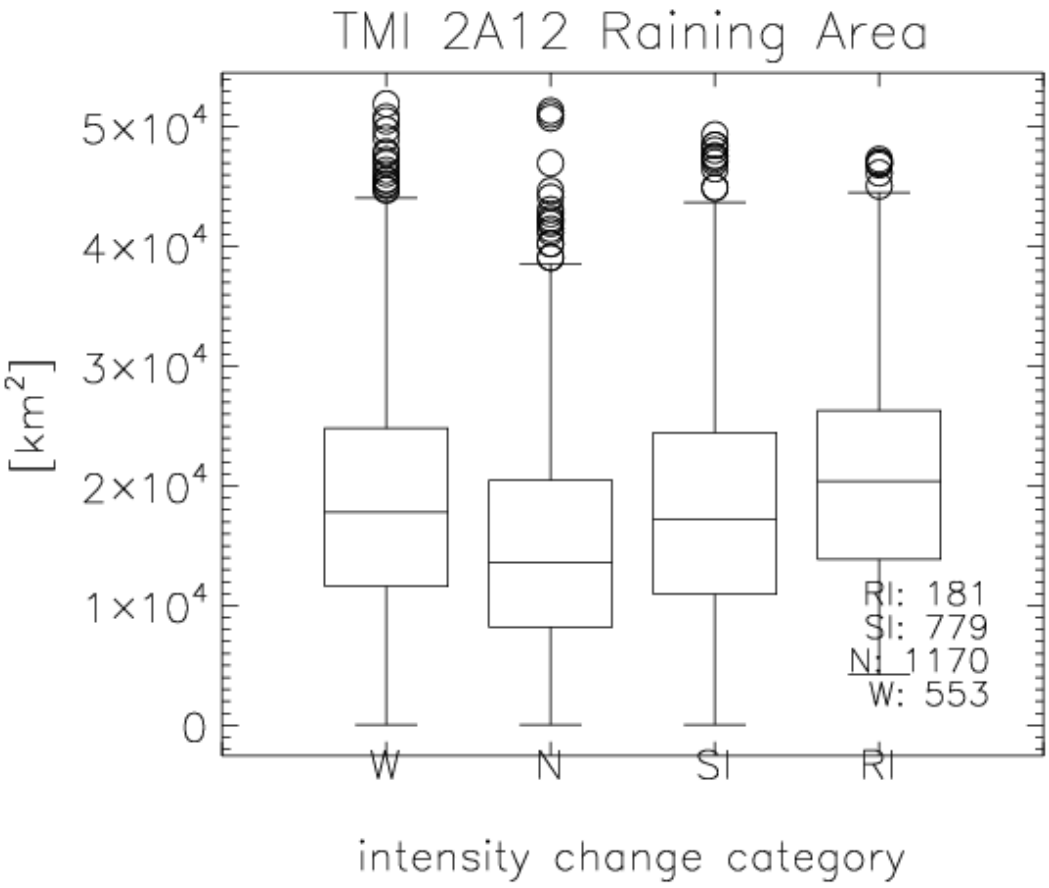

Figure 5.10. Same as Fig. 5.9, but for TMI 2A12 raining area [km^2] in the IC region.

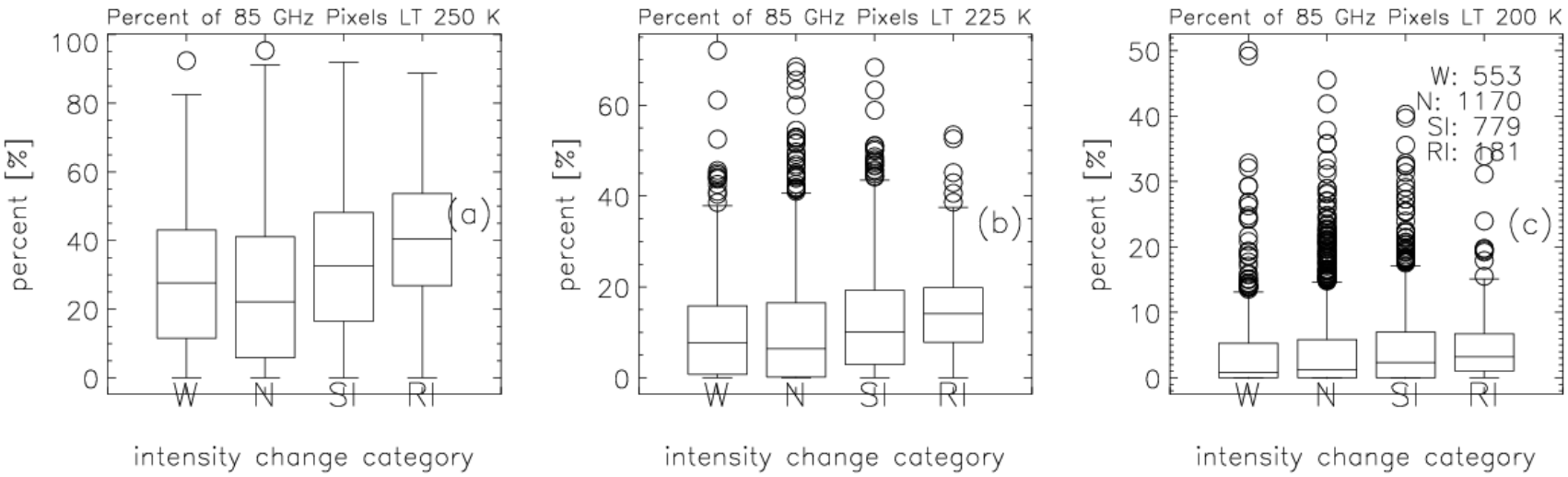

Figure 5.11. Same as Fig. 5.9, but for percentage of pixels in the IC region with 85 GHz PCT less than (a) 250 K (b) 225 K and (c) 200 K.

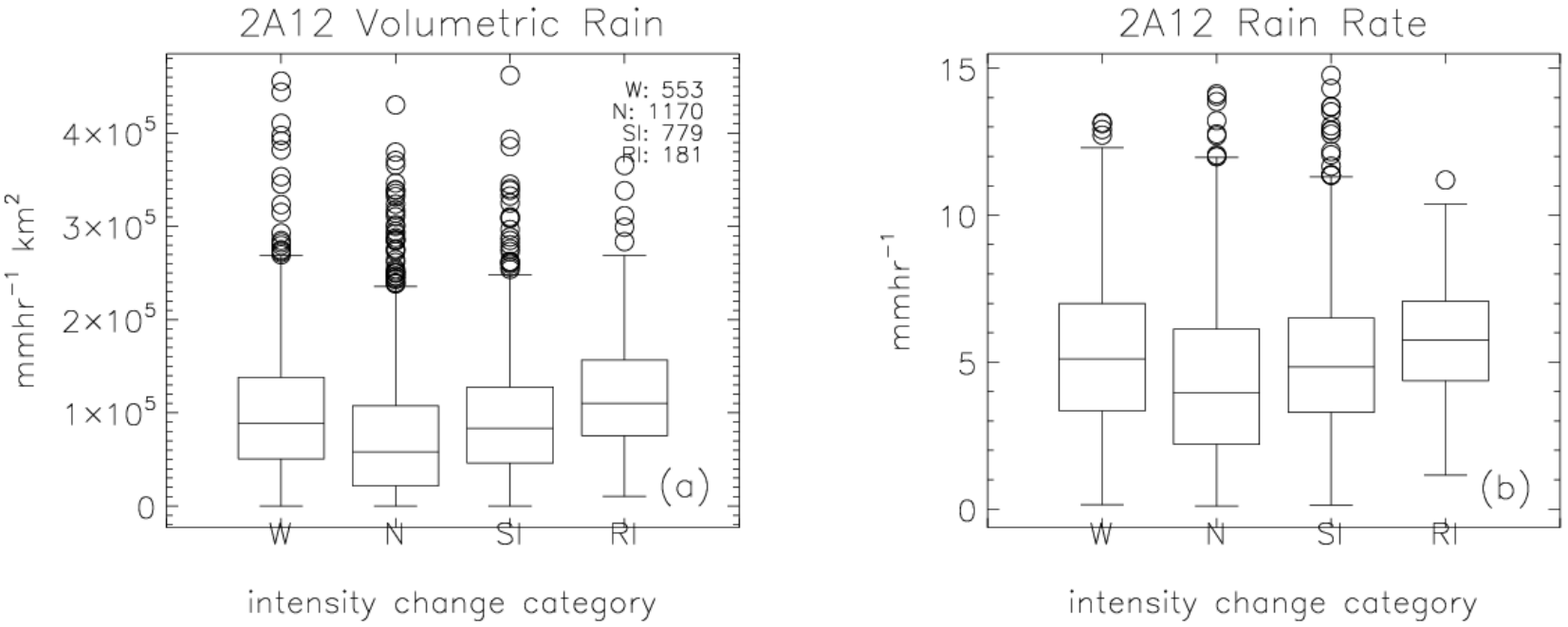

Figure 5.12. Same as Fig. 5.9, but for (a) 2A12 volumetric rain and (b) 2A12 rain rate.

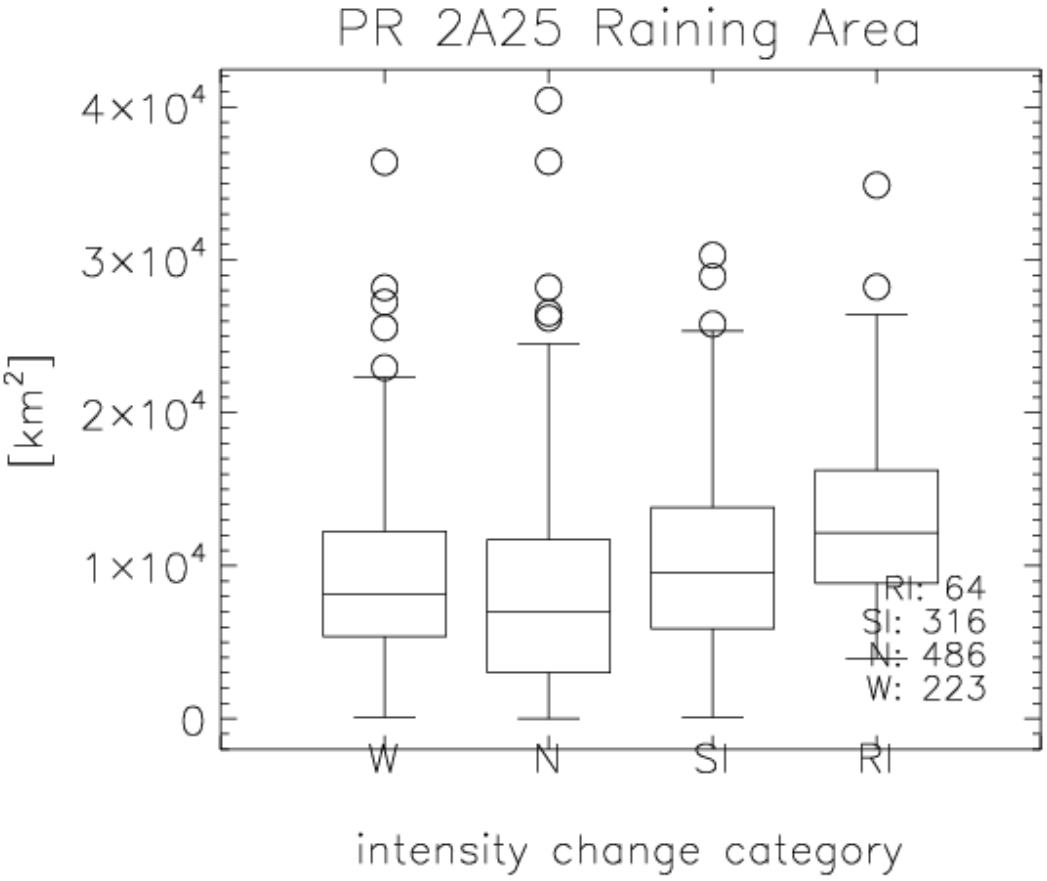

Figure 5.13. Same as Fig. 5.9, but for storm total PR 2A25 raining area [km^2] in the IC region.

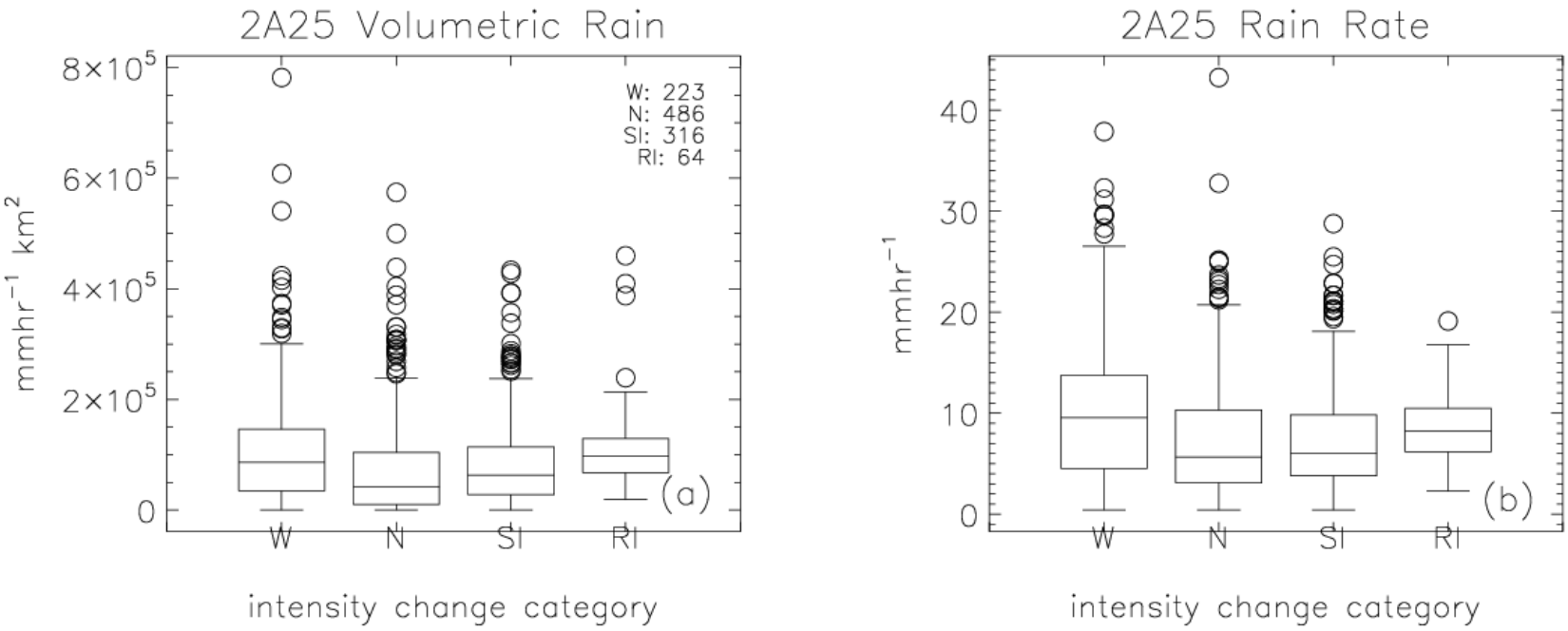

Figure 5.14. Same as Fig. 5.9, but for (a) 2A25 volumetric rain and (b) 2A25 rain rate.

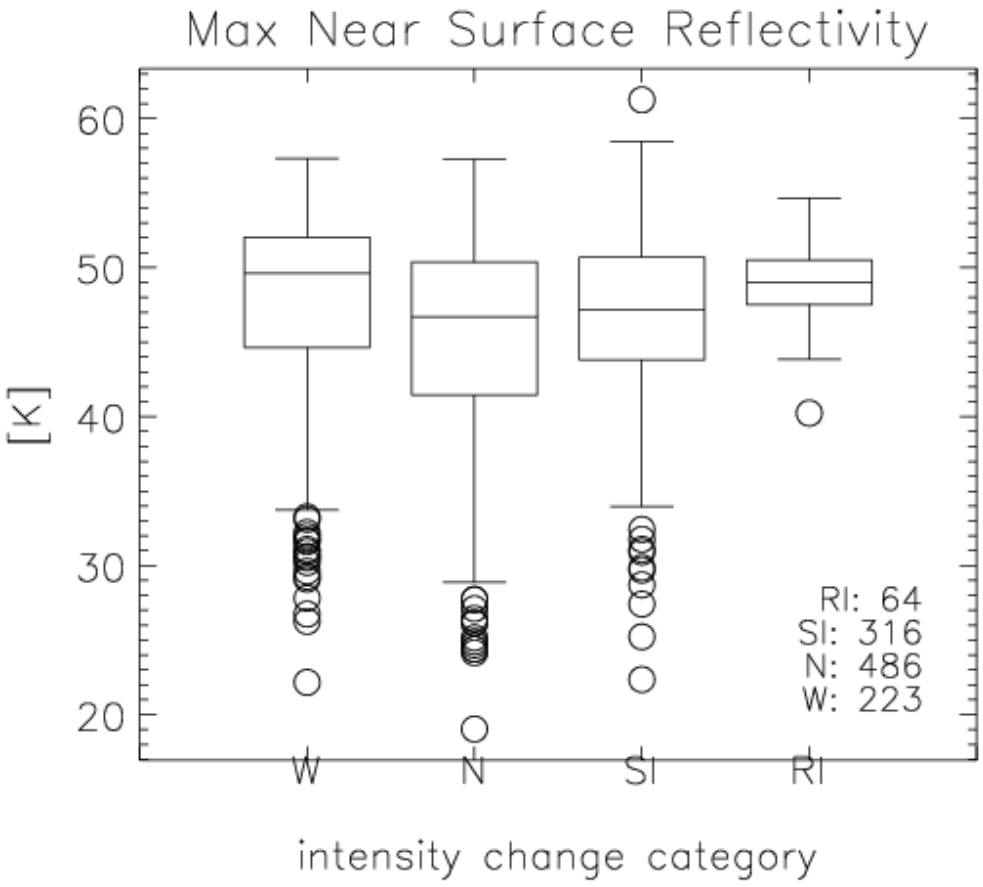

Figure 5.15. Same as Fig. 5.9, but for the maximum near surface radar reflectivity in the IC region.

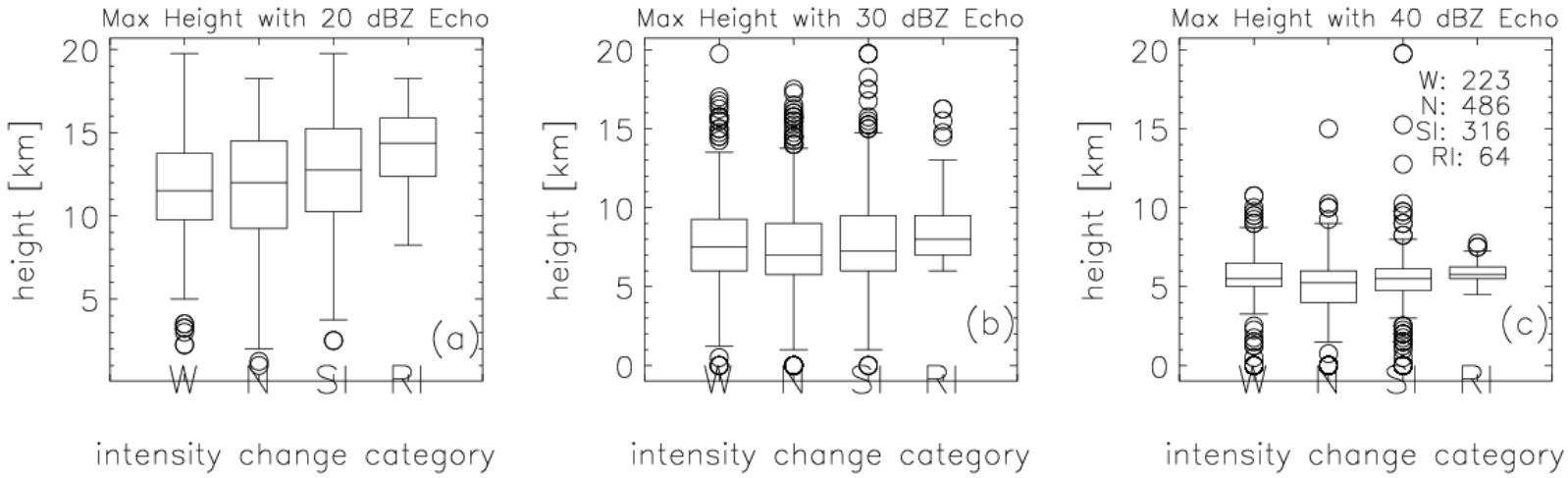

Figure 5.16. Same as Fig. 5.9, but for the maximum altitude of (a) 20 dBZ radar echo (b) 30 dBZ radar echo and (c) 40 dBZ radar echo in the IC region.

Table 5.1. Definition of W, N, SI, and RI intensity change categories and respective IC TTPF population sizes.

Intensity Change	**Maximum Wind Speed Range [kts]**	**IC TTPFs**
W	$v_{max} - v_{max24} \geq 10$	554
N	$v_{max} - v_{max24} < 10$, $v_{max24} - v_{max} < 10$	1196
SI	$30 > v_{max24} - v_{max} \geq 10$	782
RI	$v_{max24} - v_{max} \geq 30$	183
Total		2715

Table 5.2. Same as Table 5.1, but for RPFs.

Intensity Change	**Maximum Wind Speed Range [kts]**	**IC RPFs**
W	$v_{max} - v_{max24} \geq 10$	224
N	$v_{max} - v_{max24} < 10$, $v_{max24} - v_{max} < 10$	452
SI	$30 > v_{max24} - v_{max} \geq 10$	332
RI	$v_{max24} - v_{max} \geq 30$	70
Total		1078

Table 5.3. Number and percentage of IC TTPFs that contain a lightning flash in the W, N, SI, and RI intensity change categories.

Intensity Change Category	ALL IC TTPFs	IC TTPFs W/ Lightning	%
W	609	64	10.5
N	1553	135	8.7
SI	935	84	9.0
RI	194	13	6.7

Table 5.4. Lightning flash counts and ratios of various aspects of sample size to flash count in W, N, SI, and RI TTPFs.

TTPFs	Number of TTPFs w lightning	Number of Flashes	2A12 Rain Area per flash	2A12 Vol. Rain per flash	85 GHz PCT Area < 250 K per flash	85 GHz PCT Area < 225 K per flash	85 GHz PCT Area < 150 K per flash	11μm Tb Area < 235 K per flash	11μm Tb Area < 210 K per flash
	[#]	[#]	[km^2]	[$mmh^{-1}km^2$]	[km^2]	[km^2]	[km^2]	[km^2]	[km^2]
W	64	424	24 400	135 800	7 600	2 600	120	34 000	20 900
N	135	763	22 700	113 300	7 000	2 700	160	32 000	20 100
SI	84	393	35 600	188 000	12 500	4 700	260	53 900	38 400
RI	13	69	56 000	322 500	22 500	7 800	220	89 200	69 400

Table 5.5. Comparison of TMI and LIS derived parameters in the IC region in different intensity change categories after combining the individual IC precipitation features in an individual orbit.

TMI IC Storm Analysis	Total Storms	Total Storms w/ Flash	Percent of Storms w/ Flash	Total # of Flashes	Avg. 2A12 Raining Area	Avg. 2A12 Vol. Rain	Avg. 2A12 Rain Rate	Avg. 85 GHz pixels < 250 K	Avg. 85 GHz pixels < 225 K	Avg. 85 GHz pixels < 200 K
	[#]	[#]	[%]	[#]	[km^2]	[$mmhr^{-1}km^2$]	[$mmhr^{-1}$]	[%]	[%]	[%]
RI	181	13	7.2	69	21 400	122 900	5.8	40.7	14.5	4.8
SI	779	84	10.8	393	17 900	94 800	5	33.4	12.9	4.8
N	1170	135	11.5	763	14 800	73 900	4.3	26.1	10.4	4.1
W	553	64	11.6	424	18 700	103 800	5.2	28.6	10.3	3.5

Table 5.6. Same as Table 5.5, but for PR derived parameters.

PR IC Storm Analysis	Total Storms	Total Storms w/ Flash	% of Storms w/ Flash	Total # of Flashes	Avg. 2A25 Raining Area	Avg. 2A25 Vol. Rain	Avg. 2A25 Rain Rate	Avg. Max Height of 20 dBZ echo	Avg. Max Height of 30 dBZ echo	Avg. Max Height of 40 dBZ echo
	[#]	[#]	[%]	[#]	[km^2]	[$mmhr^{-1}km^2$]	[$mmhr^{-1}$]	[km]	[km]	[km]
RI	64	4	6.3	18	13 200	117 000	8.6	14.1	8.9	5.9
SI	316	36	11.4	171	10 100	84 100	7.6	12.7	8.2	5.2
N	486	51	10.5	308	8 000	70 900	7.3	11.6	7.5	4.6
W	223	21	9.4	76	9 500	112 600	10.1	11.6	7.9	5.2

CHAPTER 6

SUMMARY AND CONCLUSIONS

Using TRMM passive microwave radiometer, IR, radar, and lightning data, this study has 1) intercompared the convective and rainfall properties of precipitation features in the TC IC, IB, and OB regions, 2) quantitatively investigated differences in convective and rainfall properties of precipitation features in the IC region among TD, TS, CAT12, and CAT35 categories, and 3) quantitatively examined the relationship between TC IC rainfall and convective proxies and 24-h TC intensity changes, including weakening, neutral, slowly intensifying, and rapidly intensifying.

6.1 Inner Core, Inner Rainband, Outer Rainband

The IC region is dominated by relatively large features with moderate to strong convective signatures, while smaller and warmer features are abundant in both IB and OB regions. Strong convective signatures are more often found in the IC region, less often in the IB region, and least often in the OB region when examining features with size greater than 1000 km^2. This is seen in radar reflectivity, 85/37 GHz PCT, and IR brightness temperature. After using MCS criteria (defined in Section 3.1), similar magnitudes of ice scattering signatures are found in IC and OB features, and much lower magnitudes in IB features. As noted in previous studies, the IB region is dominated by stratiform rain and rather weak convection (Fig. 3.5). This result is consistent with previous studies using

TRMM (Cecil et al. 2002), aircraft radar (Szoke et al. 1986), lightning (Molinari et al. 1999) data, and the updraft magnitude (Jorgensen et al. 1985, Black et al. 1996).

By examining both TMI 2A12 and PR 2A25 rain retrievals, features in the IC region are found to have higher conditionally averaged rain rates than features in the IB and OB regions, while those of the IB region remain higher than those of the OB region. This is consistent with previous studies that found a decrease of the mean rain rate as the radial distance from the TC center increases (Rodgers et al. 2001, Lonfat et al. 2004, Jiang et al. 2006).

For all features without the 1000 km^2 size restriction, the percentage with lightning in the IC region is about a factor of 2 higher than the percentages found in the IB and OB regions. After normalized by the total 2A12 precipitation area, the flash density in the IC region is 2 times greater than in the OB region, and about 4 times greater than in the IB region. When normalized by the area occupied by convection, lightning flash densities in the IC and OB regions are comparable and about 2-3 times greater than in the IB region. In contrast, with a much smaller sample size, Cecil et al. (2002) found that normalized by the 2A25 total precipitation area, the flash densities are 4 times greater in the eyewall and outer rainband region than in the inner rainband region, while these flash densities are similar in the eyewall, inner rain band, and outer rainband region when normalized by the convective area.

The probability of a feature having lightning begins to increase as minimum 85 (37) GHz PCT decreases below about 210 (270) K in the OB region or 180 (255) K in the IC and IB region. Within these brightness temperatures, an OB feature is more likely to have a lightning flash than an IC or IB feature for a same given minimum 85 or 37 GHz

PCT value. OB features have between 10-25% higher likelihood of lightning for a given maximum dBZ at 6, 8, 10, and 12 km altitudes than IC and OB features. This result is consistent with the speculation of Cecil and Zipser (2002) that the OB region has more supercooled liquid water than the IC and IB region.

6.2 TC Intensity in Relation to Convective and Rainfall Properties in the IC Region

The relationship between storm intensity and convective parameters as extreme point values, i.e., minimum 85 and 37 GHz PCTs and maximum radar reflectivity profiles in IC features are not as good as expected. In contrast, a close relationship between TC intensity and *area* of 85 GHz PCT less than 250 and 225 K is observed. Similarly, Cecil and Zipser (1999) found that TC intensity is highly correlated with average 85 GHz PCT and area of 85 GHz PCT less than 250 and 225 K in the eyewall region.

Both the IC conditional mean rain rate and volumetric rain increase as storm intensity increases. This is true from both TMI 2A12 and PR 2A25 retrievals. Previous studies using SSM/I (Rodgers et al. 2000, 2001), TMI (Lonfat et al. 2004), and TRMM 3B42 (Jiang et al. 2006, Jiang and Zipser 2010) rainfall products also found a similar relationship.

No direct relationship is seen between lightning in the IC region and TC intensity, other than that major hurricanes have lightning more often than weaker TCs. While the IC region in major hurricanes has the highest percent (20%) of features with lightning, the second highest percent (10%) is from TSs, followed by CAT12 hurricanes (8%) and TDs (7%). Similarly, Cecil and Zipser (1999) found that the fraction of the sample with

lightning is the highest for TSs, followed by major hurricanes, then category 1-2 hurricanes and TDs.

6.3 TC Intensity Change in Relation to Convective and Rainfall Properties in the IC Region

At the weaker end of the convective spectrum, there is a minimum threshold of convective properties in the IC region for storms undergoing RI. The necessary conditions for RI are that the minimum 85 GHz PCT in the IC region must be less than 256 K, the minimum 37 GHz PCT in the IC region must be less than 275 K, and the maximum 20 (30, 40) dBZ echo height in the IC region must be equal to or greater than 8 (6, 4) km (Fig. 5.13). Over 98% of RI minimum 11μm Tbs in the IC region are less than 212 K (Fig. 5.1), three outliers exist. In the middle of the convective spectrum (indicated by the median values of the distributions), the convective intensity in the IC region is higher for features associated with RI storms than those in other intensity change stages (Fig. 5.5; solid lines). However, at the stronger end of the convective spectrum, RI features do not necessarily have stronger convective intensity in the IC region than features in other intensity change stages (Fig. 5.5; dashed lines). Extremely intense convection, therefore, is not the sufficient condition for RI. Modest ice scattering signatures, cloud top heights, and radar reflectivities are, however, necessary conditions for RI.

Although IC conditional mean rain rate is not a good indicator of RI, both IC raining area and IC volumetric rain are. From both TMI 2A12 and PR 2A25 data, it is found that RI storms always have larger raining area and volumetric rain in the IC region than storms in other intensity change stages. This implies that the chance of RI increases

when a storm's raining area in the IC region increases. In most cases, this means the storm becomes more symmetric. Cecil and Zipser (1999) and Kerns and Zipser (2009) also found that the spatial coverage of at least moderate inner core rainfall is highly correlated with TC intensification.

Although previous studies found that lightning might be a precursor of TC intensification (Price et al. 2009, Leary and Ritchie 2009), this study's findings indicate that a negative relationship might exist between TC intensification and lightning activity in the IC region (Table 5.3). Due to the limitation of LIS samples, it is too early to make stronger conclusions.

APPENDIX

REMOTE SENSING PRINCIPLES

Atmospheric remote sensing is the science of acquiring information about the Earth and its atmosphere by measuring upwelled or backscattered electromagnetic radiation (EMR). Understanding the spectral distribution and behavior of EMR as it interacts with matter allows continuous monitoring of atmospheric processes in data sparse regions.

A.1 Blackbody Radiation

EMR is comprised of a spatially varying electric field and a time varying magnetic field or vice versa. One field induces the other and so they oscillate in phase perpendicular to each other and perpendicular to the direction of energy propagation. EMR is commonly referenced by wavelength, the distance from wave peak to wave peak. Frequency is inversely related to wavelength by $f = c/\lambda$, where $c = 3 \times 10^8$ m s^{-1} is the speed of light. One source of EMR is the sun, which has its peak energy flux in the visible realm, 400-700nm. The Earth absorbs the EMR from the sun and re-radiates it at a much lower energy level, peaking in the IR near 10μm. Solar radiation is termed *shortwave* and terrestrial radiation termed *longwave* because of their relative wavelengths of emission.

A blackbody is a theoretical object which absorbs and emits all incident radiation isotropically in all wavelength bands. A blackbody is a perfect emitter and absorber. Blackbody temperature is the temperature an object would have were it behaving as a

blackbody. At the end of the 19th century, Wilhelm Wien attempted to mathematically explain the spectral radiance of a blackbody. The solutions, expressed in terms of wavelength (Eq. A.1) and frequency (Eq. A.2), were good approximations at short wavelengths but bad approximations at long wavelengths.

$$I(\lambda,T)=\frac{2hc^2}{\lambda^5}e^{-\frac{hc}{\lambda KT}} \qquad \text{A.1}$$

$$I(\nu,T)=\frac{2h\nu^3}{c^2}e^{-\frac{h\nu}{KT}} \qquad \text{A.2}$$

The symbol I represents the energy per unit time per unit surface area per unit solid angle, h =6.626x10^{-34} J is Planck's constant, and K =1.381x10^{-23} J K^{-1} is Boltzmann's constant. Shortly after, Lord Rayleigh and Sir James Jeans attempted to solve the same problem by empirically deriving and experimentally testing their own equation, famously known as the Rayleigh-Jeans (RJ) approximation (Eqs. A.3-4). Converse to Wien's result, the expression is valid at long λ but goes to infinity as λ becomes small.

$$I(\lambda,T)=\frac{2cKT}{\lambda^4} \qquad \text{A.3}$$

$$I(\nu,T)=\frac{2\nu^2KT}{c^2} \qquad \text{A.4}$$

Though the expressions fail at small wavelength, they are extremely useful in the microwave regime. Since passive microwave sensing, by definition, uses a longer

wavelength regime, the RJ approximation can be applied to simplify radiative transfer calculations.

At the beginning of the 20th century, Max Planck successfully derived an expression for the distribution of blackbody radiation agreeable over all wavelengths, by assuming that energy is quantized and proportional to the frequency, ν.

$$I(\lambda,T)=\frac{2hc^2}{\lambda^5}\frac{1}{e^{hc/\lambda KT}-1} \qquad \text{A.5}$$

$$I(\nu,T)=\frac{2h\nu^3}{c^2}\frac{1}{e^{h\nu/KT}-1} \qquad \text{A.6}$$

Planck's radiation law says that for a given temperature, *T*, and specific wavelength, *λ*, or frequency, *v*, there is an upper bound on the intensity of radiation. The upper limits of the sun and Earth reveal two important points: (1) Energy fluxes are not equal for all wavelengths, e.g., there is a peak wavelength, and (2) Energy flux magnitudes are not equal for all emitters. With regard to the first point, prior to Planck's Law of Blackbody Radiation, Wien experimentally found that the wavelength of maximum emission is inversely proportional to the temperature of the object. Wien's Displacement Law (Eq. A.7) states that the radiated energy from a blackbody has essentially the same shape but the wavelength of peak emission is displaced depending *only* on the temperature. This explains why the sun (5800 K) peaks in the visible region at 0.5μm and the Earth (mean surface temperature of 288 K) peaks in the IR at 10μm.

$$\lambda_{max}=2897\mu m / T \qquad \text{A.7}$$

The same equation can be mathematically derived by differentiating the Planck function with respect to wavelength. With regard to the second point, *intensity* of the energy flux can be derived by integrating the Planck function over all wavelengths, first done by Jozef Stefan and Ludwig Boltzmann. The Stefan-Boltzmann (SB) Law (Eq. A.8) says that for perfect radiators, the total amount of radiant heat energy is proportional to the fourth power of the blackbody temperature.

$$F=\sigma T^4 \qquad \text{A.8}$$

The Stefan-Boltzmann constant is represented by σ, where $\sigma = 5.67 \times 10^{-8}$ W m^{-2} K^{-4}. For imperfect emitters the equation is multiplied by the emissivity, ε.

$$F=\varepsilon\sigma T^4 \qquad \text{A.9}$$

The emissivity is the ratio of an object's emission to its blackbody emission. Kirchhoff's Law (Eq. A.10) says that emissivity equals absorption for a given λ and T, which is true in order for objects to maintain thermal equilibrium. A good absorber is a good emitter.

$$\varepsilon_\lambda = \alpha_\lambda \qquad \text{A.10}$$

A measured radiant intensity is converted into an equivalent blackbody temperature by inverting the Planck function. This temperature is termed the *brightness temperature,* T_b. Using the RJ approximation (valid in the microwave region) the relationship between the physical temperature and the brightness temperature reduces to Eq. A.11.

$$T_b \approx \varepsilon_\lambda T \qquad \text{A.11}$$

A.2 Radiative Transfer Equation

The radiative transfer equation describes how an incident beam of energy with wavelength λ, along path *s*, interacts with matter. Modes of EM energy transfer include absorption / emission, scattering, and transmission. The total incident energy on an object must be equal to the sum of the energy absorbed, scattered, and transmitted. Absorption is the temporary destruction of EMR, because the object acquires the energy. Emission is a source of EMR because it departs from the object. Scattering is the change in direction after an interaction with matter has taken place, which can be probabilistically explained. During transmission there is effectively no interaction and EMR simply passes through. Both absorption and scattering remove energy from a beam of radiation, and this extinction of radiation is termed *attenuation*. However, energy can then be emitted or scattered into another beam of radiation that may be of interest. The geometric area of a particle, called the *cross sectional area*, denoted by σ [m^2], is used to calculate the scattering efficiency in a given beam. The refractive index refers to the ratio of the speed of light in vacuum to the speed at which the EMR travels through a medium. The refractive indices of air, water and ice are 1.0003, 1.33 and 1.31, respectively. This means that light travels through a vacuum 1.31 times faster than it would through ice. Therefore, different atmospheric compositions create different angles through which the radiation will be bent.

$$I_\lambda(s) = I_{0,\lambda} e^{-\chi\lambda(s)} - \int_{s=0}^{s=\chi_\lambda} \left[(1-\omega_\lambda) B_\lambda(T) + \frac{\omega_\lambda}{4\pi} \int_{4\pi} I_\lambda(\hat{\Omega}') P_\lambda(\hat{\Omega}, \hat{\Omega}') d\hat{\Omega}' \right] e^{(\chi_\lambda(s) - \chi'_\lambda(s))} d\chi'_\lambda \qquad \text{A.12}$$

attenuation of incident energy — **emission** — **scattering** — **attenuation**

The first term on the right hand side of Eq. A.12 accounts for the attenuation of incident energy along its path. The two terms inside the brackets are called the *source function*, which calculates how energy might be added into the increment of solid angle of interest by emission or scattering. The exponential function outside the brackets explains how the source function energy is attenuated from s' to s.

A.3 Rayleigh Theory

Rayleigh scattering occurs by particles that are small with respect to the wavelength. Equation A.13 is the Rayleigh scattering equation for a single particle from a beam of unpolarized light.

$$I = I_0 \frac{1+\cos^2\theta}{2R^2} \left(\frac{2\pi}{\lambda} \right)^4 \left(\frac{n^2-1}{n^2+2} \right)^2 \left(\frac{d}{2} \right)^6 \qquad \text{A.13}$$

R is the distance from the observer to the particle, θ is the scattering angle, n is the refractive index and d is the particle diameter. The intensity of scattered light varies inversely with the 4th power of the wavelength and directly with the 6th power of the drop diameter. Rayleigh scattering is therefore strongly dependent upon both the size of the particle and the wavelength. Radiation is distributed equally in the forward and rearward directions, and slightly less at a 90 degree angle (Fig A.1a).

Rayleigh scattering principles are no longer valid when the particle size exceeds the wavelength of the incident radiation by more than 10%.

A.4 Mie Theory

Mie theory is an analytical solution of Maxwell's Equations for the scattering of EMR by spherical particles with sizes comparable to or greater than the wavelength. This ratio of particle size to wavelength is calculated using the size parameter, X (Eq. A.14).

$$X=2\pi r/\lambda \qquad \text{A.14}$$

The radius of a particle is represented by r, and wavelength by λ. Mie's scattering model finds the intensity of the scattered radiation by computing the summation of an infinite series, as opposed to a mathematical expression as in Rayleigh theory. When the wavelength is similar to the particle diameter, light interacts over a cross-sectional area larger than that of the geometric cross-sectional area due to the physical blocking of light and diffraction. The Mie model computes the scattering cross section, C_{sca}, which is subsequently used to calculate the dimensionless scattering efficiency parameter, Q_{sca}, the ratio of the scattering cross sectional area to the geometric cross-sectional area.

$$Q_{sca} = C_{sca}/\pi\, r^2 \qquad \text{A.15}$$

With increasing size parameter, Q_{sca} converges about a value of 2 (Fig. A.2), meaning the effective scattering cross section becomes twice the geometrical cross-section.

Mie scattering differs from Rayleigh scattering in that Mie is roughly independent of wavelength and scattering is preferential in the forward direction (Fig. A.1b-c). This is the result of constructive interference of waves scattered from different parts of the particle, which collectively favor the forward direction.

A.5 Passive Sensing

Passive remote sensing is the technique of measuring naturally emitted radiation with a radiometer. The source of energy is external to the sensor. Passive *microwave* instruments are sensitive to energy at specific frequencies ranging from 3-300 GHz, called the microwave band. The spatial resolution is determined by a combination of footprint size, which is a function of the altitude and beam width. The temporal resolution is determined mainly by the orbit and swath width. The inclination of the orbit and the altitude determine whether the orbit is sun-synchronous. Examples of passive microwave sensors include the Scanning Multi-Channel Microwave Radiometer (SMMR), the Special Sensor Microwave Imager (SSM/I), and the Advanced Microwave Scanning Radiometer- Earth Observing System (AMSR-E). The SMMR operated on the Nimbus-7 satellite from 1978-1987 and has a 50 degree incidence angle at Earth's surface, which provides a 780 km swath width. The SSM/I has 0.25 degree spatial resolution, and operates over 7 different channels with a 1400 km conical scan. The AMSRE-E conically scans, operates over 12 channels, and has dual polarization. It has an altitude of 705 km, a swath width of 1445 km, and an incidence angle of 55 degree at Earth's surface.

A.5.1 Emission Based Algorithms

Emission based algorithms rely on the brightness temperature contrast between the ocean surface and atmospheric hydrometeors. The ocean emits microwave energy proportional to the surface emissivity multiplied by the surface temperature, where the emissivity depends on frequency, incidence angle, polarization, and the index of refraction (Kummerow et al. 1996). The ocean has a uniformly low emissivity making it appear colder than its thermodynamic temperature. Conversely, raindrops have high emissivities and exhibit brightness temperatures nearly equivalent to their thermodynamic temperature. The contrast between liquid hydrometeors and the ocean surface provides information about the liquid water path. Greater temperature differences equate to higher volumes of rain. Since long wavelengths are less sensitive to the effects of ice scattering that are important at 37 GHz, and even more so at higher frequencies, the 10 GHz and 19 GHz channels are better suited for emission methods. Nearly all liquid hydrometeors are in the Rayleigh regime for 10 and 19 GHz channels. Emission based algorithms break down over land because of varying surface emissivities including those of forests, deserts, urban regions, fields, and swamps.

A.5.2 Scattering Based Algorithms

Scattering based rain algorithms are developed from experimentally correlating ice scattering temperature depressions with rain rates. When ice particles scatter upwelled radiation, the sensor measures a colder temperature. This column integrated result of emission and scattering processes infers the depth of the ice water path (IWP). A scattering index is assigned from a lookup table and is used to compute a rain rate. This method performs surprisingly well in general, but assumes that the presence of ice aloft

implies precipitation at the surface. The 85 GHz and 37 GHz channels are best suited for measuring ice scattering signatures because of their ability to resolve medium to large sized ice particles. Ice scattering at 85 GHz is carried out by particles down to a few hundred microns while ice scattering at 37 GHz is sensitive only to mm size graupel and hydrometeors. Eighty-five GHz temperature *depressions* can be as much as 150 K over deep convective storms (Kummerow et al. 1996), and sometimes even greater. Since both oceanic and continental storms can contain ice, the scattering technique *can* be employed over ocean but *must* be employed over land.

A.6 Active Sensing

Active sensing is the method of measuring the return strength of a transmitted signal. The source of energy is internal to the sensor. A radar is an active sensor which emits electromagnetic pulses at known frequencies and then listens for the return signal. The distance of the object can be calculated by the elapsed time.

A.6.1 Radar Equation for Distributed Targets

The radar equation describes the diminution of transmitted power from interacting with distributed targets of known radius. The power received is given either in terms of the antenna gain or the antenna area.

$$\mathrm{P_r} = \frac{P_t G^2 \lambda^2 \sigma}{(4\pi)^3 R^4} = \frac{P_t A^2 \sigma}{4\pi \lambda^2 R^4} \qquad \text{A.16}$$

P_t is the power transmitted with an antenna gain G_t. Gain is a known value of the antenna and is a measure of the antenna's ability to focus outgoing energy into the beam. The power received from a given target is directly related to the square of the antenna gain

(Eq. A.16). A is the effective aperture of the receiving antenna, λ is wavelength, σ is the radar scattering cross section, and R is the range, or distance from the target to the transmitter / receiver. Range is calculated by the time it takes the transmitted signal to return. The average power returned is inversely related to the square of the range for both the outgoing and return trip and therefore becomes R^4 (if transmitter and receiver are collocated).

A.6.2 Radar Rainfall Retrieval

Measured radar reflectivity is a function of the rain rate and drop size distribution (DSD), so with an assumed DSD a direct relationship exists between radar reflectivity and rain rate. Marshall and Palmer (1948) empirically derived the following power law to relate the reflectivity factor Z ($mm^6\ m^{-3}$) and rain rate R (mmh^{-1}).

$$Z=aR^b \qquad \text{A.17}$$

If Rayleigh scattering is assumed then the reflectivity Z is given by Eq. A.18.

$$Z=\int N(D)D^6Dd \qquad \text{A.18}$$

Reflectivity is proportional to the 6th moment of the drop diameter. The rain rate can be expressed by Eq. A.19.

$$R=\frac{1}{\rho_l}\int_0^\infty m(D)n(D)V(D)dD \qquad \text{A.19}$$

where ρ_l is the density of water, n is the number of drops per volume, m is the mass of a drop given by Eq. A.20.

$$m = \rho_l \frac{\pi}{6} D^3 \qquad \text{A.20}$$

V(D) is the sedimentation velocity given by Eq. A.21.

$$V(D)=\alpha D^{\beta} \qquad \text{A.21}$$

Rain rate is therefore a function of the DSD, the 3rd moment of the drop diameter, and the drop fall velocity for a given diameter. Substituting for *V(D)* and *m* and solving the integral, the rain rate expression is simplified to

$$R = \frac{\alpha\pi}{6} N_0 D_0^{4+\beta} \Gamma(4+\beta) \qquad \text{A.22}$$

By relating the *Z* and *R* equations (Eqs. A.18, A.22) and applying the power law from Eq. A.17, the coefficients *a* and *b* can be solved for by assuming a DSD. Due to numerous potential combinations of DSDs and fall velocities, there is no uniform Z-R relationship. For different environmental conditions and precipitation types, many different rain rates can be derived for a given *Z*. The base equation for quantifying rain rate from reflectivity was derived by Marshall-Palmer, $Z=200R^{1.6}$. This is a generalized DSD, which is highly variable depending on region, hydrometeor composition, and storm intensity. Several *a* and *b* coefficients have been empirically derived to satisfy specific conditions and locales.

A.6.3 Attenuation and Beam Filling Effects

Attenuation is the gradual loss of signal due to interactions and interference with matter. There are varying degrees of attenuation ranging from partial to complete. For 10

cm radars like WSR88D, attenuation is negligible. For the 5 cm C-band, attenuation becomes an issue for long path lengths through heavy rain. Shorter wavelengths are better for high resolution imaging, but then the regime shifts from Rayleigh to Mie more quickly. For this reason, the TRMM PR (22 mm) may observe reflectivity of 40 dBZ (Rayleigh regime) whereas CloudSat (3 mm) observes only 20 dBZ (Mie regime) for the same overpass. Another issue is the beam filling effect. Beam filling errors, initially acknowledged by Wilheit (1986), result from the inhomogeneity of rain within the sensor field of view. When a pulse travels away from the antenna, the cone-shaped beam radially expands and often includes several rain intensities within its footprint. When unaccounted for, beam filling errors can underestimate rain up to a factor of 2 (Graves 1993). *A priori* information of the rain rate variability is required to understand how to deal with beam-filling issues (Kummerow et al. 2004), and varies according to footprint size.

A.7 TRMM Instruments and Products

The Tropical Rainfall Measuring Mission (TRMM) satellite was launched in November of 1997 and remains operational at the time of this writing. During August 2001 its altitude was boosted from 350 km to 402 km to reduce drag and therefore increase its lifetime in orbit. This platform provides coverage of latitudes from 36 S to 36 N, which play a major role in the global energy budget (Simpson et al. 1988).

A.7.1 Microwave Imager

The TRMM Microwave Imager (TMI) is a conically scanning 9 channel microwave radiometer with a 49 degree nadir angle that provides column integrated

precipitation data. The instrument operates at 10.65 GHz, 19.35 GHz, 21.3 GHz, 37.0 GHz and 85.5 GHz frequencies and has an 878 km swath width. Dual polarization at all frequencies except 21.3 GHz comprises the 9 channel suite.

To reduce the ambiguity between low brightness temperatures due to ice scattering and low brightness temperatures due to radiometrically cold sea surface, Spencer et al. (1989) derived the 85 GHz channel polarization corrected brightness temperature (Eq. A.23). Cecil et al. (2002) and Toracinta et al. (2002) use a similarly empirically derived formula for the 37 GHz channel (Eq. A.24).

$$PCT_{85} = 1.8T_{85v} - 0.8T_{85h} \qquad \text{A.23}$$

$$PCT_{37} = 2.2T_{37v} - 1.2T_{37h} \qquad \text{A.24}$$

where *v* and *h* subscripts are for vertical and horizontal polarizations. For TMI specifically, footprint sizes are 7 km x 5 km (85 GHz) and 16 km x 9 km (37 GHz) with scans every 14 km distance. The 85 GHz channel, therefore, is subject to under-sampling while the 37 GHz channel is subject to oversampling (Cecil et al. 2005).

The 2A12 surface rainfall product is computed over the 878 km TMI swath and uses the full spectrum of frequencies to make rain estimates (Kummerow et al. 1996, 2001). Cloud type, liquid water content, geographical location, and surface emissivity can adversely affect rain values. The 2A12 algorithm uses Bayesian inversion methodology to construct the most probable outcome given measured data and probability distribution likelihoods. The technique weights distributions to give high probability to likely outcomes, and low probability to unlikely outcomes. Rain estimates from the Goddard Cumulus Ensemble, a cloud microphysical model, are used to establish rainfall profile

distributions (Kummerow et al. 1996). Kummerow et al. (1996) showed that adding a 10.7 GHz frequency to the SSM/I channels (which then makes-up the TMI channel suite) eliminates several rain rate underestimations, since the 10 GHz channel does not saturate as quickly as the 19 GHz channel. Still, SSM/I estimates are less preferable due to its 833 km orbit altitude. TMI retrievals show excellent correlations with observations up to 25 mm h^{-1}.

A.7.2 Precipitation Radar

The TRMM Precipitation Radar (PR) is a 13.8 GHz (2.17 cm wavelength) electronically scanning radar that constructs 3-D rain profiles over land and ocean between 36 N and 36 S. The PR has a swath width of 247 km, a horizontal resolution of 5 km, and a vertical resolution of 250 m at nadir. The cross track scanning angle ranges from -17 to +17 degrees, which produces coarser than 1500 m resolution at limb. The implications for this range can be significant, such as the inability to resolve the bright band region. The minimum detectable signal is 17-18 dBZ, which corresponds to a rain rate of approximately 0.25 mm hr^{-1}.

The TRMM PR 2A25 rain retrieval algorithm estimates rain rate *R* from a measured reflectivity *Z* (Fig. A.3). The objective is to eliminate rain estimation errors by relating the observed radar reflectivity factor $Z_m(r)$ to the true radar reflectivity factor $Z_e(r)$ (Eq. A.25).

$$Z_m(r)=Z_e(r)A(r) \qquad \text{A.25}$$

A(r) is the attenuation factor which takes into account k(r), the attenuation coefficient. Two attenuation correction methods are implemented, the surface reference technique

(SR) and the Hitschfeld-Bordan method (HB). The SR estimate of path integrated attenuation (PIA_{SR}) ,$\Delta\sigma^o$, is derived from the apparent decrease of the surface scattering cross section in raining areas relative to that measured in rain free areas (Iguchi et al. 2000, Meneghini et al. 2000).

$$PIA_{SR} = \Delta\sigma^o = \sigma^o{}_{no\text{-}rain} - \sigma_{rain} \qquad A.26$$

The PIA_{HB} calculation requires an estimate of the attenuation factor A(r). A DSD model is selected based on the rain type (convective or stratiform) given by 2A23, then the k-Ze and Ze-R relationships are calculated for different temperatures (Iguchi et al. 2000). The HB method performs more superior for small attenuations and the SR technique becomes necessary with increasing path attenuation. The two independent estimations of PIA are subjected to a weighting function to yield a best guess, called PIA_e. This hybrid method was developed by Iguchi and Meneghini (1994). The non uniform beam filling (NUBF) effect must also be accounted for. Up to this point, the algorithm is still under the assumption of horizontally uniform rain over the 5 km footprint. The PIA will be modified again to create a new attenuation coefficient used to compute Z_e. The variable k denotes the specific attenuation and is related to Z_e by Eq. A.27.

$$k(r)=\alpha Z_e^{\beta} \qquad A.27$$

Alpha (α) is an adjusted coefficient determined by matching the PIA_{HB} with the PIA_{SR}. Initial differences in alpha are assumed to be the result of inappropriate assumption of initial DSD. A non uniformity index is created by normalizing the standard deviation of PIA variation within the radar resolution cell. A full derivation is displayed in Iguchi et

al. (2000). Rainfall estimates are calculated through the power law (Eq. A.17). The coefficients *a* and *b* are functions of the rain type, heights of the zero degree isotherm, and heights of the storm top.

Attenuation correction is extremely important because it can change the radar reflectivity factor by a factor of 10 or more (Iguchi et al. 2000). Though the assumed DSD and nonuniformity index can affect rain estimates, they are less significant than attenuation.

A.7.3 Lightning Imaging Sensor

The Lightning Imaging Sensor (LIS) is a staring optical imager collocated with the PR and TMI. Rapid changes in the 777.4 nm oxygen emission line are monitored for the detection of lightning both day and night. The LIS detects total lightning including intra-cloud, cloud to cloud, and cloud to ground strikes, and cannot differentiate among the three. Each observation period is for 80-90 s and thus allows for a minimum detectable flash rate of 0.7 fl min^{-1}. LIS has 2 ms temporal resolution and 3-6 km spatial resolution (Christian et al. 1992, 1999).

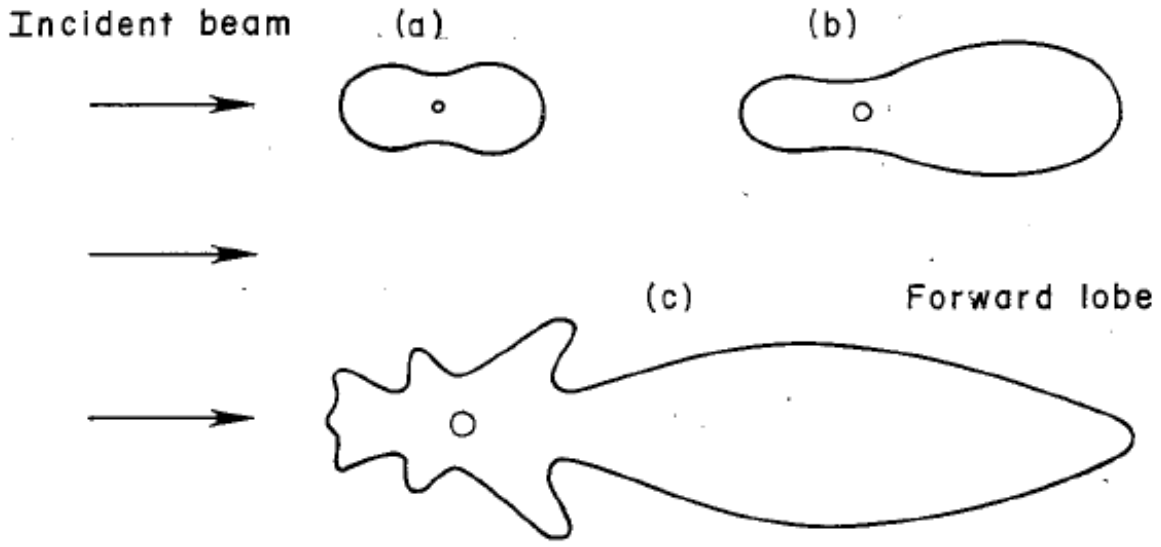

Figure A.1. Schematic showing the angular patterns of the scattered intensity from particles of three sizes: (a) small particles, (b) large particles, and (c) larger particles (Liou 1980). Reprinted with permission from Elsevier.

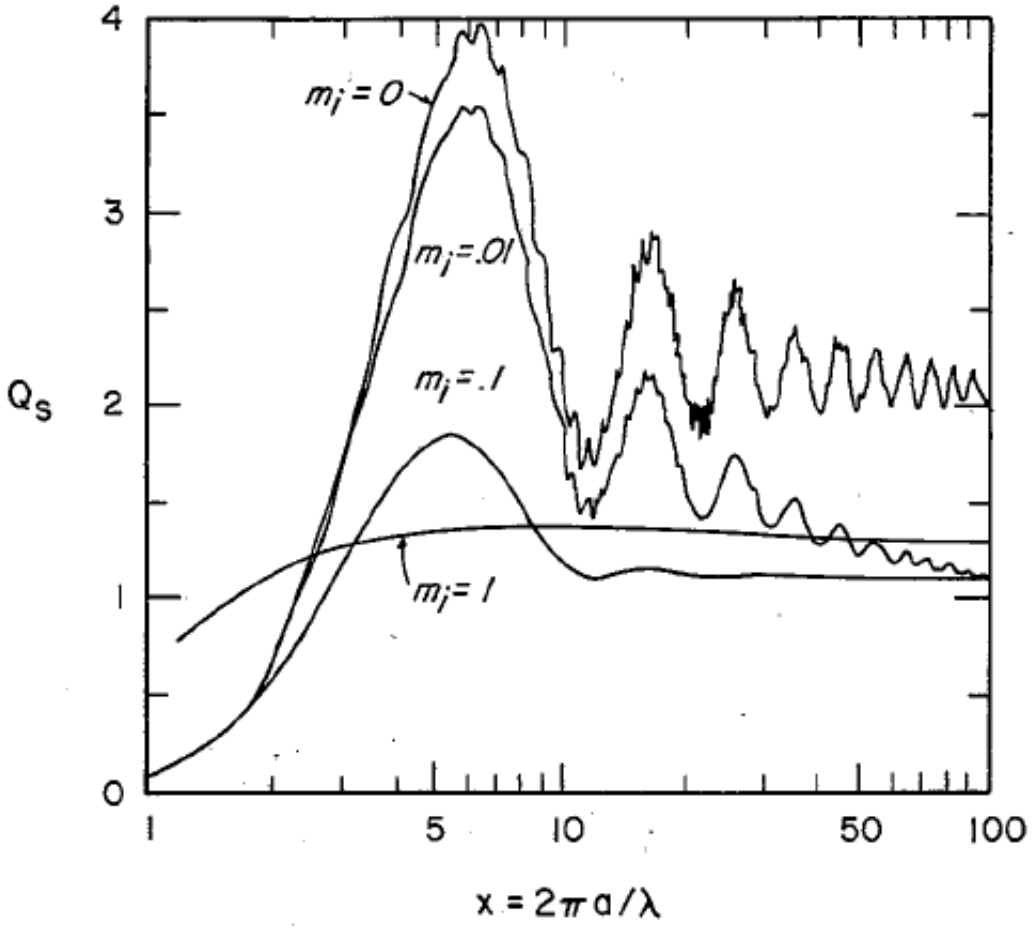

Figure A.2. The scattering efficiency as a function of size parameter x, plotted on logarithmic scale, for four different refractive indices (Liou 1980). Reprinted with permission from Elsevier.

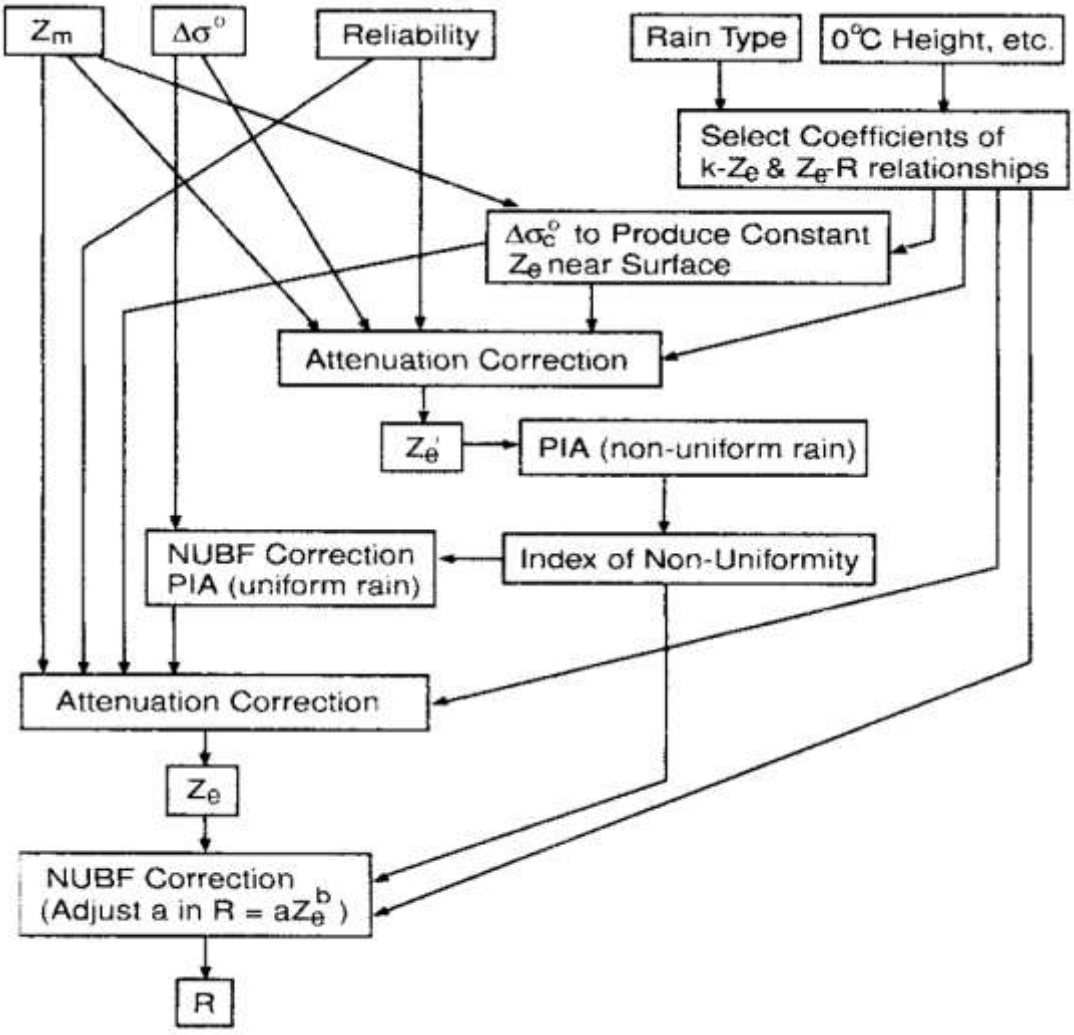

Figure A.3. Flowchart of the 2A25 algorithm (Iguchi et al. 2000).

REFERENCES

Abarca, S. F., K. L. Corbosiero, and D. Vollaro, 2010: The world wide lightning location network and convective activity in tropical cyclones. *Mon. Wea. Rev.*, doi: 10.1175/2010MWR3383.1.

Black, P. G., R. W. Burpee, N. M. Dorst, and W. L. Adams, 1986: Appearance of the sea surface in tropical cyclones. *Wea. Forecasting,* **5**, 102-107.

Black, R. A., and J. Hallet, 1986: Observations of the distribution of ice in hurricanes. *J. Atmos. Sci.,* **43**, 802-822.

Black, R. A., and J. Hallet, 1999: Electrification of the hurricane. *J. Atmos. Sci.,* **56**, 2004-2028.

Black, M. L., R.W. Burpee, and F. D. Marks Jr., 1996: Vertical motion characteristics of tropical cyclones determined with airborne Doppler radial velocities. *J. Atmos. Sci.,* **53**, 1887-1909.

Cecil, D. J., and E. J. Zipser, 1999: Relationships between tropical cyclone intensity and satellite-based indicators of inner core convection: 85 GHz ice-scattering signature and lightning. *Mon. Wea. Rev.*, **127**, 103-123.

Cecil, D. J., E. J. Zipser, and S. W. Nesbitt, 2002: Reflectivity, ice scattering, and lightning characteristics of hurricane eyewalls and rainbands. Part I: Quantitative description. *Mon. Wea. Rev.*, **130**, 769-784.

Cecil, D. J., and E. J. Zipser, 2002: Reflectivity, ice scattering, and lightning characteristics of hurricane eyewalls and rainbands. Part II: Intercomparison of observations. *Mon. Wea. Rev.*, **130**, 785-801.

Cecil, D. J., S. J. Goodman, D. J. Boccippio, and E. J. Zipser, 2005: Three years of TRMM precipitation features part I: Radar, radiometric, and lightning characteristics. *Mon. Wea. Rev.*, **133**, 543-566.

Cecil, D. J., and M. Wingo, 2009: Comparison of TRMM rain-rate retrievals in tropical cyclones. *J. Meteor. Soc. Japan*, **87**, 369-380.

Christian, H. J., R. J. Blakeslee, and S. J. Goodman, 1992: Lightning Imaging Sensor (LIS) for the Earth Observing System, NASA Technical Memorandum 4350, MSFC, Huntsville, AL.

Christian, H. J., and Coauthors, 1999: The Lightning Imaging Sensor. *Proc. 11th Int. Conf. on Atmospheric Electricity,* Huntsville, AL, National Aeronautics and Space Administration, 746–749.

Croxford, M., and G. M. Barnes, 2002: Inner core strength of atlantic tropical cyclones. *Mon. Wea. Rev.*, **130**, 127-139.

Emanuel, K. A., 1986: An air-sea interaction theory for tropical cyclones. Part I. *J. Atmos. Sci.,* **42**, 1062-1071.

Graves, C. E., 1993: A model for the beam-filling effect associated with the microwave retrieval of rain. *J. Atmos. Oceanic Technol.*, **10**, 5–14.

Hendricks, E. A., M. T. Montgomery, and C. A. Davis, 2004: The role of "vortical" hot towers in the formation of tropical cyclone Diana (1984). *J. Atmos. Sci.,* **61**, 1209-1232.

Hendricks, E. A., M. S. Peng, B. Fu, and T. Li, 2010: Quantifying environmental control on tropical cyclone intensity change. *Mon. Wea. Rev.*, **138**, 3243-3271.

Hence, D. A., and R. A Houze Jr., 2010: Vertical structure of hurricane eyewalls as seen by the TRMM precipitation radar. *J. Atmos. Sci*. *Under Review*.

Houze Jr., R. A., 2010: Clouds in tropical cyclones. *Mon. Wea. Rev.*, **138**, 293-344.

Iguchi, T., and R. Meneghini. 1994: Intercomparison of single frequency methods for retrieving a vertical rain profile from airborne or spaceborne data. *J. Atmos. Oceanic Technol.*, **11**, 1507–1561.

Iguchi, T., T. Kozu, R. Meneghini, J. Awaka, and K. Okamoto, 2000: Rain-profiling algorithm for the TRMM Precipitation Radar. *J. Appl. Meteor.*, **39**, 2038–2052.

Jiang, H., P. G. Black, E. J. Zipser, F. D. Marks Jr., and E. W. Uhlhorn, 2006: Validation of rain-rate estimation in hurricanes from the stepped frequency microwave radiometer: Algorithm correction and error analysis. *J. Atmos. Sci.*, **63**, 252-267.

Jiang, H., C. Liu, and E. J. Zipser, 2010: A TRMM-based tropical cyclone cloud and precipitation feature database. *J. Appl. Meteor. Climatol. In Press*.

Jiang, H., and E. J. Zipser, 2010: Contribution of tropical cyclones to the global precipitation from eight seasons of TRMM data: Regional, seasonal, and interannual variations. *J. Climate*, **23**, 649-663.

Jorgensen, D. P., E. J. Zipser, and M. A. LeMone, 1985: Vertical motions in intense hurricanes. *J. Atmos. Sci.,* **42**, 839-856.

Jorgensen, D. P., and M. A. LeMone, 1989: Vertical velocity characteristics of oceanic convection. *J. Atmos. Sci.,* **46**, 621-640.

Kaplan, J., and M. DeMaria, 2003: Large-scale characteristics of rapidly intensifying tropical cyclones in the north atlantic basin. *Wea. Forecasting,* **18**, 1093-1108.

Kelley, O. A., J. Stout, and J. B. Halverson, 2004: Tall precipitation cells in tropical cyclones eyewalls are associated with tropical cyclone intensification. *Geophys. Res. Lett*., **31**, L24112, doi: 10.1029/2004GL021616.

Kelley O. A., J. Stout, and J. B. Halverson, 2005: Hurricane intensification detected by continuously monitoring tall precipitation in the eyewall, *Geophys. Res. Lett*., **32**, L20819, doi: 10.1029/2005GL023583.

Kerns, B., and E. J. Zipser, 2009: Four years of tropical ERA-40 vorticity maxima tracks. Part II: Differences between developing and nondeveloping disturbances. *Mon. Wea. Rev.*, **137**, 2576-2591.

Khain, A., N. Cohen, B. Lynn, and A. Pokrovsky, 2008: Possible aerosol effects on lightning activity and structure of hurricanes. *J. Atmos. Sci.,* **65**, 3652-3677.

Kummerow, C., W. S. Olson, and L. Giglio, 1996: A simplified scheme for obtaining precipitation and vertical hydrometeor profiles from passive microwave sensors. *IEEE Transactions on Geosci. and Remote Sensing.* **34**, 1213-32

——, Coauthors, 2001: The evolution of the Goddard Profiling Algorithm (GPROF) for rainfall estimation from passive microwave sensors. *J. Appl. Meteor.*, **40**, 1801–1820

——, P. Poyner, W. Berg, and J. Thomas-Stahle, 2004: The effects of rainfall inhomogeneity on climate variability of rainfall estimated from passive microwave sensors. *J. Atmos. Oceanic Technol.*, **21**, 624–638.

Leary, L. A., and E. A. Ritchie, 2009: Lightning flash rates as an indicator of tropical cyclone genesis in the eastern north pacific. *Mon. Wea. Rev.*, **137**, 3456-3470.

LeMone, M. A., and E. J. Zipser, 1980: Cumulonimbus vertical velocity events in GATE. Part I: Diameters, intensity, and mass flux distributions. *J. Atmos. Sci.,* **37**, 2444-2457.

Liou, K.-N., 1980: *An Introduction to Atmospheric Radiation*. Academic Press, 392 pp.

Liu, C., E. J. Zipser, D. J. Cecil, S. W. Nesbitt, and S. Sherwood, 2008: A cloud and precipitation feature database from nine years of TRMM observations. *J. Appl. Meteor. Climate*, **47**, 2712-2728.

Lonfat, M., F. D. Marks, and S. S. Chen, 2004: Precipitation distribution in tropical cyclones using the tropical rainfall measuring mission (TRMM) microwave imager: A global perspective. *Mon. Wea. Rev.*, **132**, 1645-1660.

Lucas, C., E. J. Zipser, and M. A. LeMone, 1994: Vertical velocity in oceanic convection off tropical Australia. *J. Atmos. Sci.,* **51**, 3183–3193.

Lyons, W. A., and C. S. Keen, 1994: Observations of lightning in convective supercells within tropical storms and hurricanes. *Mon. Wea. Rev.*, **122**, 1897-1916.

Marshall, J. S., and W. M. Palmer, 1948: The distribution of raindrops with size. *J. Meteor*, **5**, 165–166.

Meneghini, R., T. Iguchi, T. Kozu, L. Liao, K. Okamoto, J. A. Jones, and J. Kwiatkowski, 2000: Use of the surface reference technique for path attenuation estimates from the TRMM Precipitation Radar. *J. Appl. Meteor.*, **39**, 2053–2070.

Mohr, K. I., and E. J. Zipser, 1996a: Defining mesoscale convective systems by their 85-GHz ice scattering signatures, *Bull. Amer. Meteor. Soc*., **77**, 1179-1189.

Mohr, K. I., and E. J. Zipser, 1996b: Mesoscale convective systems defined by their 85-GHz ice scattering signature: Size and intensity comparison over tropical oceans and continents. *Mon. Wea. Rev*., **124**, 2417-2437.

Mohr, K. I., R. Toracinta, E. J. Zipser, and R. E. Orville, 1996: A comparison of WSR-88D reflectivities, SSM/I brightness temperatures, and lightning for mesoscale convective systems in Texas. Part II: SSM/I brightness temperatures and lightning. *J. Appl. Meteor.*, **35**, 919–931.

Molinari, J., P. K. Moore, and V. P. Idone, 1999. Convective structure of hurricanes as revealed by lightning locations. *Mon. Wea. Rev.*, **127**, 520-534.

Montgomery, M. T., M. E. Nicholls, T. A. Cram, and A. B. Saunders, 2006: A vertical hot tower route to tropical cyclogenesis. *J. Atmos. Sci.,* **63**, 355-386.

Nesbitt, S. W., E. J. Zipser, and D. J. Cecil, 2000: A census of precipitation features in the tropics using TRMM: radar, ice scattering, and lightning observations. *J. Climate*., **13**, 4087-4106.

Price, C., A. Mustafa, and Y. Tair, 2009: Maximum hurricane intensity preceded by increase in lightning frequency. *Nature Geosci.*, **2**, 329 – 332.

Rao, G. V., and P. D. MacArthur, 1994: The SSM/I estimated rainfall amounts of tropical cyclones and their potential in predicting the cyclone intensity changes. *Mon. Wea. Rev.*, **122**, 1568-1574.

Riehl, H., and J. S. Malkus, 1958: On the heat balance in the equatorial trough zone. *Geophysica*, **6**, 503-537.

Rodgers, E. B., S. W. Chang, and H. F. Pierce, 1994: A satellite observational and numerical study of precipitation characteristics in western north atlantic tropical cyclones. *J. Appl. Meteor.*, **33**, 129-139.

Rodgers, E. B., and H. F. Pierce, 1995: A satellite observational study of precipitation characteristics in western north pacific tropical cyclones. *J. Appl. Meteor.*, **34**, 2587-2599.

Rodgers, E. B., R. F. Adler, and H. F. Pierce, 2000: Contribution of tropical cyclones to the north pacific climatological rainfall as observed from satellites. *J. Appl. Meteor.*, **39**, 1658-1678.

Rodgers, E. B., R. F. Adler, and H. F. Pierce, 2001: Contribution of tropical cyclones to the north atlantic climatological rainfall as observed from satellites. *J. Appl. Meteor.*, **40**, 1785-1800.

Samsury, C. E., and R. E. Orville, 1994: Cloud-to-ground lightning in tropical cyclones: A study of hurricanes Hugo (1989) and Jerry (1989). *Mon. Wea. Rev.*, **122**, 1887-1896.

Simpson, J., R. F. Adler, and G. R. North, 1988: A proposed Tropical Rainfall Measuring Mission (TRMM) satellite. *Bull. Amer. Meteor. Soc*, **69**, 278–295.

Simpson, J., J. B. Halverson, B. S. Ferrier, W. A. Peterson, R. H. Simpson, R. Blakeslee, and S. L. Durden, 1998: On the role of "hot towers" in tropical cyclone formation. *Meteorol. Atmos. Phys.*, **67**, 15-35.

Squires, K., and S. Businger 2008: The morphology of eyewall lightning outbreaks in two category 5 hurricanes. *Mon. Wea. Rev.*, **136**, 1706-1726.

Spencer, R. W., H. M. Goodman, and R. E. Hood, 1989: Precipitation retrieval over land and ocean with the SSM/I: Identification and characteristics of the scattering signal. *J. Atmos. Oceanic Technol*, **6**, 254–273.

Steranka J., E. B. Rodgers, and R. C. Gentry, 1986: The relationship between satellite measured convective bursts and tropical cyclone intensification. *Mon. Wea. Rev.*, **114**, 1539-1546.

Szoke, E. J., E. J. Zipser, and D. P. Jorgensen, 1986: A radar study of convective cells in mesoscale systems in GATE: Part I: Vertical profile statistics and comparison with hurricanes. *J. Atmos. Sci.*, **43**, 182-198.

Takahashi, T., 1978: Riming electrification as a charge generation mechanism in thunderstorms, *J. Atmos. Sci.*, **35**, 1536-1548.

Toracinta, E. R., D. J. Cecil, E. J. Zipser, and S. W. Nesbitt, 2002: Radar, passive microwave, and lightning characteristics of precipitating systems in the tropics. *Mon. Wea. Rev.*, **130**, 802-824.

Wilheit, T. T., 1986: Some comments on passive microwave measurement of rain. *Bull. Amer. Meteor. Soc.*, **67**, 1226–1232.

Xu, W., E. J. Zipser, C. Liu, and H. Jiang, 2010: On the relationships between lightning frequency and thundercloud parameters of regional precipitation systems, *J. Geophys. Res.*, **115**, D12203, doi: 10.1029/2009JD013385.

Yuter, S. E., and R. A. Houze Jr., 1995: Three-dimensional kinematic and microphysical evolution of Florida cumulonimbus. Part III: Vertical mass transport, mass divergence, and synthesis. *Mon. Wea. Rev.*, **123**, 1964–1983.

Zipser, Edward J., 1994: Deep cumulonimbus cloud systems in the tropics with and without lightning. *Mon. Wea. Rev.*, **122**, 1837-1851.

Zipser, E. J., and K. R. Lutz, 1994: The vertical profile of radar reflectivity of convective cells: A strong indicator of storm intensity and lightning probability? *Mon. Wea. Rev.*, **122**, 1751-1759.